UNIVERSITÀ DEGLI STUDI DI NAPOLI FEDERICO II

DEPARTMENT OF CHEMICAL, MATERIALS AND PRODUCTION ENGINEERING (DICMAPI)

PhD in "INDUSTRIAL PRODUCTS AND PROCESSES ENGINEERING"

XXXII cycle

"A NOVEL BIOENGINEERED CYSTIC FIBROSIS MODEL TO STUDY PATHOGENIC MECHANISMS AND EVALUATE THERAPEUTIC STRATEGIES"

Supervisor

Prof. Paolo Antonio Netti

Advisor

Dr.ssa Giorgia Imparato

Dr. Francesco Urciuolo

Dr.ssa Claudia Mazio

Coordinator

Prof. Giuseppe Mensitieri

PhD Student

Laura Sara Scognamiglio

Sommario

Abstract

Cystic fibrosis (CF) is one of the most common genetic diseases in the world; it is an autosomal recessive disease affecting various organs, in particular bronchi and alveoli in the lung. The pathology is caused by a mutation in the CFTR gene, which encodes a protein termed CFTR (Cystic Fibrosis Transmembrane Conductance Regulator) that functions as a channel for chlorine. The most common mutation present in 70% of worldwide CF cases is the ΔF508, a deletion (Δ meaning suppression) of three nucleotides, which results in a loss of phenylalanine in the 508 position of the protein.

CFTR is a chloride channel located at the apical membrane of epithelial cells of different organs where it plays an important role in transepithelial electrolyte and fluid transport [1]**.** This CFTR gene is mainly expressed in the respiratory epithelium, where the CFTR protein is found at the apical level of the epithelial cells. In the presence of the ΔF508 mutation, the CFTR protein cannot be glycosylated and folded or properly folded. Therefore, the protein gets stuck in the cell membrane and is not be able to reach the apical side of the respiratory epithelium. This causes a decompensation of chlorine, liquids and consequently the formation of a thick and viscous mucus that promotes bacterial colonization of the airways [2]. As a consequence of this infected and compromised environment, inflammation, fibrosis and remodeling of the extracellular matrix occur at the baso-lateral side of the epithelium; thus inducing the formation of a fibrotic connective tissue as a secondary response to the pathology [3] [4]. Furthermore, some studies have also revealed an alteration of the submucous glands present in the CF respiratory connective tissue [5].

Most of the studies about CF are focused on epithelial cells because they express CFTR and are directly compromised by the channel dysfunction. For this reason, the large majority of the in vitro models of CF are represented by epithelial cells. Currently, the most used models to study CF are animal models (murine) and epithelial cells models on filter. However, experiments with animals have always the drawback of ethical issues and, particularly in the case of murine models, of the scarce representativity of the human lung pathology, which is the most clinically relevant. As for the models of epithelia on porous membranes, although they are useful for many applications, they do not completely recapitulate the conditions of the tissue in vivo. Indeed, the absence of an extracellular matrix means that the epithelium / connective tissue crosstalk is missing, which

influences the differentiation and function of the epithelium in vitro and the response / adaptation to physiological stimuli or harmful events in vivo.

In this perspective, in the IIT@CRIB lab we established a novel tissue engineering approach to build-up organ in vitro. By following such strategy, we produced different organ models (i.e. skin [6,7], cervix [8]). Our results clearly demonstrated the fundamental role of the connective tissue in guiding in vitro epithelium morphogenesis. Using a similar method, as first aim of this PhD project, we developed a full thickness CF airway model, a 3D human bronchial tissue never made before, consisting of bronchial epithelium on an endogenous pulmonary extracellular matrix, thus produced exclusively by lung fibroblasts. This innovative model is extraordinarily useful for studying the effects of therapeutic strategies focused not only on epithelial response but also on stromal response in a dynamic environment representative of the native human condition.

Moreover, the second aim of this PhD project was to design and manufacture a microfluidic chip in which to insert the full tickness airway (normal and CF) or the epithelial model on porous membrane. This microfluidic device represents a new platform for tissue culture, which best summarizes the structure of the human lung and its environment under dynamic conditions. Furthermore, in addition to offering a new cell culture method, this chip allows a more realistic drug administration, by the systemic and air route, with the use of an engineered aerosol system directly on the chip. Finally, the microfluidic platform allows live monitoring of the tissue conditions by means of electrical measurements and the insertion of gold electrodes.

Chapter 1

State of art

The following thesis work regards the development of a novel bioengineered model of cystic fibrosis (CF), aiming to increase the complexity of the currently available in vitro models of the pathology, by including a pulmonary extracellular matrix and the establishement of a dynamic culture condition into a microfluidic chip. Such system is better representative of the in vivo environment, and useful for testing and evaluating tissue differentiation and function. For these reasons, the first chapter of this manuscript will describe the main features of tissue engineering and CF, with special focus on the pulmonary disease and in vitro airway models. At the same time, the principles of impedance spectroscopy to analyze electrical tissue properties will be underlyined. Futhermore, the importance of the Lung-on-chip model will be highlighted together with the explanation of the basis of microfluidics and microfabrication useful to build the microfluidic chip.

1.1 Tissue engineering

Tissue Engineering represents the first interdisciplinary field that integrates almost all fields of science, such as cellular/molecular biology, material science, chemistry, physics, industrial engineering and medicine. This discipline represents the new frontier in the biomedical arena, which has the purpose of repairing or even replacing tissues and organs (such as muscle, bone, cartilage, etc.) damaged by diseases, trauma or aging, thus restoring their integrity and functionality. Tissue eingineering, also defined *regenerative medicine*, is paving the way for new treatment options and a better quality of life for patients. In addition this science can have diagnostic applications by developing of in vitro tissue for testing drug metabolism and uptake pathogenicity [9].

The term "*Tissue Engineering*" appears around the seventies of the last century and it is intended only as a manipulation of tissue and organs. Later the term takes on the modern meaning, defined as that interdisciplinary field that applies the principles and methods of engineering and life sciences, in order to develop biological substitutes for the maintenance, repair, replacement or

functional enhancement of tissue organic or whole organs [10]. In 1994 the tissue engineering company was founded in Boston, whose acronym was TES (Tissue Engineering Society), also the specialized magazine "Tissue engineering" was founded (i.e. tissue engineering) [11]. TES was later transformed into TESI (Tissue Engineering Society International) and finally, a decade later (2005) from the union of the latter with other tissue engineering companies, such as the European one (ETES: European Tissue Engineering Society) and various Asian counterparts, the TERMIS (Tissue Engineering and Regenerative Medicine International Society) was born, including in addition to tissue engineering also the sector of regenerative medicine [12].

Tissue engineering creates biological tissues that aim to improve the function of diseased or damaged tissues. To enhance the function of engineered tissues, there is a need to generate structures that mimic the intricate architecture and complexity of native organs and tissues[13].

Tissue engineering is a relatively new field that uses living cells, biocompatible materials, and suitable biochemical (e.g., growth factors) and physical (e.g., cyclic mechanical loading) factors, as well as combinations thereof, to create tissue-like structures. Most frequently, the ultimate goal is implantation of these tissue constructs into the body to repair an injury or replace the function of a failing organ. The critical functions may be structural (e.g., bone, cartilage), barrier- and transport-related (e.g., skin, blood vessels), or biochemical and secretory (e.g., liver and pancreas). Tissue engineering also applies to the development of specialized extracorporeal life support systems containing cells (e.g., bioartificial liver and kidney), as well as tissue units that may be used for diagnostic screening. In addition to clinical applications, other uses include drug testing for efficacy and toxicology as well as basic studies on tissue development and morphogenesis[14].

Protagonists of this new scientific revolution are *stem cells* that constitute the "weapons" of regenerative medicine. Stem cells are the progenitor cells of all organs and tissues of living organisms. They are undifferentiated cells that have not yet taken on a specific type and function, but which, under certain conditions, can specialize and develop in tissues and organs [15].

In natural tissues, cells are immersed in an *ExtraCellular Matrix* (ECM), characterized by a structure of natural nanofibers, organized hierarchically to form a polymeric network which, through the interactions that are generated between the nanofibers and the cells, allows to[16,17]:

1. influence cell behavior (proliferation, differentiation and migration) thanks to biomechanical stimuli and interactions by binding to growth factors and interacting with surface cell receptors
2. support of the entire cellular architecture, thus determining the morphology of the tissue
3. influence the biochemical and biomechanical properties (compressive and tensile strength, elasticity…) of the different tissues and organs.

The natural extracellular matrix is made up of three classes of biomolecules:

- *structural fibrous proteins* such as fibrillar collagen (in particular of type I, II and III) and elastin: the collagen imparts structural integrity and resistance to tissues [10], while the elastin increases its elastic properties;
- *proteoglycans* or protein molecules formed by the union of glycosaminoglycans with ECM proteins: they allow to bind and store growth factors within the ECM;
- *non-proteoglycan polysaccharides*: an example is hyaluronic acid, which confers compressive strength to tissues thanks to its ability to swell in the presence of water [18].

Since the constituents of the extracellular matrix have a nanoscopic size (the diameter of structural proteins is between 50 and 500 nm [19]), for tissue engineering nanomaterials and nanotechnologies are used [20]. Currently, in fact, in this application area, biomaterials and polymeric nanocomposites are used in the synthesis of *scaffolds* that imitate the extracellular matrix as they have a high degree of affinity with the constituents of the cellular microenvironment, that is, they are capable of imitating the composition, the topography and the architecture of human tissues[21](Figure 1.1).

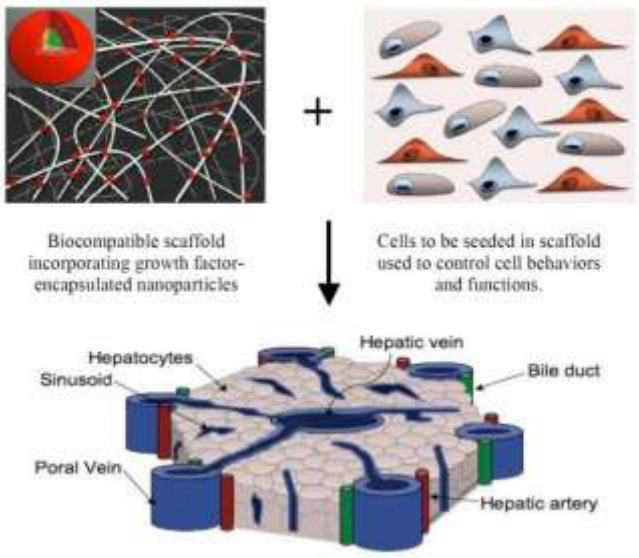

Fig. 1.1: An example of nanotechnology applications in complex engineered tissues [16].

Cells seeded into biocompatible and nanostructured scaffolds are able to reassemble into functional structures that resemble native tissues, under the stimulation of growth factors spatiotemporally delivered by nanoparticles. Complex tissues, like this lobule of the liver (Figure 1), could be engineered with the help of devices that are equipped with nanotechnology [16].

The challenge of tissue engineering is therefore twofold: on one hand, to identify a suitable support that contains the cells and in which the cells are needed and able to orient themselves to develop layered structures, on the other hand, to study and reproduce the conditions that allow cells to grow, multiply and differentiate into different types of tissues. The bioartificial material of the scaffold therefore affirms a temporal structure that acts as a homing to the cells, promotes their regeneration, the right direction and orientation. So three principal components are involved in tissue engineering combined together to regenerate a functional tissue (Figure 1.2)[22]:

- *Cells* to facilitate the required tissue formation;
- *Scaffold* that provides structure and substrate for tissue growth and development;
- *Growth factors* or biophysical stimuli to direct the growth and differentiation of cells within the scaffold.

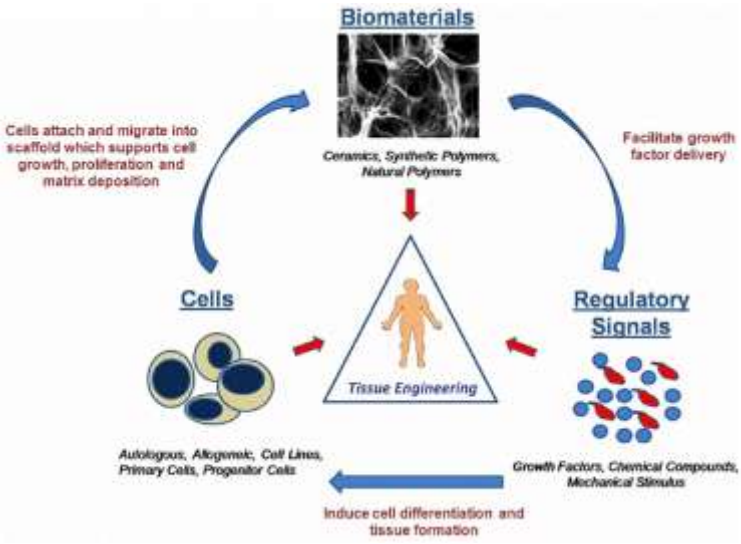

Figure 1.1 - The three essential components constituting the tissue-engineering triad.

However, in a wide range of pathologies, neither native nor purely artificial implantable materials can adequately replace or repair damaged tissues. The capability of a tissue to self-repair is limited to bone[23]or skin[24,25], provided that the damage is not invasive such as a small injury or a superficial wound. In many tissues such as myocardium [26]and cartilage[27]or in the case of large bone defect and deep skin wound, the self-repairing capability is lost and surgery becomes necessary. To overcome such limitations, tissue engineering focuses on the in vitro fabrication of living and functional tissues that can be implanted in the damaged zone to restore the healthy status. So, with the goal to create more complex tissues, including organized and functional microenvironments (cells-cells, cells-matrix communications and tissue specific morphology), the new tissue engineering techniques are beginning to focus on building modular microtissues with repeated functional units [13,28]. In other words, tissue engineering techniques are starting to generate micron-sized tissue modules with specific micro-architectural features, which can be used alone as a living filler in damaged areas. or serve as building blocks to design large biological tissues. This science represents an evolution of the field of biomaterial development, and refers to the practice of combining biodegradable scaffold, cells and molecules into functional tissues [29].

1.1.1 Classical approach

Classical strategies of tissue engineering employ a "*top-down*" approach in which cells are seeded on a biodegradable polymeric scaffold. In this top-down technique, cells populate the scaffold and

create the adequate extracellular matrix (ECM) and microenvironment often with the aid of growth factors, perfusion and mechanical stimulation[30]. One of the first rules to induce the formation of adequate microenvironement are the use of:

- biomimetic and biodegradable scaffolding
- structural features on the microscale to build modular tissues that can be used as building blocks to create larger tissues.

However, despite progress, top-down approaches often do not easily recreate the intricate microstructural features of 3D-tissues. Indeed this approach, which should produce viable tissue by seeding cells into preformed, porous, and biodegradable scaffolds, presents several problems mainly due to the difficulty in reproducing adequate micro environmental conditions in a three-dimensional (3D) thick structure [31,32].

1.1.2 Bottom up approach

An innovative modular approach intends to resolve typical problems of top-down approaches and to recreate the intricate microstructural features of tissues. This approach allows tissue building by assembling blocks, thus mimicking the units in a *bottom-up* design. The fabrication of those tissue models necessitates tools to create an initial architecture and to systematically manipulate their microenvironments in space and time. Once obtained microtissues, these multicellular units spontaneously aggregate and self-organize and can be used as building blocks to create larger scaffold-free tissues. One of the major challenges of this method is to assemble modular tissues with specific micro architectures into macroscale biomimetic engineered tissues. Despite this approach allows to print complex tissues with high shape resolution, these have limited use due to lack of mechanical integrity of the cellular aggregates that restricts the size of the resulting tissues. In addition to cell aggregates, the microtissues used as building units include cell-laden microgels, cell-seeded microbeads, and cell sheet. However, there is a strong biological basis for this bottom-up approach, as many tissues are made of repeating functional units, such as the lobule in the liver. By mimicking native microstructural functional units, bottom-up approaches aim to create more biomimetic engineered tissues. One of the major challenges by using this approach is to assemble modular tissues with specific microarchitectures into macroscale biomimetic engineered tissues[33,6]. Another challenge is to retain the microarchitecture and cellular behaviour of modular tissues and, at same time, to create engineered tissues with robust mechanical properties.

In this innovative method, microscale building blocks can be assembled into larger construct obtained by various technologies as: soft lithography, photolithography, membrane technology, centrifugal casting, micromachining, or the combination of multiple processes. Moreover, combination with computer-aided printing systems helps the generation of appropriate and complex 3D-templates. Designs must focus on promoting self-remodelling into the final architecture. Usually, these building blocks are composed of gel encapsulated cells or spontaneously aggregated cells [10]. Microbioreactors are other important makers of this approach. Indeed, the presence of microbioreactors allows long-term control of microscale tissues, formation of adequate microenvironement and accurate control of amounts of biological factors and relate gradients. The primary advantages of this method are the rapid production of millimetre-thick 3D cell structures, a homogeneous cell density, a tissue formation without necrosis in a period of less than a week and the possibility to culture microtissues in controlled and heterogeneous environments [34,35].

The strategy for the construction of biohybrids or 3D connective tissue refers to that described in a paper published by Palmiero et al in 2010 and it is based on the principle that most tissues in vivo are composed of repeating units of dimensions in the order of μ, consisting of different cell types and with a μ-architecture and tissue-specific functions. The bottom up approach allowed to obtain thick and viable 3D tissues starting from the assembly of μ-Tissue-Precursors (μTPs), obtained via dynamic seeding and culture of fibroblasts on porous gelatin micro-spheres. Fibroblasts from human skin biopsies were dynamically seeded and cultured on gelatin porous μscaffolds into Spinner Flask. Cells were able to adhere on the surface and into the pores of the scaffold and there to proliferate and produce elements of the extracellular matrix (ECM), in particular collagen I. Thanks to cell-cell and cell-matrix interactions, adjacent μTPs were able to increase in size and to coalesce, forming larger tissue precursors. To get the 3D tissue-equivalent, μTPs were assembled into specific maturation chambers and kept in dynamic culture regime. In a following work, Imparato et al. demonstrated that the mechanical properties and the degradation rate of the scaffold has an impact on the organization and maturation of the de novo synthesized collagen. In particular, they showed that modulating the density of the crosslinking it is possible to drive collagen deposition and assembly as well as to balance the degradation rate of the scaffold with tissue maturation and cell traction. The use of micro-scaffolds crosslinked with 4% of glyceraldehyde allowed to obtain a massive deposition of immature collagen, progressively assembled in mature collagen fibrils. The relationship between the degradation time of the

scaffold and the synthesis of collagen was just below the unit by determining an intermediate tissue ability to resist contraction[36]. Seeding human keratinocytes on this kind of matrix, led to obtaining a functional skin equivalent model in which it is possible to generate follicle-like structures in vitro resembling what occurs in vivo in the fetal skin. These results support the importance of the repository and regulatory role of the endogenous extra cellular matrix in guiding tissue morphogenesis[37].

Finally, figure 1.3 summarizes the main differences between the bottom up and the top down approaches: the traditional top-down approach (right) involves seeding cells into full sized porous scaffolds to form tissue constructs. This approach has many limitations, such as slow vascularization, poor diffusion, low cell density and non-uniform cell distribution. In contrast, the modular or bottom-up approach (left) involves the assembling of small, non-diffusion limited, cell-laden modules to form larger structures and has the potential to eliminate the shortcomings of the traditional approach [38].

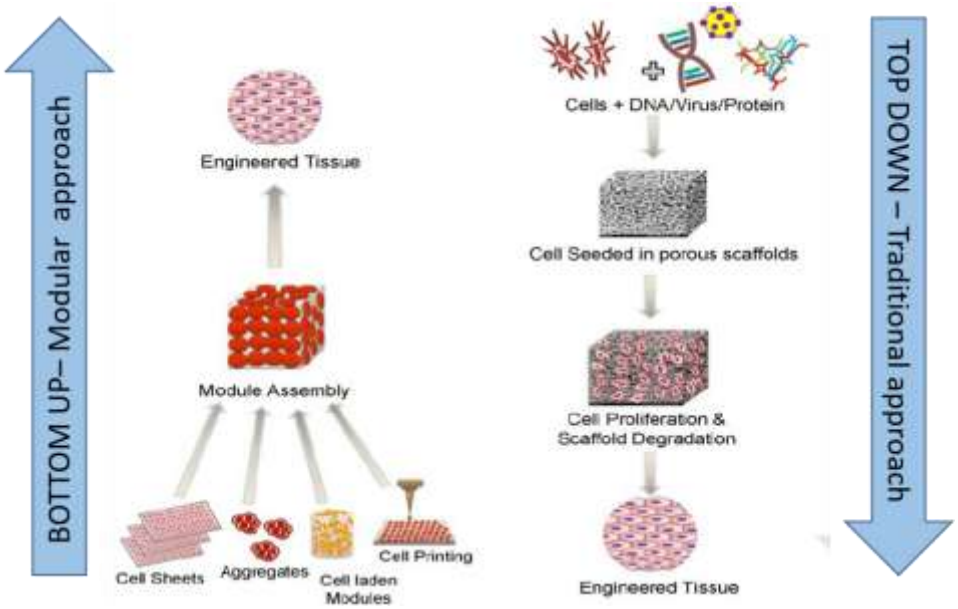

Figure 1.3- Bottom-up vs top-down approach in tissue engineering.

1.2 Cystic Fibrosis

Cystic fibrosis (CF) is a widespread disease of the transport epithelium that affects the secretion of fluids from the exocrine glands and the lining epithelium of the respiratory, gastrointestinal and

reproductive tract. This pathology leads to increased viscosity of the mucous secretions that obstruct the hollow organs, causing recurrent lung infections, pancreatic insufficiency, malnutrition, cirrhosis of the liver, intestinal obstruction and male infertility. Indeed, CF is a multi-organ disease, but lung dysfunction represents the main cause of mortality and morbidity for individuals with CF. The clinical manifestations of this disease can appear at any time in life, from birth to youth to adolescence [39].It can be said that in general one child is born in Europe with CF for every 2.0003.000 new born. In North America, one in 2,500-3,500 among whites, one in 4,000-10,000 among Hispanics (mestizos) and one in 15,000-20,000 among blacks. The disease is therefore much more frequent in white skin diseases, while in Asians it is very rare. CF is an autosomal recessive disease and therefore the heterozygous carriers are asymptomatic [40]. There is scientific evidence that suggests that CF defect affects not only the function of respiratory cells, but also that of cells, such as platelets and leukocytes which participate in the inflammatory response. Moreover, endothelial cells participate in the inflammatory response, regulating the traffic of leukocytes in inflamed tissues. If this filter function does not work properly, an uncontrolled passage of leukocytes into the tissues occurs, as in CF, with damage to the affected organ. Vascular endothelial cells express CFTR, the mutated gene in CF, and on the basis of preliminary experiments, we believe that a malfunction of CFTR can lead endothelial cells to lose the regulatory capacity of leukocyte flows in the tissues.[41,42]

- *The cystic fibrosis gene: structure, function and dysfunction.*

In normal epithelial ducts, chloride is transported by the channels of the plasma membrane (chloride channels). The primary defect in CF is represented by an abnormal function of the chloride epithelial channel protein encoded by the trans membrane cystic fibrosis conductance regulator (CFTR) whose gene is located on the long arm of chromosome 7. The encoded protein has two trans membrane domains, two cytoplasmic nucleotide-binding domains (NBD) and a regulatory domain (Domain R), which contains the phosphorylation sites of the kinase proteins A and C (Fig. 1.4).

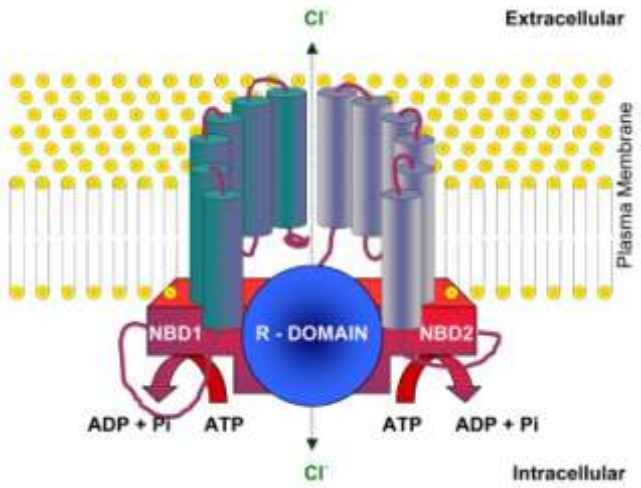

Fig. 1.4 - Structure and activation of the normal regulator of the trans membrane conductance of cystic fibrosis.

Antagonists (e.g. acetylcolin) bind to epithelial cells and increase cAMP that activates protein kinase A; the latter phosphorylates CFTR at the the R domain, causing the opening of the chloride channel. The binding of adenosine triphosphate (ATP) and hydrolysis take place in the domain binding the nucleotide and this is essential for the opening and closing of the channel in response to the signal mediated by cyclic AMP.
The most common mutation of the CFTR gene induces an endoplasmic / Golgi protein folding deficiency and CFTR degradation before it reaches the cell surface. Other mutations act on the synthesis of CFTR, on the domains that bind nucleotides, on the R domain and on the membrane domains. Although it was initially defined as a conductance channel for chloride, it has been shown that CFTR can regulate multiple ion channels and cellular processes through interaction with its nucleotide binding domain. These include the so-called exocellular channels for chloride, intracellular channels for potassium, epithelial channels for sodium (ENaC) and processes involved in the transport of ATP and in mucous secretion. Of these, the interaction of CFTR with the ENaC probably has the greatest pathophysiological relevance in CF. ENaC is located on the apical surface of exocrine epithelial cells and is responsible for the intracytoplasmic transport of sodium from luminal secretions, making the luminal fluid hypotonic. ENaC is inhibited by a normo functioning CFTR; therefore, in CF, there is an increase in the activity of ENaC with a consequent marked increase in the transport of sodium through the apical membranes. The only exception to this rule occurs at the level of the human sweat gland ducts, where ENaC activity decreases as a result of a

CFTR mutation; therefore, the lumen of the sweat glands contains a hypertonic secretion with a high content of chloride and sodium ("salty sweat").

CFTR functions are tissue-specific and, therefore, the impact of CFTR mutations is also tissue-specific. The most important function performed by CFTR in the sweat gland ducts consists in the reabsorption of chloride ions from the glandular lumen and in an increase in the reabsorption of sodium through ENaC. Therefore, in the ducts of the sweat glands the loss of CFTR function leads to an increase in the reabsorption of sodium chloride and to the production of hypertonic sweat. Specifically,the defect of CFTR leads to an inability of the gland to recover chlorine and sodium through its excretory duct, which are produced at the origin in a concentration equal to that of plasma; this means that sweat is eliminated on the skin with a high salt concentration [39]. In the respiratory and intestinal epithelium, CFTR regulates the active secretion of chloride inside the lumen. In these locations, CFTR dysfunction leads to the loss or reduction of the chloride excreted in the lumen. The active absorption of intraluminar sodium is also increased (due to loss of inhibition of the ENaC activity) and both of these ionic modifications increase the passive reabsorption of water from the lumen, lowering the water content from the coating surface of the cells of the mucous membranes[39]. Basically, therefore, if the channel is absent or malfunctioning, as in patients with CF, not enough chlorine is secreted outside the cell, while the sodium is reabsorbed in excess: this lack of chlorine and sodium at the surface of the epithelial cells involves a secondary reduction of water, which makes the secretions "dry" [40]. At the lung level, this dehydration leads to a deficit of ciliary mucus activity and to the accumulation of hyperconcentrated and viscous secretions that obstruct the passage of air and predispose to recurrent lung infections.

➢ *The cystic fibrosis gene: mutational spectra and genotype-phenotype correlation.*

Since CFTR gene cloning in 1989, more than 800 variants have been identified caused by different CFTR mutations which can be grouped into six "classes" based on their effect on the CFTR protein.

- Class I: *Impaired protein synthesis*. These mutations are associated with the complete lack of CFTR protein at the apical surface of the epithelial cells.
- Class II: *Changes in protein folding, processing and transport*. These mutations consist in the defective processing of the protein chain from the endoplasmic reticulum to the Golgi

apparatus; the protein does not become completely folded and glycosylated and it is consequently degraded before reaching the cell surface (cell membrane). The most common gene alteration of patients with CF is the deletion of three nucleotides encoding phenylanine in position 508 (**ΔF508**). Worldwide, this mutation can be found in about 70% of cases of CF [39].

- Class III: *Improper adjustment*. The mutations of this class prevent the activation of CFTR by preventing the binding and hydrolysis of the ATP, a fundamental prerequisite for the ion channel activity. There is a normal portion of the CFTR protein on the apical surface that however is not functional.
- Class IV: *Reduced conductance*. These mutations occur in the CFTR trans-membrane domain. There is a normal amount of CFTR in the apical membrane, which however has a reduced function (milder phenotype of CF).
- Class V: *Quantitative reduction*. These mutations reduce protein production and are associated with a milder phenotype of CF.
- Class VI: *Altered regulation of ion channels*. Mutations of this class affect CFTR conductance and its regulatory role of other ion channels. For example the ΔF508 mutation is a class II and class VI mutation[39].

1.3 Bronchial tree and cylindrical epithelium

The respiratory system consists of the lungs and the airways that put them in communication with the external environment; its function is to supply oxygen (O_2) to the body's cells and expell the carbon dioxide (CO_2) produced by them. The performance of this function requires the realization of the following four distinct events, collectively known as breathing:

- movement of air in and out of the lungs (breathing or ventilation)
- exchange of O_2 contained in the inspired air with carbon dioxide contained in the blood (external respiration)
- transfer of O_2 and CO_2 to and from cells (gas transportation)
- exchange of O_2 and CO_2 near the cells (internal respiration)

The first two events, ventilation and external respiration, take place inside the respiratory system, while it is the circulatory system that provides the transport of gases and internal respiration takes

place at the level of the body's tissues. The respiratory system is divided into two main parts: the conductive part which conveys air from the external environment and the respiratory part which provides for the exchange of oxygen with carbon dioxide (external respiration).

The respiratory system supplies oxygen, eliminates carbon dioxide and includes:

• the upper respiratory tract (nose and pharynx);

• the lower respiratory tract (larynx, trachea, bronchi and lungs)[43]

The bronchial tree begins at the bifurcation of the trachea, with the left and right primary bronchi forming branches that progressively decrease in size. The bronchial tree consists of the airways external to the lungs (primary bronchi, extrapulmonary bronchi) and the airways internal to the lungs: intrapulmonary bronchi (secondary and tertiary bronchi), bronchioles, terminal bronchioles and respiratory bronchioles (Fig. 1.5). The bronchial tree divides 15-20 times before reaching the level of the terminal bronchioles. As the airways decrease in size, a decrease in the amount of cartilage, the number of glands and goblet cells and the height of the epithelial cells, and an increase in smooth muscle tissue and elastic tissue (compared to the wall thickness) [44] can be observed.

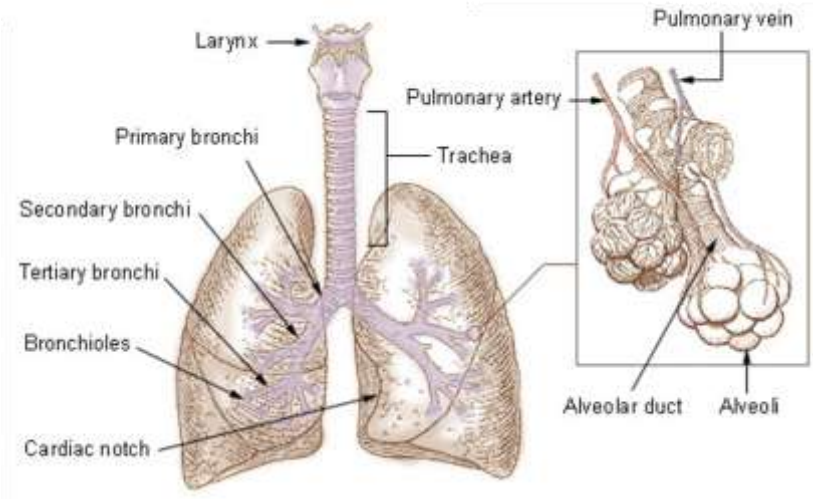

Fig. 1.5 – Bronchial tree

In particular, the primary and secondary bronchi on the outside are covered by a fibrous sheath and on the inside by the respiratory epithelium. The respiratory epithelium is a ciliated *pseudostratified cylindrical epithelium*, separated from the lamina by a thick basement membrane.

It is composed of six cell types: goblet cells, ciliated cylindrical cells, basal cells, brush cells, serous cells and cells of the diffuse neuroendocrine system (DNES). All these cells are in contact with the basement membrane, but not all of them reach the tracheal lumen [44](Fig. 1.6).

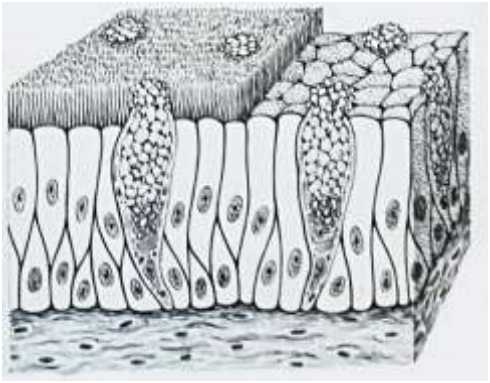

Fig. 1.6 – Pseudo stratified ciliated cylindrical bronchial epithelium [45]

Goblet cells make up about 30% of the respiratory epithelium cell population. They produce mucinogen that hydrates and becomes mucin once released in an aqueous environment. Like the goblet cells present in other parts of the body, those of the respiratory epithelium have a narrow stem below and an expanded theca above, which contains secretion granules. Electron microscopy shows how the nucleus and most of the organelles are located in the stem. This region also shows an extensive rough endoplasmic reticulum (RER), a well-developed Golgi complex, numerous mitochondria and abundant ribosomes. The display case is full of secretory granules, of varying diameter, containing mucinogen. The apical plasmalemma has few and short blunt microvilli. *Ciliary cylindrical cells* represent approximately 30% of the cells; they are tall and thin, with a basal nucleus, and have cilia and microvilli on the apical portion of the plasma membrane. The apical cytoplasm is rich in mitochondria and contains the Golgi complex. The rest of the cytoplasm has little RER and few ribosomes. These cells move the mucus and the corpuscular material incorporated in it, through the movement of the eyelashes, towards the nasopharynx for their elimination. *Basal cells* make up 30% of the cell population; they rest on the basement membrane and their apical surface does not reach the lumen of the organ. They are poorly differentiated and therefore considered stem cells, capable of proliferating to replace the ciliate cylindrical, brush and dead goblet cells. *Brush cells* (small mucous cells) represent 3% of the total cell population; they are narrow, cylindrical cells with high microvilli. Their function is unknown but, given that

they are related to nerve terminals, some authors have suggested that they paly a role in sensory activity; other researchers speculate that they are simply goblet cells that have already released their mucinogen. Serous cells are cylindrical cells that represent about 3% of the total cells of the respiratory epithelium. At the apex, they have microvilli and granules containing an electrosense serous secretion product. DNES cells, also known as small granule cells or Kulchitsky cells, represent 3–4% of the cell population. Many of these cells have long, thin extensions that extend to the lumen, and are believed to have the ability to monitor oxygen and carbon dioxide levels in the airway lumen. These cells are closely associated with naked nerve endings, with which they establish synaptic contacts, and together with these nerve fibers they make up the neuroepithelial pulmonary bodies. DNES cells contain numerous granules in their basal cytoplasm, where pharmacologically active substances can be found, such as amines, peptides, acetylcholine and adenosine triphosphate. Under hypoxic conditions, these substances are released not only in the synaptic cleft, but also in the spaces of the connective tissue of the lamina propria, where they act as paracrine hormones or pass into the circulation acting as real hormones[44].

1.3.1 In vitro models of airway epithelium

The two bronchial epithelium models currently on the market and used for clinical trials / drug screening are:

- *Mucilair* (Fig. 1.7)

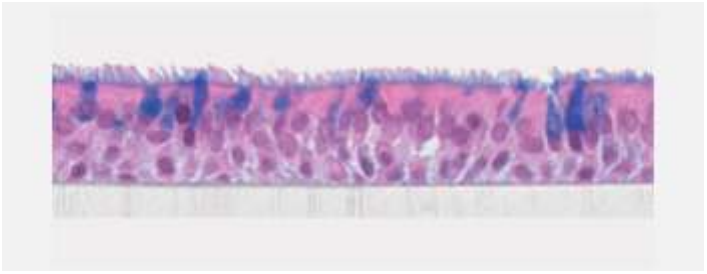

Fig. 1.7 – Bronchial epithelium on filter

This in vitro model, created by the Swiss company Epithelix in order also to allow the reduction of experiments on animals, involves the seeding of human primary cells on porous supports of a snapwell. This provides a "submerged phase" during which the epithelial cells, completely immersed in the culture medium, proliferate and replicate until they reach confluence. Then cells are placed in an "air liquid interface"(Fig. 1.8) by removing the culture medium from the apical are

of the filter on which the epithelial cells are placed. This allows cells to differentiate by reproducing the typical structure of cylindrical pseudostratified ciliated epithelium.

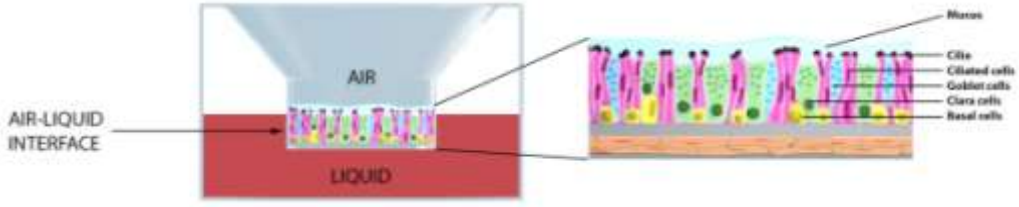

Fig. 1.8 - Cell culture condition for the Mucilair model

- EpiAirway - EpiAirway FT

MatTeck Corporation offers two types of respiratory models, EpirAirway (Fig. 1.9) and EpiAirway FT (Fig. 1.10): the first like Mucilair, simply reproduces the respiratory epithelium on porous inserts membranes (Transwell) and the second, more innovative, consists of epithelial cells that reproduce the typical pseudstratified cylindrical epithelium ciliated on pulmonary fibroblasts immersed in an exogenous collagen matrix.

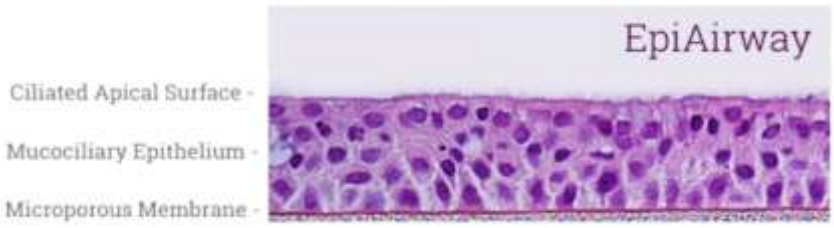

Fig. 1.9 - EpiAirway model

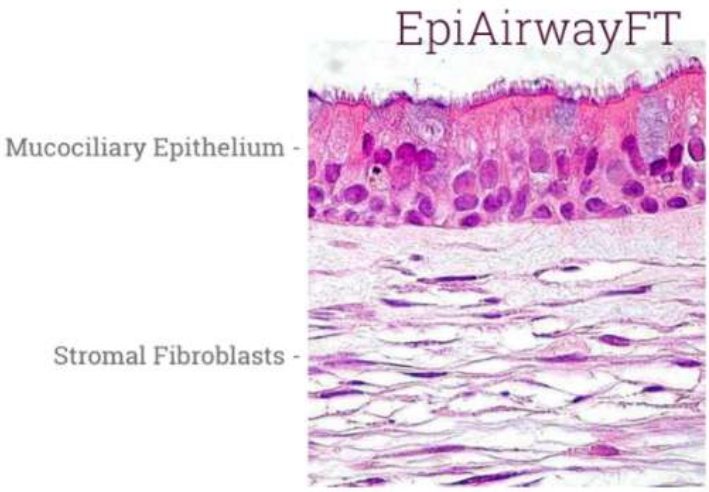

Fig. 1.10 - EpiAirway FT model

1.4 Airway Mucus Function and Dysfunction

1.4.1 Overview

The lungs are remarkably resistant to environmental injury, despite continuous exposure to pathogens, particles, and toxic chemicals in inhaled air. Their resistance depends on a highly efficient defense provided by the airway mucus, an extracellular gel in which water and mucins (heavily glycosylated proteins) are the most important components. Airway mucus traps inhaled toxins and transports them out of the lungs by means of ciliary beating and cough (Fig. 1.11). Paradoxically, although a deficient mucous barrier leaves the lungs vulnerable to injury, excessive mucus or impaired clearance contributes to the pathogenesis of several lung diseases including CF.

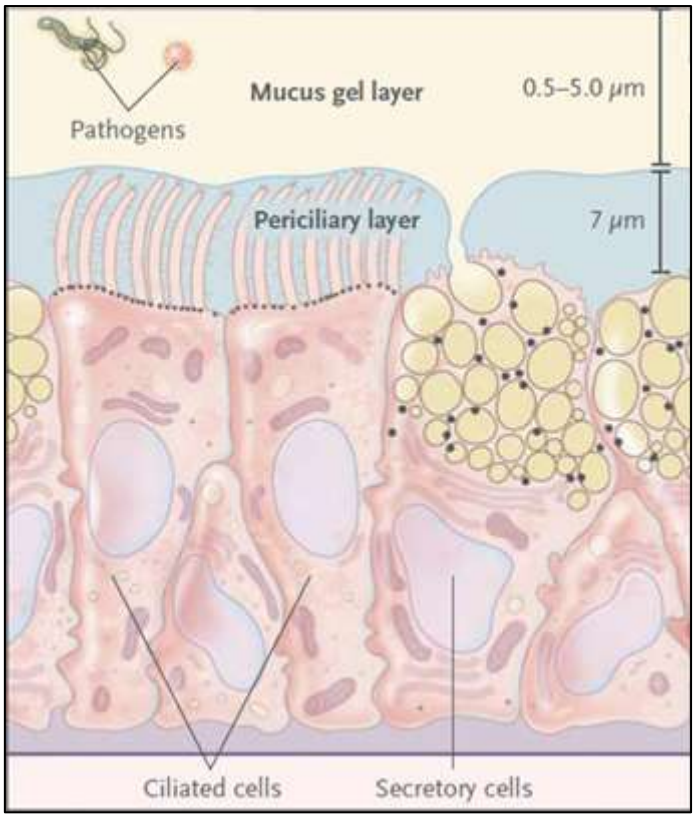

Fig 1.11 Bronchial epithelium

CF is indeed characterized by the buildup of thick, sticky mucus that can damage many of the body's organs. In people with CF, the body produces mucus that is abnormally thick and sticky. This abnormal mucus can clog the airways, leading to severe problems with breathing and bacterial lung infections, which cause chronic coughing, wheezing, and inflammation. Over time, mucus buildup and infections result in permanent lung damage, including the formation of scar tissue (fibrosis) and bronchiectasis [46].

Cystic fibrosis was previously termed “mucoviscidosis” [47,48] because copious amounts of viscid mucus were observed in the gastrointestinal and respiratory tracts of children when the disease was first reported in 1938 [49]. Mucus is a viscoelastic material that covers and protects the apical surfaces of the respiratory, gastrointestinal, and reproductive epithelial tracts and is a made of components secreted apically (luminally) by epithelial and glandular cells of the mucosal epithelium [50].

Mucin glycoproteins (mucins) are major macromolecular components of lung mucus [51,52]. Mucins (MUCs) are heavily *O*-glycosylated and are now identified by the *MUC* genes that encode their protein backbones.

1.4.2 Mucin Glycoproteins

Mucins are large glycoproteins with a carbohydrate content that accounts for 50%–90% of their molecular mass. They are characterized by a high number of *O*-glycans and an extensive number of tandem repeats (TRs) in their protein backbones that are high in threonine and/or serine and proline. Domains specific to individual mucins, TR domains, are a characteristic feature that distinguishes mucins from mucin-like glycoproteins, especially membrane-bound glycoproteins/receptors that have extracellular regions high in serine, threonine, and proline [53]. Mucins are classified by their MUC protein backbones, which are encoded by one of 18 *MUC* genes, as membrane-tethered (MUC1, MUC3A, MUC3B, MUC4, MUC11, MUC12, MUC13, MUC16, MUC17, MUC20), secreted, polymeric, and cysteine rich (MUC2, MUC5AC, MUC5B, MUC6, MUC19) or secreted and non-cysteine rich (MUC7, MUC8, MUC9) mucins [54].

Mucus and mucins provide a physiological barrier to environmental toxins and pathogens [55–57] and are part of the first line of innate immune responses in the airway epithelium [58]. Polymeric mucins are the major macromolecular components of lung mucus and form viscoelastic gels by interacting with other mucins and/or proteins[59,60]. MUC5AC and MUC5B are the predominant mucins in lung secretions. In healthy lungs, MUC5AC mRNA expression is restricted to goblet cells in the airway epithelium. MUC5B mRNA is expressed in mucosal cells of the submucosal glands, but is also expressed in goblet cells during the second trimester of gestation [61] and recently has been observed at the protein level in adult lungs. Although altered localization of cellular expression of secretory mucin genes has been reported—MUC5B mRNA in goblet cells in patients with various obstructive lung diseases [62] and MUC5AC protein in glandular cells of COPD patients[63] — this has not been observed in CF lungs. However, in neonatal wild-type and CF piglets, both MUC5AC and MUC5B mucins are expressed in goblet cells in the conducting airway epithelium, whereas MUC5B, but not MUC5AC, is expressed in glandular cells. Interestingly, the submucosal glands of CF piglets have reduced MUC5B immunostaining relative to gland volume, suggesting that mucous cell development is reduced and that airway changes that begin during fetal life may contribute to CF pathogenesis and its clinical manifestations during postnatal life[64] . MUC5AC and MUC5B are overproduced in CF lung secretions [65], especially following microbial exacerbations [66].

1.4.3 Mucociliary clearance in the normal and CF airway

The normal airway epithelium is covered by a biphasic mucus layer consisting of a viscous upper layer and a more fluid lower (periciliary) layer (Fig. 1.12). Concerted beating of epithelial cell cilia drives the mucus to flow unidirectionally toward the esophagus, carrying entrapped . In CF airways, alterations in either mucus secretion, mucus reabsorption, or both, make the mucus layer uniformly viscous, such that beating of the epithelial cilia is no longer sufficient to propel the mucus toward the esophagus. Bacteria can therefore persist in the diseased airways[67].

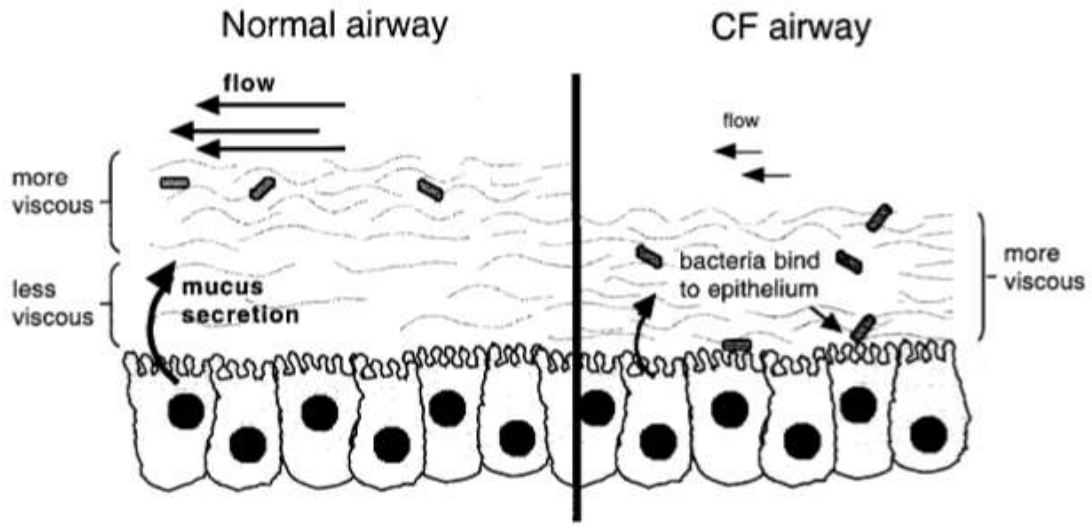

Fig. 1.12 - Comparison of mucociliary clearance in the normal airway and the CF airway

1.5 Mechanisms of tissue connective fibrosis

Pulmonary fibrosis is a respiratory disease characterized by hardening and scarring of the lung tissue that surrounds and interposes between the alveoli, thereby replacing the normal lung tissue. The term "fibrosis" indicates a particular process that can affect all tissues and organs modifying their structure and function. The most common example of fibrosis is that of the scar that forms as a result of a wound. Fibrosis is the mode of reaction and late repair to any inflammation, caused by microorganisms, chemicals or other agents. There are two forms of pulmonary fibrosis: the idiopathic form (IPF), for which a clear pathogenetic agent has not yet been found, and the secondary form, for which several determinants have been identified. For **IPF**,

a number of pathogenetic causes have been proposed such as cigarette smoke, coal and metal powders, select viral infections, genetic and hereditary factors. **Secondary pulmonary fibrosis** may by due to: infectious or autoimmune diseases, anticancer drugs and radiotherapy, cardiac problems and bacterial infections, prolonged exposure to toxic substances.

Fibrosis occurs through two main pathogenetic pathways. In the first, a primitive increase in connective tissue cells (fibroblasts, adipocytes and, more rarely, endothelial cells, smooth muscle cells, histiocytes and other connective cells) and extracellular matrix molecules (collagen, glycoproteins, proteoglycans and other molecules) occur. The causes and progression of this type of fibrosis are linked to an *unbalance between the production and degradation of connective tissue components*. In the second pathogenetic pathway, cells are damaged up to necrosis and are gradually replaced by connective tissue. The progression of this type of fibrosis, which is therefore secondary to the reparative response triggered by prolonged or chronic damage to the tissue parenchyma, is determined by the persistence of the damage and the continuation of the reparative response[68]. The main cells of the connective tissue are the *fibroblasts* that produce the connective matrix, a substance with amorphous and fibrillary constituents, which represents the carrier and nutritive axis of the other tissues. A significant proportion (about 1%) of these cells is a stem cell population with a high proliferative potential, capable of differentiating into mature fibrocytes (specialised in the production of connective tissue matrix) and in other connective cells, such as angioblasts (from which the new vessels are derived), smooth muscle cells, adipocytes, histiocytes, etc. Fibroblasts produce most of the components of the connective matrix, a smaller proportion is produced by the other connective cells and epithelial cells. The matrix molecules include collagen, glycoproteins, proteoglycans and elastin; each group consists of numerous proteins with a very similar structure, but with important functional roles that allow the construction and maintenance of complex tissues, organs and organisms. These proteins are usually long fibrous molecules that are organized in bundles (fibrils, fibres, shoots and capsules) with a considerable resistance to mechanical stresses [69].

In physiological conditions fibroblasts proliferate to guarantee the normal cellular replacement or during a reparative response (e.g., repair of a wound or area of parenchymal necrosis). Proliferative signals are triggered by various growth factors, especially transforming growth factor (TGF-β), fibroblast growth factor (FGFS), platelet-derived growth factor (PDGF) and epidermal growth factor (EGF) released by macrophages and other cells involved in inflammation and

healing. Moreover, fibroblasts express receptors for growth factors (TGF-β, FGFs, PDGF and EGF) which, depending on the combination, stimulate the proliferation and/or production of collagen and other matrix molecules. Among the various functions modulated by these complex signals, the inhibition of proliferation, the production of collagen and other matrix molecules, the control of matrix degradation by proteases (Collagenases, hyaluronidase, other metalloproteinases, plasmin and other Serin-o cysteinproteases) are particularly relevant. Most of the pathogenetic mechanisms of fibrosis include the alteration of at least one of these molecular pathways.

Fibrosis has significant tissue and organ consequences. The increase in connective constituents can affect the interstitium, or replace part of the damaged parenchyma. The mechanisms of fibrosis-related functional impairment include mainly three aspects: 1) Reduction of the elastic and stiffening component (sclerosis) of various tissue and organ structures, including walls (e.g. alveolar septa), vessels and other structures (e.g., exocin ducts, *bronchi*, intestines, excretory channelles, etc.); 2) Perivasal deposition with consequent stiffening and more or less severe reduction of the vessel lumen. In this case, the effects on the local circulation (increased hydrostatic upstream pressure) and the intake of oxygen and nutrients to hypoperfuse downstream cells, which will be able to go against hypoxic damage; 3) disorganization at various degree of organ architecture for the improper increase of the connective component, often not homogeneous and in any case excessive. Such disorganization is responsible for further and less repairable functional damage. In the case of parenchyma replacement, the clinical consequences are related to the degree of functional deficiency, i.e., their severity is proportional to the amount of parenchyma lost and the scenario is that of organ insufficiency. The situation is analogous in case of progressive disorganization of the tissue architecture and, above all, of the vascular stroma, often macroscopically evident with alterations of shape and consistency (sclerosis, scleroinsufficiency) [69].

1.6 Electrical properties of biological tissues

Unlike metallic conductors, electrical conduction within biological tissues is due to ions. In the presence of an electric field, a conduction current Ic will develop due to the movement of mobile ions within the aqueous biological medium. This current is therefore related to the ionic content and ionic mobility of the specific tissue and it is expressed as tissue's conductivity σ. The ion

mobility is also temperature dependent. Bound charges within tissues give rise to complex dielectric properties, and thus displacement currents Id will contribute to the time-varying electrical behavior. These bound charges include electrical double layers at membrane surfaces and polar molecules, such as proteins. Both conductivity and relative permittivity vary widely between different biological tissues and these parameters also vary with the frequency of the applied field. The permittivity is related to the extent to which the bound charges can be displaced or polarized under the influence of the electric field. Each polarizable entity within the tissue will exhibit its own characteristic response and thus a distribution of relative permittivities will give rise to a complex function of frequency of the form:

$$\varepsilon^*(\omega) = \varepsilon_{HF} + (\varepsilon_{LF} + \varepsilon_{HF}/(1 + j\omega\tau)$$

where ε_{HF} is the high-frequency permittivity at which the polarizable entities are unable to respond, ε_{LF} the low frequency permittivity where polarization is maximal, ω the angular frequency and τ the characteristic relaxation time of the tissue under study. A dielectric dispersion is therefore associated with biological tissues in which the relative permittivity decreases with increasing frequency. However, the displacement current is proportional to the applied field frequency and so these two opposing factors lead to a complicated frequency behavior. In general, three discrete regions of dispersion can be identified in biological tissues.

These are commonly defined as:

• Alpha dispersion, associated with tissue interfaces, such as membranes.

• Beta dispersion, associated with the polarization of cellular membranes and protein and other organic macromolecules.

• Gamma dispersion, associated with the polarization of water molecules.

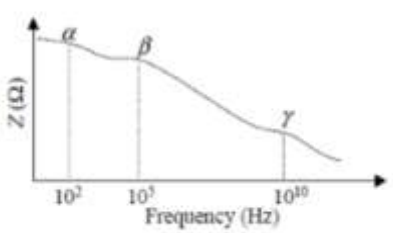

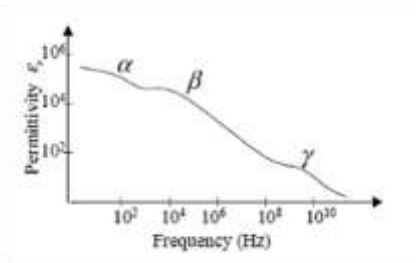

Fig. 1.13 - (on the left) Theoretical impedance diagram showing the α, β and γ dispersions for muscle tissue; (on the right) An idealised plot of the relative permittivity as a function of frequency for a typical biological tissue

The figure 1.13 shows an illustration of these frequency dispersions. It should be noted that such dispersions or some tissues may be not clearly distinguishable. Also, additional secondary dispersions may be present. Although factors contributing to alpha dispersion are still not fully understood, it is reasonable to expect that alpha dispersion's form is influenced by the membrane potential as well as by other physiological processes, which control the transport of ions from one side to the other of the membranes. The beta dispersion is mainly due to two processes, the first results from the capacitive properties of the membranes in storing the electric charge. In particular, this dispersion is attributed to a membrane Maxwell-Wagner polarization, which acts as barrier to ion flow between intra- and extra-cell compartments. A second effect derives from polarization of proteins and other macromolecules with ionized groups.

1.5.1 Capacitance and Resistance of plasma membrane

Every animal cell is enclosed in a *plasma membrane*, which has the structure of a lipid bilayer with many types of large molecules embedded in it. Because it is made of lipid molecules, the plasma membrane intrinsically has a high electrical resistivity, in other words a low intrinsic permeability to ions. However, some of the molecules embedded in the membrane are capable either of actively transporting ions from one side of the membrane to the other or of providing channels through which they can move. In electrical terminology, the plasma membrane functions as a combined *resistor* and *capacitor*. Resistance arises from the fact that the membrane impedes the movement of charges across it. Capacitance arises from the fact that the lipid bilayer is so thin that an accumulation of charged particles on one side gives rise to an electrical force that pulls oppositely charged particles toward the other side [70].

The double lipid layer of membranes, impervious to ions, acting as an isolate separating two layers of loads, gives the membrane an electrical capacity. Instead, the ionic channels, through which the electrical charges move, equip the membrane with its own electrical conductance. These two electrical properties of the membrane can be conveniently represented by an equivalent circuit in which a capacitor is connected in parallel with a resistor. The resistance represents the conductance of the ionic channels while the capacitor represents the capacity of the lipid double layer. Therefore, the resistance of a membrane is a measure of its ion impermeability while

conductance is a measure of its ion permeability. In the presence of a given transmembrane voltage, the lower the resistance of the membrane (i.e., the greater its conductance), the greater the number of ions that pass through the ionic channels of the membrane in the time unit. The relationship between the current, the resistance and the voltage through a membrane is given by the OHM's law, which states that the voltage variation caused by a current flowing through the membrane is directly proportional to the current multiplied by the resistance of the membrane:

$$\Delta V_m = \Delta I \times R$$

where ΔV_m is the voltage variation, ΔI is the current (in ampere) and R is the electrical resistance (in Ohm, Ω). In addition:

$$\Delta V_m = V_m - E_{nerst}$$

where E_{nerst} is the reversal potential (also known as the *Nernst potential*) of an ion is the membrane potential at which there is no net (overall) flow of that particular ion from one side of the membrane to the other [71].

The entry resistance of a cell (i.e. the total resistance encountered by the current flowing inward or outward of the cell) varies depending on the area of its membrane, as the membrane of a large cell will normally contain a number of channels higher than a smaller cell. For this purpose, it defines the *specific resistance,* Rm, of the membrane, as:

$$R_m = R \times A$$

where A is the membrane area and Rm is the resistance per unit of the membrane area. By rearranging the OHM's law, we can get $Rm = \Delta Vm/\Delta I$ and replacing:

$$R_m = (\Delta V_m/\Delta I) \times A$$

where the ratio $\Delta Vm/\Delta I$ is in Ohm and the area in square centimeters, so Rm will be expressed in Ohm x cm^2. The reciprocal of the Resistance R, is the *conductance*, G (whose unit of measure is the Siemens S):

$$G = 1/R$$

Substituting this expression in the Ohm's law, we will have:

$$\Delta V_m = \Delta I \, G_{IN}$$

The reciprocal of the specific resistance of a membrane is the specific *conductance,* G_m. The conductance strongly depends on the ionic permeability of the membrane. Moreover, for a given ionic species, conductance is defined according to the OHM's law as the current conveyed by that ionic species divided by the electrical force acting on the ionic species itself:

$$G_x = I_x / \varepsilon_x$$

where G_x is the membrane conductance for the specific ions x, I_x is the current conveyed by X and ε_x represents the electromotive force acting on X. Thus, even if the membrane is potentially permeable to the X-ion, the G_x conductance obviously depends on the presence and concentration of this ion in solution [71,72].

The cell membrane can be represented by the following equivalent circuit model RC (Fig. 1.14):

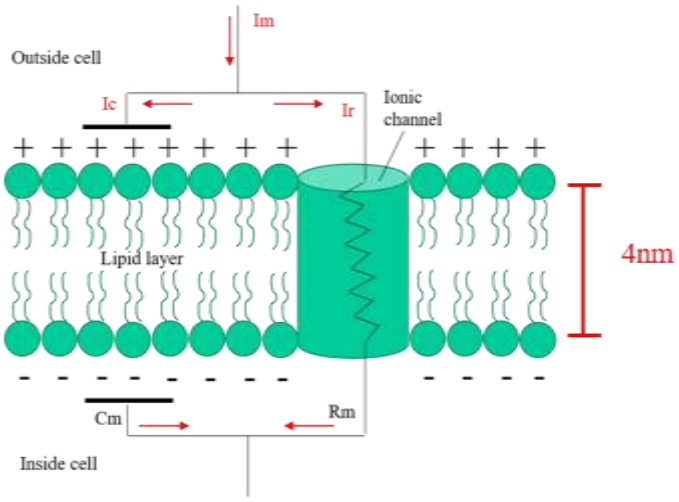

Fig. 1.14 - Equivalent circuit model RC of the plasme membrane

After the application of a stimulus, the current I_m crossing the membrane is divided into two components: Ic (Capacitive current: ion flow that makes the charge on the membrane capacity vary, Ir (Ionic current: ion flow through ionic channels, R).

When applying a stimulus:

1) The current flowing through the membrane goes to load the Capacitor (varies the charge, Vm).

2) When Vm changes, the ions begin to cross channels (R)and Ii increases.

3) When the condenser is charged, all applied current crosses R

$$\Delta V_m = R \times I$$

4) At the end of the impulse, the current generated by the capacitor discharge will pass through R.

1.5.2 Barrier function of tight junctions

In many tissues (e.g. connective tissue), each cell is separated from the next by extracellular components or matrix. However, in some tissues (e.g. Epitelia, Fig 1.15), the plasma cell membranes adhere to each other and are thus pressed one against the other. The structures that derive from this cellular arrangement are called *cellular junctions*.

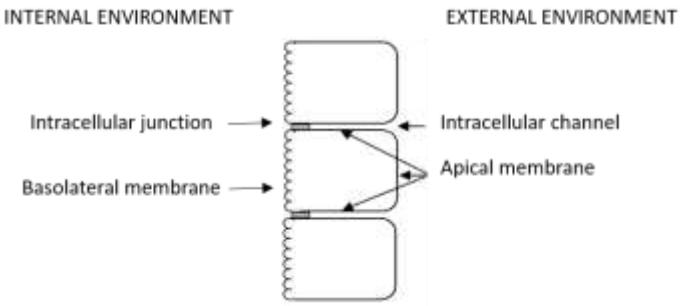

Fig 1.15: Schematic model of Epithelia

Epithelial cells have many functions:

- They constitute a barrier with the outside environment .
- They regualate the movement of countless incoming or outgoing substances through this barrier by absorption or secretion.
- They transform the external substances.

The epithelial apical and basolateral section of the cell mebrane are different both from the morphological and functional point of view. This diversity gives the epithelium the ability to operate a direct net transport of a given substance, from the lumen to the blood, i.e. absorption, or from the blood to the lumen, i.e. secretion.

Three main types of epithelial intercellular junctions are known:

- Tight junctions are connections among the proteins of the plasma membrane of neighboring cells, or structures that produce a barrier-like closure (intestinal system, kidney and lung where fluids must be contained in a specific area).
- Adherent junctions are structures that mechanically join adjacent cells. When a cell moves, the junction tends to pull it and bring it back to the cytoskeleton of the neighboring cell. They also connect the epithelium to the underlying basal membrane.
- Gap junctions represent pathways of communication between the cells. They constitute an open passage through which ions and small molecules can directly pass from one cell to the other.

Tight junction are the main responsible for the epithelial barrier function [73].

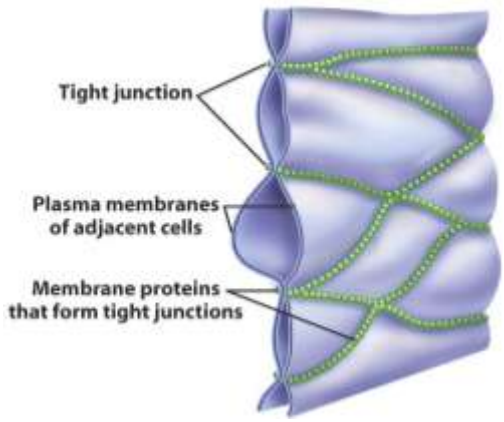

Fig 1.

Fig. 1.16 - Threedimensional view of tight junctions [73]

The two main membrane proteins of the tight junctions are Claudine and Occludin. These proteins protrude on the outer face of the membrane and are joined together by non-covalent bonds. Tight junctions are particularly present in the lining epithelia (e.g. skin), in the intestinal or *pulmonary epithelium*. They prevent the passage of fluids between the cells forming around the cellular perimeter a continuous belt (called Zonula).

The evaluation of a good epithelial cell differentiation and therefore the correct formation of tight junction is carried out by measuring the *Transepithelial Electrical Resistance (TEER)*.

1.7 TEER analysis and measurement Methods

As mentioned above, the analysis of the TEER allows to:

- Measure the electrical resistance to the passage of fluids through the epithelium
- Measure the epithelium integrity and in particular the status of the tight junctions formed between polarized cells
- Measure the confluence and degree of epithelial cell differentiation

1.7.1 The Ohm's Law Method

The electrical resistance of a cellular monolayer, measured in ohms, is a quantitative measure of the barrier integrity. The classical setup for measurement of TEER, shown in Figure 1.17, consists of a cellular monolayer cultured on a semipermeable filter insert, which defines a partition between apical (or upper) and basolateral (or lower) compartments. For electrical measurements, two electrodes are used, with one electrode placed in the upper compartment and the other in the lower compartment and the electrodes are separated by the cellular monolayer. In theory, the ohmic resistance can be determined by applying a direct current (DC) voltage to the electrodes and measuring the resulting current. The ohmic resistance is calculated according to the Ohm's law as the ratio of the voltage and current. However, DC currents can damage both cells and electrodes. To overcome this issue, an alternating current (AC) voltage signal with a square waveform is applied. In the widely used and commercially available TEER measurement system known as an Epithelial Voltohmmeter (EVOM)[74], an AC square wave at a frequency of 12.5 Hz is used to avoid any charging effects on the electrodes and the cell layer. The EVOM system (Fig 1.17) has a measurement range of 1-9,999 Ω with a 1Ω resolution and uses a pair of electrodes, popularly known as a STX2/ "chopstick" electrode pair. Each stick of the electrode pair (4 mm wide and 1 mm thick) contains a silver/silver chloride pellet for measuring voltage and a silver electrode for passing current. The measurement procedure includes measuring the blank resistance (R_{BLANK}) of the semipermeable membrane only (without cells), and measuring the resistance across the cell layer on the semipermeable membrane (R_{TOTAL}). The cell specific resistance (R_{TISSUE}) in units of Ω, can be obtained as:

$$R_{TISSUE}(\Omega) = R_{TOTAL} - R_{BLANK}$$

The TEER readings with EVOM2 are highly dependent on the electrode positions and a careful handling of the electrodes is required while introducing them into the well under test to avoid any

disturbance to the cells. The uniformity of the current density generated by the electrodes across the cell layer has a significant effect on TEER measurements. The STX2/ “chopstick” electrode cannot deliver a uniform current density over a relatively large membrane, such as the ones used in 24 mm diameter tissue culture inserts, and therefore leads to an overestimation of the TEER value. As an alternative to STX2/ “chopstick” electrodes, an EndOhm chamber [75], which allows the cups from culture wells to be inserted, can be used. In an EndOhm chamber, both the chamber and the cap contain a pair of concentric electrodes: a voltage-sensing silver/silver chloride pellet in the center plus an annular current electrode. The symmetrical arrangement of circular disc electrodes on both sides of the membrane in an EndOhm chamber generates a more uniform current density across the membrane when compared to STX2/ “chopstick” electrodes. Also, with EndOhm’s fixed electrode geometry, variation of measurements on a given sample is reduced to 1-2 ω when compared to 10-30 ω with STX2 electrodes.

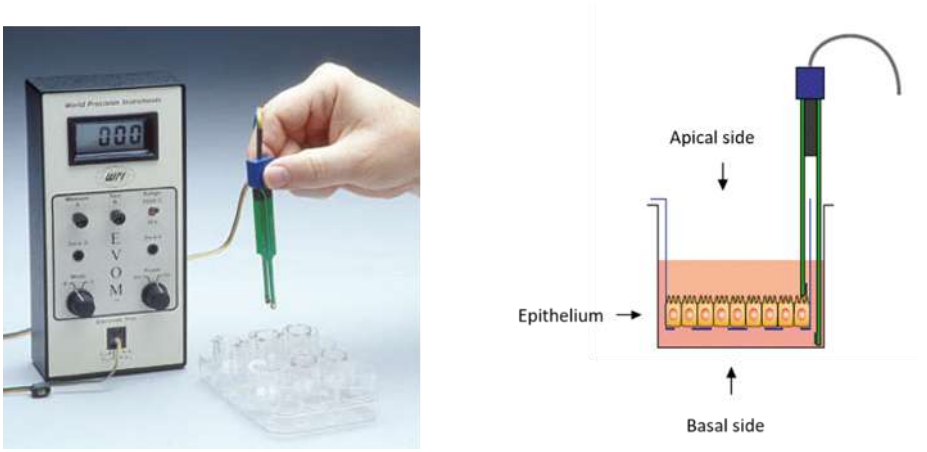

Fig 1.17 - TEER measurement with “chopstick” electrodes.

1.7.2 Impedance Spectroscopy

Impedance spectroscopy when combined with a fitting algorithm provides a more accurate representation of TEER values than traditional DC/single frequency AC measurement systems[76]. Impedance spectroscopy is performed by applying a small amplitude AC excitation signal with a frequency sweep and measuring the amplitude and phase response of the resulting current.

Electrical impedance (Z) is the ratio of the voltage-time function V (t) and the resulting current-time function I (t):

$$Z = \frac{V(t)}{I(t)} = \frac{V_0 sin\theta}{I_0 \sin(2\pi ft + \Phi)} = \frac{1}{Y}$$

$$Z = Z_R + jZ_I$$

where V_0 and I_0 are the peak voltage and current, f is the frequency, t is the time, Φ is the phase shift between the voltage-time and current-time functions, and Y is the complex conductance or admittance. Z is a complex function and can be described by the modulus |Z| and the phase shift Φ or by the real part Z_R and the imaginary part Z_I. Impedance measurement across a wide spectrum of frequencies, instead of a DC/single frequency AC TEER measurement, can provide additional information about the capacitance of the cell layer. Electrical impedance spectroscopy (EIS) has been widely used to assess the condition of animal tissues, both in vivo, in vitro and ex vivo and for various other applications. This method is useful to characterize cellular changes quantitatively. The electrical impedance of a volume of tissue at a series of frequencies provides information about the cell population. Predominantly, the characteristics and integrity of the population's plasma membranes, cell volumes and intra and extracellular conductivities influence the impedance spectrum. Thus, EIS can be used as a method of identifying and following in time detectable cellular responses, in ex vivo, in vivo and in vitro systems. In general, EIS provides impedance information in a wide range of frequencyies, which is not available via other non-invasive diagnostic techniques and which can be used for treatment purposes. Since tissue electrical impedance is a function of its structure, EIS can be used to monitor cell growth and formation of the epithelia. It is important to emphasize also the role of tight junctions, that is what we want to truly monitor to follow up on cell differentiation. Barrier integrity is vital for the physiological activities of the tissue. To successfully treat certain diseases of organs protected by physiological barriers, it is necessary to develop methods that can enable the transport of therapeutic drugs across these barriers in order to reach the target tissue. For example, in their work, Gonza´lez-Correa et al have concluded that there is a clear separation between normal squamous and columnar cells (stomach and Barrett's esophagus), also they observed different discrimination between tissues at high frequencies (Fig 1.18).

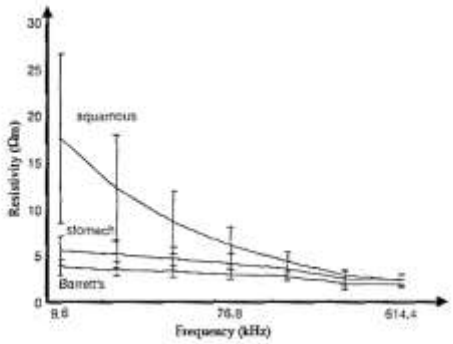

Fig1.18: Mean values of the resistivity obtained for the in-vivo measurements (redrawn from Gonz´alez-Correa et al 2000).

Cell membranes seem to interact with applied pulsed electric fields causing intramolecular transitions and intermolecular processes that lead to structural reorganization of the cell membranes.

1.7.3 A model of tissue impedance

It is known that the electrical impedance of biological tissues decreases with increasing frequency and this dependence on frequency is due to the cell membrane, which behaves like a capacitor. The extracellular and intracellular constituents of tissue can be related to the electrical equivalent circuit, as shown in Figure 1.19.

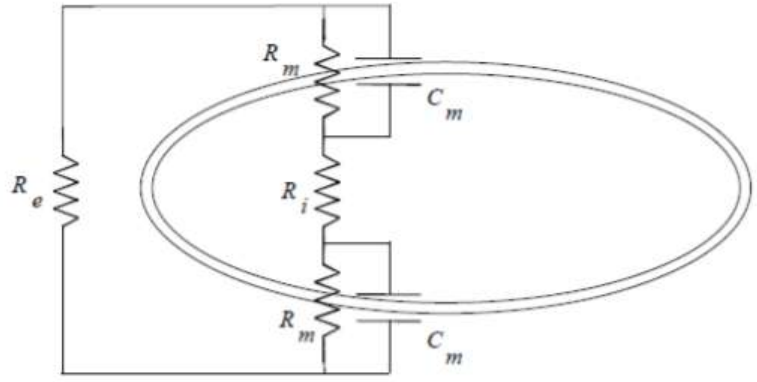

Fig. 1.19 - Diagram of the electrical cell model, where R_e is the extracellular fluid resistance, R_i is the intracellular fluid resistance, R_m is the membrane resistance and C_m is the membrane capacitance

However, this cell model does not represent the behaviour of the membrane impedance over a wide frequency range. Debye produced a similar model by considering the impedance of a suspension of free dipoles. He produced the following equivalet circuit shown in Figure 1.20, which derives from the equation below:

$$R_{TISSUE}(\Omega) = R_{TOTAL} - R_{BLANK}$$

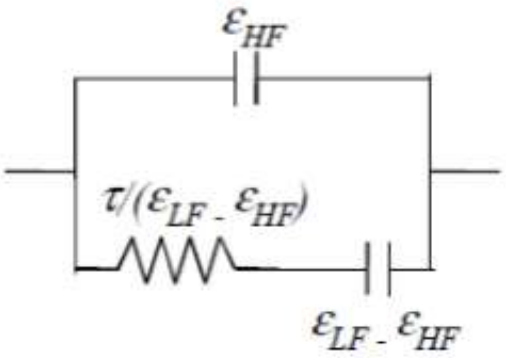

Fig. 1.20 - Equivalent circuit for the equation

However, neither the Debye model nor the cell model can predict values for the relative permittivity over a wide frequency range. Cole et al (1941) took into account dispersion by including a distribution parameter α in the equation $R_{TISSUE}(\Omega) = R_{TOTAL} - R_{BLANK}$. α can be chosen to produce a good fit between a measured spectrum and the equation below:

$$Z = \frac{V(t)}{I(t)} = \frac{V_0 sin\theta}{I_0 \sin(2\pi f t + \Phi)} = \frac{1}{Y}$$

It should be pointed out that the Cole equation is not derived from a model but is an empirical modification to the Debye equation below:

$$\varepsilon^*(\omega) = \varepsilon_{HF} + (\varepsilon_{LF} + \varepsilon_{HF}/(1 + j\omega\tau^{1-\alpha})$$

where α is the dimensionless numerical constant to fit the data. When α = 0 the two equations above are identical.

1.7.4 The electrode/tissue interface

When an electrode (i.e. metal) is connected to a solution in contact with tissues, the electrode will become positively charged and the solution negative. Charge transfer will occur until the system is in equilibrium, which means that the energy level in the solution is equal to the Fermi level in the metal (Compton et al 1996). Then, a difference in potential (or a current) between the electrode and the tissue will be measured. This type of potential is referred to as a polarization potential. Measurements of potential are possible because current flows through the electrode, but electrolysis may take place at the electrode/tissue interface. Therefore, for a current to be sustained, charge transfer across the electrode/tissue interface will be required. In order to sustain that transfer of charge across the electrode/tissue interface, an alternating current has to be applied. As a result, the movement of ions in and out of the electrode/tissue interface constitutes an alternating current into the tissue, hence an alternating potential. The electrode/tissue interface also presents an impedance due to any net flow of electrolytes. McAdams (1987) has concluded that the non-linearities of the electrode system are related to frequency dispersion of the electrode/electrolyte interface impedance as a result of different physical properties of the electrode surfaces.
An electrical model was used by McAdams (1987) to represent the electrical properties of the electrode/electrolyte interface. He derived the empirical equation below:

$$Z = Z_R + jZ_I$$

to describe the electrode/electrolyte interface impedance. Therefore:

$$Z = R_\infty + (R_0 + R_\infty/(1 + (j\frac{\omega}{\omega_c})^{1-\alpha})$$

where ω_c is the angular characteristic frequency, R_0 is the resistance at zero frequency, i.e. DC, and R_∞ is the resistance at high frequency, i.e. infinity. The polarization impedance of electrodes can become very large at very low frequencies but is less important at the frequencies considered in this thesis.

1.7.5 Equivalent circuit of tissue

An equivalent circuit analysis of the measured impedance spectrum provides the electrical parameters that can be applied to characterize the cellular barrier properties. Figure 1.21 (a) (adapted from Benson et al.) shows a typical equivalent circuit diagram that can be applied to analyze the impedance spectrum of cellular systems. In this circuit, the current can flow through the junctions between cells (paracellular route) or through the plasma membrane of the cells (transcellular route). The tight junction proteins in the paracellular route contribute to an ohmic resistance (R_{TEER}) in the equivalent circuit. Each lipid bilayer in the transcellular route contributes to a parallel circuit consisting of ohmic resistance ($R_{membrane}$) and an electrical capacitance (CC). In addition to these elements, the resistance of the cell culture medium (R_{medium}) and the capacitance of the measurement electrodes (CE) have to be considered. The high values of $R_{membrane}$ causes the current to mostly flow across the capacitor and allows an approximation where $R_{membrane}$ can be ignored and the lipid bilayers can be represented with just CC. Based on this approximation, the equivalent circuit diagram can be further simplified as shown in Figure 1.21 (b) (adapted from Benson et al.) and the impedance spectrum observed will have a nonlinear frequency dependency as shown in Figure 1.21 (c) (adapted from Benson et al.). Typically, there are three distinct frequency regions in the impedance spectrum where the impedance is dominated by certain equivalent circuit elements. In the low frequency range, the impedance signal is dominated by CE. In the mid frequency range, the impedance signal is dominated by circuit elements related to the cells, namely R_{TEER} and CC. In the high frequency range, CC and CE provide a more conductive path and the impedance signal is dominated by R_{medium}. These equivalent circuit parameters can be estimated by fitting the experimental impedance spectrum data to the equivalent circuit model using non-linear least squares fitting techniques to obtain the best fit parameters [77].

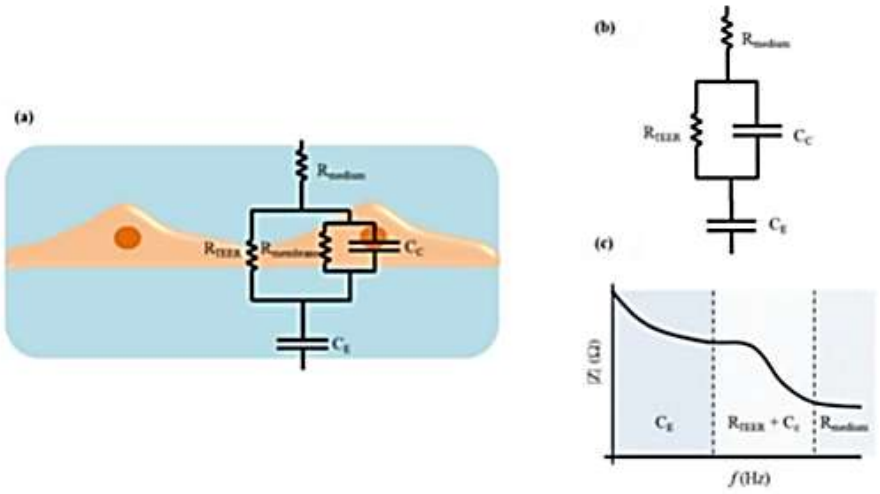

Fig. 1.21 - (a) A typical equivalent circuit diagram that can be applied to analyze the impedance spectrum of cellular systems. (b) Simplified equivalent circuit (c) A typical impedance spectrum with distinct frequency dependent regions.

1.8 Organ on chip

1.8.1 Introduction

The first requirement that has driven tissue engineering to the design/manufacture of a microfluidic chip and to the introduction of an equivalent human tissue in the laboratory, is first of all the realization of a platform for 3d culture mimicking the physiological activity, mechanisms, and response of an entire organ. These microfluidic devices are usually made of biocompatible and transparent plastic (PDMS) with chambers continously perfused and populated by living cells arranged to simulate human tissue and organ structure and physiology. By summarizing multicellular architectures, tissue-tissue interfaces, physico-chemical microenvironments, and vascular perfusion of the body, these devices produce levels of functional tissues and organs that are not possible with traditional 2D or 3D culture systems. They also allow high-resolution and real-time imaging and in vitro analysis of the biochemical, electrical, genetic and metabolic activities of living cells in a functional context of tissues and organs. This technology has great potential to advance the study of tissue development, organ physiology and the etiology of an illness [78]. The idea is to recreate the smallest functional unit of any organ in a particular microenvironment in order to imitate the human body as closely as possible. Secondly, drug testing on animal models takes time, is costly and often does not foresee the adverse effects

usually occurring in humans. It is estimated that 60% of animal models are not able to predict the real toxicity of molecules [79]. Nowadays, therefore, the development of safe and effective drugs is hindered by the poor predictive power of the preclinical response performed on animals. Therefore, by substituting animal tests or simpler tests on human cells in Petri dishes, this innovative "Organ on Chip" technology is able to accelerate the development of drugs and save millions or even billions of dollars, spent on testing drug candidates that fail in human clinical trials.

1.8.2 Lung on chip

The most important microfluidic "Lung-on-Chip" platforms developed in recent years have been realized by Donald E. Ingber, American cellular biologist and Bioengineer, founder of Harvard's Wyss Institute for Biologically Inspired Engineering University and professor of bioengineering at Harvard's John A. Paulson School of Engineering and Applied Sciences. One of his most recent innovations is a microfabrication method for the construction of small, complex three-dimensional models of living human organs. As an alternative to animal studies, the Lung-on-chips could be used to study the safety and efficacy of new drugs, speeding up the introduction of drugs into the market while reducing research costs. The first human Lung-on-chip has been reported on Science in 2010 [80].

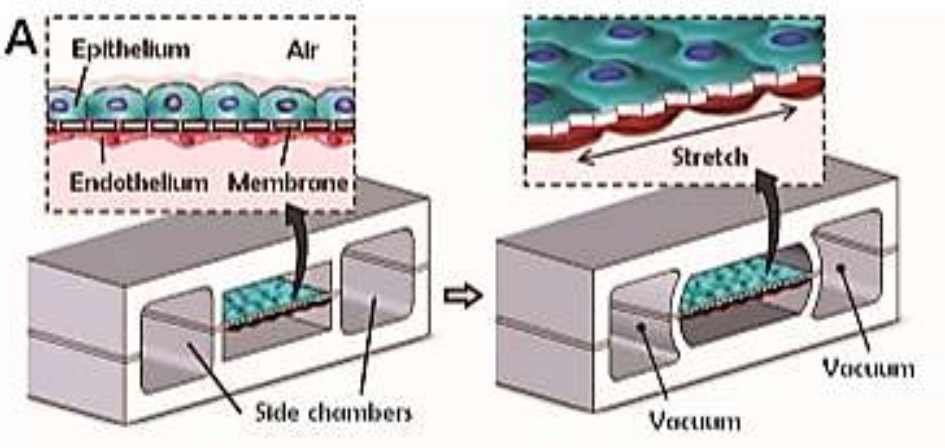

Fig. 1.22: The first model of "Lung on Chip" – 2010

Created using microchip production methods, the Lung-on-chip is a complex three-dimensional model of a respiratory lung that incorporates human lung cells living within microfluidic silicone

rubber channels. In this work, a biomimetic microsystem has been reproduced which reestablishes the alveolar-capillary functional interface of the human lung. Simulating the pulmonary contraction that occurs by inhalation and exaltation, this microchip reproduces complex responses following exposure to bacteria and inflammatory cytokines introduced in the alveolar space. In Nanotoxychology studies, this pulmonary model revealed that the mechanical cyclic movement accentuates the toxic and inflammatory responses of the lung to the silica nanoparticles. The mechanical movement also improves the epithelial and endothelial absorption of nanoparticles and stimulates their transport in the underlying microvascular channel.

In 2012, reproposing the same microchip realized in 2010 where the pulmonary respiratory action is reproduced by induced mechanical cycles, Ingber and his team demonstrated in a study on Science translational Medicine the ability to imitate a complex human disease on the Lung-on-chip, such as the pulmonary edema, commonly known as "fluid on the lungs"-and to identify new therapies using this model [81]. Specifically, this device has been used to reproduce toxicity-induced pulmonary edema in patients with human cancer treated with interleukin-2 (IL-2). This study revealed once again that the mechanical forces associated with physiological respiratory motions play a crucial role in the development of increased vascular loss leading to pulmonary edema and that circulating immune cells are not necessary for the development of this disease.

Finally, the latest innovation on lung tissue proposed by Ingber (Fig. 1.23) dates back to 2016:

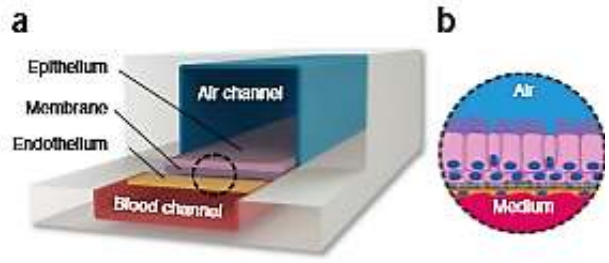

Fig. 1.23: Lung on chip 2016

In this work, the Ingber team describes the development of a "small airway on Chip" of a human lung containing a differentiated mucociliary bronchial epithelium (alveolar epithelial cells) and an underlying microvascular endothelium exposed to a fluid flow. This platform allows the analysis of lung pathophysiology at organ level in vitro by exposing the epithelium to the action of

Interleukin-13 (IL-13), thus reconstituting the hyperplasia of the caliciform cells, the hypersecretion of cytokines and the diminished ciliary function typical of asthmatics [82].

1.9 General principles of microfludics

Fluid mechanics is the branch of physics that deals with the study of properties of the fluids both in equilibrium (hydrostatic) and not (hydrodynamic). The focal point of this science is, therefore, the fluids. The nature of molecular interactions that characterize fluids plays a fundamental role in the type of approach used to study their properties. One of the most important assumptions underlying this survey is the so-called "continuum hypothesis", which allows us to study fluids as a sort of unicum composed of a very large quantity of infinitesimal elements that contribute to determining its macroscopic behavior. For the "continuous assumption" to be valid, it must be verified that the macroscopic size of the flow is incomparably larger than the length scale of intermolecular collisions. In this context, any small volume element in the fluid is supposed to be large enough to contain a large number of molecules and so the displacement of some fluid particle is that of a volume element containing many molecules, though still regarded as a point. Local properties such as density or velocity are defined as averages over large elements compared with the microscopic structure of the fluid but small enough in comparison with the scale of the macroscopic phenomena. This approach has some mathematical implications, it enables the use of differential calculus to describe density/velocity fields, for example, and a continuum fluid implies that the derivatives of all the dependent variables exist in some reasonable sense. Molecules play no role in the continuum mechanics and any macroscopic variable is an average of a corresponding molecular variable.

$$u = \frac{1}{V}\int w\, dV$$

For the "continuum hypothesis" to be valid, the volume element must be large enough with respect to the characteristic molecular length scale, considering that a 10µm channel has approximately 30,000 water molecules spanning it, the fluid particles are much smaller than a microchannel, so the "continuum hypothesis" can be applied without difficulty in this contest. The continuum hypothesis generates two independent mechanisms for momentum (as well as for heat) transfer:

1. Convective: associated with the macroscopic average velocity field.
2. Diffusive: generated by local fluctuations.

Dimensionless numbers

The dimension of any physical quantity is a formula that defines how the numerical value of the quantity changes when the base unit sizes are changed. The dimension of a quantity by itself does not provide any information on the quantity's intrinsic nature. In 1883 Osborne Reynolds first performed systematically a flow experiment in circular cross-section tubes, observing that combining the average velocity, the diameter of the tube and the kinematic viscosity in a single factor, it was possible to describe the flow dynamics.

$$R_e = \frac{Ud}{v} = \frac{U\rho l}{v}$$

where U is the average velocity, ρ is the density, l the characteristic lenght, depending on the channel's geometry, and ν the kinematic viscosity. In general, the number of Reynolds (Re) is, therefore, an adimensionary group proportional to the ratio between inertia forces and viscous forces. The dimensionless number called Reynolds number characterizes the type of flow. Low Reynolds number means negligibility of inertial forces. Other dimensionless numbers used in the study of microfluidic are the Sherwood number and the Bond number. The first one is used if we are interested in studying the diffusion effect. Infact, the Sheerwood number is the ratio of mass transfer by convection to diffusion:

$$Sh = \frac{kd}{D}$$

where k is the mass transfer coefficient, D is the diffusion coefficient, d is the channel diameter. Since in our case Sh is very small, the transport by diffusion is dominant over that of convection. The Bond number allows us to estimate how much the surface tension is dominant over the gravitational force:

$$B_o = \frac{\Delta\rho g L^2}{\gamma}$$

where Δρ is the density difference at the interface, g is the gravitational acceleration, L is the characteristic dimension of the channel and γ the surface tension.

The Navier-Stokes equations

We want to describe a fluid which is local, instantaneous, homogeneous, and isotropic. Indeed, a fluid is isotropic if the constitutive equation is unchanged by rotations of the coordinate system. If we choose a fourth gradient tensor fulfilling all these properties, we get the following Newtonian constitutive equation:

$$T = (-p + \gamma trD)I + 2\mu D$$

Where T is the stress tensor, p the pressure, D the rate-of- strain tensor, I the identity matrix. But if the fluid is incompressible we get

$$trD = \sum_{i=1}^{3} D_{ii} = 0$$

and so, the equation is reduced to:

$$T = -pI + 2\mu D$$

where μ is called viscosity. All materials are compressible to some degree. When the density remains close to a constant value the flow is incompressible. The assumption of incompressibility requires:

$$\frac{\delta p}{\rho} \approx \frac{\delta p}{\rho}\frac{d\rho}{dp} = \frac{u^2}{c^2} = M^2 \ll 1$$

Where M is the M ach number, u the velocity and c the sound's velocity. In microfluidics the flows are typically slow, the pressure changes depend on viscous effects in the liquid. In a channel with typical small dimension l = dp ≈ μu/l, hence, the assumption of incompressibility requires:

$$\frac{\delta p}{\rho} \approx \frac{\delta p}{\rho}\frac{d\rho}{dp} = \frac{\mu u}{\rho l c^2} = \frac{M^2}{R_e} \ll 1$$

In most microfluidic flows M is much smaller than Re: density variations can be neglected, but one has to be careful if the micro-channels are long, in this case a significant pressure change may occur then the density will also change. The Navier-Stokes Equations for incompressible fluid in isothermal conditions (dimensional form) is:

$$\rho\left(\frac{\partial u}{\partial t} + u\nabla u\right) = \rho g - \nabla p + \mu\Delta^2 u$$

The continuity equation is ∇u = 0. With some algebra we can derive the dimensionless Navier-Stokes equation

$$R_e\left(\frac{1}{Str}\frac{\partial u^*}{\partial t^*} + u^*\nabla u^*\right) = \rho^* g^* - \nabla p^* + \mu^*\Delta^2 u^*$$

Where x* = x/(UμL), Re = ρUL/μ, Str = T/(L/U) is the Strouhal number (Str = 1 for steady flows) and g is the gravity acceleration.

In the inertialess case Re <<1 and Re/Str << 1 from which we derive the creeping flow equations:

$$-\rho^* g^* + \Delta p^* = \mu^*\nabla^2 u^*$$

$$\nabla u^* = 0$$

The Navier-Stokes equations are generally non-linear, the creeping flow equations (also known as Stokes equations) are the linearizations of the Navier-Stokes ones. Stokes equations are the mathematical model for most of microfluidic applications, even with suspended particles.

1.10 Micro-fabrication technologies

Microfluidic devices are often produced using two polymers: PDMS (polydimethylsiloxane) and PMMA (polymethylmethacrylate or plexiglass). Both are modeled using a variant of the photolithographic process normally used for the manufacture of microelectronic devices; are generally biocompatible and chemically inert polymeric materials; and guarantee simple machining and low cost. PDMS has the benefit of optical transparency, useful in many analyses. Moreover, it is an elastomer, so there are no problems for inserting the tubes, which can simply be inserted with some interference inside holes put in the material. One disadvantage, in some specific applications, may be its permeability to oxygen. PMMA also has the advantage of radiation transparency but, unlike the PDMS, it is waterproof to gas and rigid. The second feature may be a problem for connecting to tubes in case of flow tests. Connection pipes are generally in PTFE (polytetrafluoroethylene) or silicon. The main μ-fabrication technologies showed in this chapter are: micromilling, soft lithography, photo-lithography and laser 2D. There are many other technologies, but the above mentioned are relatively simple and cheap.

1.10.1 Micromilling machine

Micromilling is a mechanical micromachining method. It is a process that utilizes microtips, see Fig. 1.24, with radii that vary from 25 µm to few mm. It consists of mechanical removal of material through the microtip, moving the work-piece axially and radially against the rotating milling cutter. It is precise, costly, labor intensive, requires highly specialized skills, equipment and facilities.

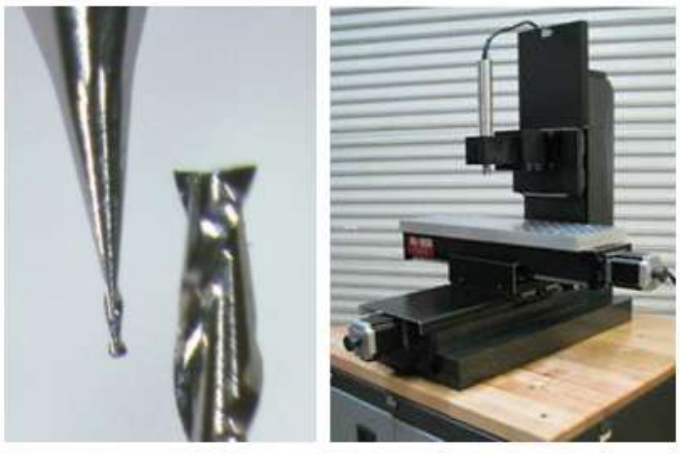

Fig. 1.24: Microtips of 25 and 200 µm (left) and micromilling (right)

The machine (on the right of fig- 1.24) allows very fine control of both the xy and z plane and gives the possibility to import CAD files with the drawing to be realized. The product obtained must be clearly cleaned from all debris with an adequate number of washes. In the figure 1.25 we can see the tip during machining.

Fig. 1.25: Tip during machining

1.10.2 Photolithography

Photolithography ("optical lithography" or "UV lithography") is the process that uses ultraviolet light (UV) to transfer a geometric pattern from a photomask to a light-sensitive chemical "photoresist" on a substrate generally made of silicone (Si). It consists of depositing a photoresist film (positive or negative) on which a lithographic mask is laid. It has the function of protecting the part of photoresist that we are not interested in developing. The entire procedure is schematized in Fig. 1.26. It is characterized by low resolutions, high cost, reduced writing areas, long fabrication time.

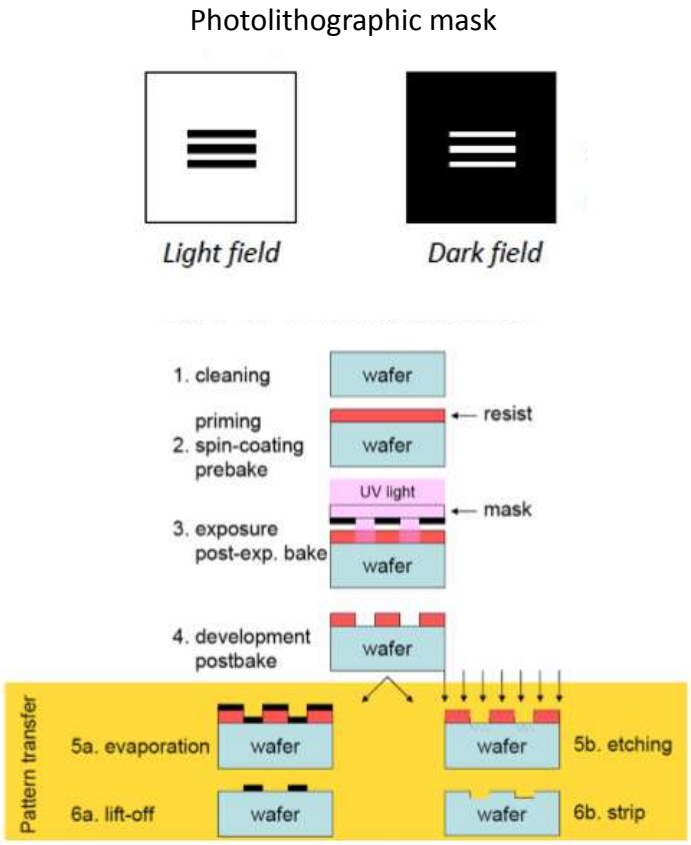

Fig. 1.26: Photolithograpic process

1.10.3 Laser 2D

With this technique, we can do the same thing of the photolithography but without the need of a mask. That's because the laser inscribes directly on the photoresist film deposited on the plate to

be treated. The following steps are the same as photolithography with mask, namely: chemical or physical attack of the substrate, removal of the remaining fotoresist.

1.10.4 Soft-lithography

Soft lithography refers to a family of non-photolithographic techniques to fabricate microstructures and replicate them using a patterned material. The use of the term ”soft” originates from the elastomeric (soft) polymers like (PDMS). These techniques include Replica Molding, MicroMolding In Capillaries, MicroTransfer Molding and MicroContact Printing.

1.10.5 Replica Molding

Replica molding allows duplication of 3D topologies in a single step, it has a 30 nm resolution. The use of elastomers facilitates the release of small fragile structures (Fig 1.27).

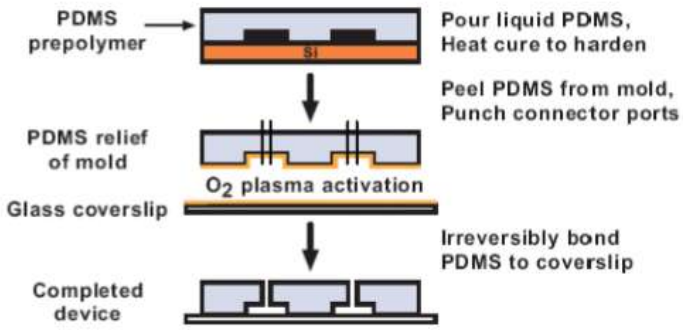

Fig.1.27: Replica molding process

1.10.6 Microtransfer Molding

Here, the master is made of PDMS and it is filled with a prepolymer and placed on a substrate. Similarly to the techniques shown before, the polymer is cured and the master is removed. With this technicque it is possible to generate multilayer structures. It has a 250 nm resolution.

1.10.7 MicroMolding in Capillaries

Here, we have continuous channels formed upon contact of PDMS master with substrate, a polymer precursor fills channels with capillary action, then the polymer is cured and master is removed. It has a 1 µm resolution.

1.10.8 MicroContact Printing

Here, an “ink” is spread on a patterned PDMS master, the master is then brought into contact with the substrate of interest. The “ink” is then transferred to the substrate, where it can act as a resist against etching, it can also be a selfassembled monolayer or a biological sample. It has a 300 nm resolution.

Chapter 2

Development of a novel tridimensional cystic fibrosis model \featured by endogenous extracellular matrix

2.1 Introduction

Cystic fibrosis (CF) is a genetic disease caused by mutations in the cystic fibrosis transmembrane conductance regulator (CFTR) gene. CFTR is a chloride channel primarily located at the apical surface of epithelial cells in different organs playing a fundamental role in trans-epithelial fluid homeostasis [83]. Gene mutations can reduce channel number or function; the most common CFTR mutation is the deletion of the phenylalanine at position 508 (ΔF508) which is associated with defective protein folding resulting in proteosomic degradation and very little or no CFTR reaching the apical membrane of the epithelium. CFTR dysfunction affects many organs but lung disease is responsible for most of severe complications in patients with cystic fibrosis. As result of defective anion secretion, cystic fibrosis patients display a chronic respiratory disease characterized by mucus obstruction and bacterial colonization of the airway [84]. Moreover, the host inflammatory response in CF lung disease has been recognized as a central pathological feature and an important therapeutic target. It is still unclear if the inflammatory response can be directly attributable to CFTR impairment or only secondary to airway obstruction and chronic bacterial infection [85,86]. During the chronic disease, tissue damage and inflammation could trigger fibrosis and matrix remodeling. Significant airway remodeling is a major component of the increased morbidity and mortality observed in cystic fibrosis patients [87,88]. Despite the continuous development of new therapeutic strategies, the genetic and clinical heterogeneity of patients with CF imposes a personalized medicine approach. To this end, in vitro models have been developed using cells collected from individual patients. with the aim to study pathogenic mechanisms underlying the chronic respiratory diseases and develop appropriate therapeutic strategies. Usually, airway epithelia are studied in vitro by seeding bronchial or nasal epithelial cells at high density on porous membranes and inducing their differentiation by placing the cells under air-liquid interface (ALI) conditions. After 2-3 weeks under ALI condition, cells generate a tight epithelium with cilia and other features of the tissue in vivo. Crosstalk with the underlying

connective tissue, mediated by soluble factors or cell-substrate interaction, has important consequences on the differentiation and function of the epithelium and the response/adaptation to physiological stimuli and noxious events. In this perspective we established in the IIT@CRIB lab a novel tissue engineering approach to build-up organ in vitro. By following such strategy, we produced different organ models (i.e. skin [7,37], cervix [8]). Our results clearly demonstrated the fundamental role of the connective tissue in guiding in vitro epithelium morphogenesis. Using a similar method we developeded a full thickness cystic fibrosis model of the airway. We argue that such model may be useful to study the effects of therapeutic strategies focused not only on epithelial but also on stromal response into a dynamic environment representative of the native human condition [89].

2.2 Material and methods

2.2.1 Cell culture

Normal/Cystic fibrosis human lung fibroblast were purchased by Lonza (NHLF CC-2512 and DHLF-CF CC-194843, respectively). Cells were cultured in Minimum Essential Medium (Sigma-Aldrich M2279) supplemented with 20% FBS (Sigma-Aldrich F7524), 2% of Non-Essential Aminoacids (EuroClone ECB3054D), 1% of L-Glutamine (MICROTECH X0550) and 1% of penicillin/streptomycin (Sigma-Aldrich P4333), until passage 4/6. Normal/Cystic Fibrosis Human bronchial epithelial cells (respectively, NA-HBEC/CF-HBECs ΔF508) were provided by the Primary Cell Culture Facility of the FFC (Istituto G. Gaslini, Genova). Cells were seeded in flasks pre-coated with Rat tail collagen and expanded using the LHC9/RPMI164 serum-free medium[90] until P3/4.

2.2.2 Microscaffold production

Gelatin porous microbeads (GPMs) were prepared according to a modified double emulsion protocol (O/W/O) [91]. GPMs were stabilized by crosslink reaction with glyceraldehyde (GAL) (SIGMA-G5001), in order to make them stable in an aqueous environment at 37°C [36]. GAL at 4% w/w of the microbeads was used for all experiments.

2.2.3 Building of human Lung microtissue (µTP) precursors

Approximately 10 NHLF/DHLF-CF P4/6 were seeded for micro-scaffold into a spinner flask bioreactor (Integra). Cells were cultured under continuous agitation (30 rpm) after 6 hours of intermitting stirring regime in order to promote cell seeding (30 min at 0 rpm, 5 min at 30 rpm). The culture medium was enriched MEM plus Ascorbic Acid (2-O-α-D-Glucopyranosiyl-L-Ascorbic-Acid TCI G0394-5G; Cf: 0.5mM). Normal airway µTPs (NA- µTPs) and Cystic fibrosis µTPs (CF- µTPs) were cultured for 21 days before the phase of assembly in order to guarantee the initial collagen synthesis. NA- µTPs and CF- µTPs were sampled during the culture period in order to monitor cell growth and the synthesis of elements of the extracellular matrix. Micro-tissue diameter was quantified using optical images and Image J measurement plugin. At different time points, micro-tissues were digested using trypsin/collagenase type A and cell number was counted using the Neu Bauer chamber.

2.2.4 3D Assembly of human Connective Airway tissue (CAT)

The CAT was engineered by using a previously described bottom-up approach [92]. NA-µTPs/CF-µTPs were transferred from the spinner flask to a maturation chamber in order to allow their molding in disc-shaped construct (usually 1 mm in thickness and 10 mm in diameter but also different shapes and dimensions). The chamber was a sandwich-like structure with in the middle a silicon mold with empty spaces for the µTPs housing. The silicon mold was delimited on both the top and bottom sides by two stainless steel rigid grids characterized by a porous mesh (18 µm) that was able to retain the µTPs and to guarantee the passage of nutrients and waste products. Two polytetrafluoroethylene (PTFE) rings were placed on the grids on both sides. The system was closed by means of stainless-steel screws passing across the PTFE rings and bolts. The chamber was placed on the bottom of a spinner flask (Bellco biotechnology code 1967- 00050) and completely surrounded by culture medium. The tissues were cultured in dynamic condition at 60 rpm. The culture medium was enriched MEM plus Ascorbic Acid. After 3/4 weeks of culture the assembling chamber was opened and Normal airway connective tissue (NA-CAT) and Cystic Fibrosis connective tissue (CF-CAT) were collected for the sample analysis or for the production of the full thickness model.

2.2.5 Fabrication of a human Bronchial full tickness model (FT)

After 3/4 weeks of maturation the sandwich-like chamber was opened and the NA-CAT/ CF-CAT was placed on a Snapwell insert (Corning 3801- diameter 12mm, porosity 0.4 μm) in order to seed NA-HBEC/CF-HBECs ΔF508 respectively on the surface of the NA-CAT/ CF-CAT. The CAT surface was coated using 50 μg/ml human fibronectin (Sigma Aldrich F0895). The coating was performed with a minimal volume of about 10 μl of fibronectin. Samples were left under hood, at Room Temperature (RT), for 40 minutes and into the incubator, at 37°C, for 10 minutes. Meanwhile HBECs were detached using the protocol supplied by the Primary Cell Culture Facility of the FFC (Istituto G. Gaslini, Genova). About 4.400 cells/mm^2 were seeded on the surface of the CAT, cells were suspended in about 10 μl of LHC/RPMI medium in order to avoid drop falling. After 1 hour the sample was submerged with the medium LHC/RPMI. From the day after the seeding, the serum free LHC/RPMI medium was replaced by the DMEM/Ham's F12 medium containing 2% New Zealand fetal bovine serum, according to the protocol used for classical epithelial differentiation in Snapwell [90]. Sample were cultured for 1 week in submerged culture and 2 weeks in air-liquid condition.

2.2.6 Multiphoton analysis

For SHG imaging, samples were examined by confocal microscopy (TCS SP5 II Leica) combined with MPM where the NIR femtosecond laser beam was derived from a tunable compact mode-locked titanium: sapphire laser (Chamaleon Compact OPO-Vis, Coherent). Two-photon excited fluorescence was used to induce SHG and obtain high-resolution images of unstained collagen structures. The samples were observed by using λ_{ex} = 840 nm (two photons) and λ_{em}=415-425 nm. The SHG images were acquired with a resolution of 12 bit, 512x512 pixel by using a 25X water immersion objective (HCX IRAPO L 25.0X0.95 Water, n.a. 0.95).

2.2.7 Collagen fraction quantification

In order to quantify the collagen fraction, SHG images were analyzed by using the ImageJ software. ROIs in the stroma compartment were chosen by excluding the signal of the micro-scaffold. The Collagen Fraction (%) was defined as percentage of the ratio between bright pixels to total pixels in each selected ROI.

$$\text{Collagen Fraction}(\%) = \frac{\text{Nc}}{\text{Nb} + \text{Nc}} * 100$$

Nc and Nb represent the number of pixels from the collagenous and non-collagenous portion, respectively.

2.2.8 Gray-level co-occurrence matrix analysis: correlation

The gray level co-occurrence matrix (GLCM) analysis was performed using the ImageJ plugin Texture on SHG images as previously described [93]. The correlation was calculated for distances ranging from 1 to 100 pixels in the horizontal and vertical direction of each optical section. In such spatial windows the distance at which the correlation functions fall off represents the correlation length of the texture. Correlation length was obtained by fitting data with an exponential low.

2.2.9 Immunofluorescence on tissue sections

Samples were fixed with Formalin (10%) (HT501320 Sigma) for 1 hour at Room Temperature (RT) and washed with PBS1X (P4417-100TAB Sigma). They were dehydrated in Ethanol from 75% to 100% and treated with Xylene (A9982 ROMIL) before Paraffin inclusion. Tissue slices, 7µm thick, were cut using a microtome (Thermo Scientific HM 355S) and then deparaffinized using xylene. Sections were hydrated in ethanol from 100% to 75% and washed in water, 0,2% Triton and 1X PBS. In order to release the epitopes from paraffin, for all the antibodies unless Hyaluronic Acid, heat mediated citrate buffer (pH=6, Thermo scientific TA-125-PM1X) unmasking was performed. To release the epitopes for the detection of Hyaluronic Acid, an enzymatic unmasking was performed rinsing the slices in a solution with $CaCl_2$ (1.02378.0500 Merck) and Trypsin (215240 DifcoTM Trypsin 250) at a final concentration of 0,01% in 1X PBS (pH 7.8) for 20 minutes at 37 °C. The sections were then washed with PBS (1X), blocked using BSA (6%), FBS (5%), $MgCl_2$ (20mM) and Tween20 (0,02%) in PBS (1X) for 2 hours at RT and incubated with the primary antibodies over night (ON) at 4°C in a humid environment. Table 1 indicates the antibodies used for immunofluorescence. The morning after, samples were washed in PBS (1X) and the secondary antibodies (Alexa Fluor, Table2) diluted with PBS (1X) were added for 1,5 hour at RT. Nuclei were stained with DAPI and samples were iexamined by Confocal Leica TCS SP5 II.

Antibody	Code	Working dilution
Alpha tub (Anti-Rabbit)	ab15246	1:100
CK 19 (Anti-Rabbit)	ab15463	1:100
CFTR (Anti-Mouse)	570, A2 Chapel Hill	1:200
ColII (Anti-Rabbit)	ab34710	1:500
Hyaluronic Acid (Anti-sheep)	ab53842	1:50
P63 (Anti-Mouse)	Invitrogen 4B1E12	1:50
Periostin (Anti-Rabbit)	ab14041	1:100

Table 1

Secondary Antibody	Code	Working dilution
488 Goat anti-Mouse	A11001	1:500
488 Goat Anti-Rabbit	A11008	1:500
546 Donkey Anti Rabbit	A10040	1:500
546 Donkey Anti-Sheep	A21098	1:500

Table 2

2.2.10 Protein quantification by image analysis

Ten images per sample were acquired in different points of the 3D tissue and analyzed by using ImageJ. In order to estimate the quantity of protein per cell, the area relative to the fluorescent protein signal was thresholded, quantified (in μm^2) and divided for the number of cells obtained by counting cell nuclei stained by DAPI with Analyze particle [89].

2.2.11 Mechanical properties

The mechanical properties of CAT (10 mm diameter and 1mm thickness) were analyzed by Piuma Nano-Indenter (Optics) showed in figure 2.1. Indentation is a versatile, quantitative and non-destructive technique for measurements of tissue mechanical behavior. Based on the indentation of surfaces using probes with a well-defined geometry, the elastic and viscoelastic constants of the examined materials can be determined by relating indenter geometry and measured load and displacement to parameters which represent stress and deformation. In particular, commercially available indentation instruments have led to the optimization of testing and analyzing methods

for monitoring elastic and plastic proprieties of materials, such as elastic modulus and hardness. For these reasons, the constitutive response of soft tissue and biomaterials differs from that of linearly elastic and isotropic engineering materials. First, the former generally exhibit non-linear stress-strain (σ−ε) behavior; second, their mechanical response is often characterized by a significant time-dependence, which is typically described by empirical parameter viscoelastic models; third, these materials are likely to be both microscopically and microscopically anisotropic, especially in case of biological tissue.

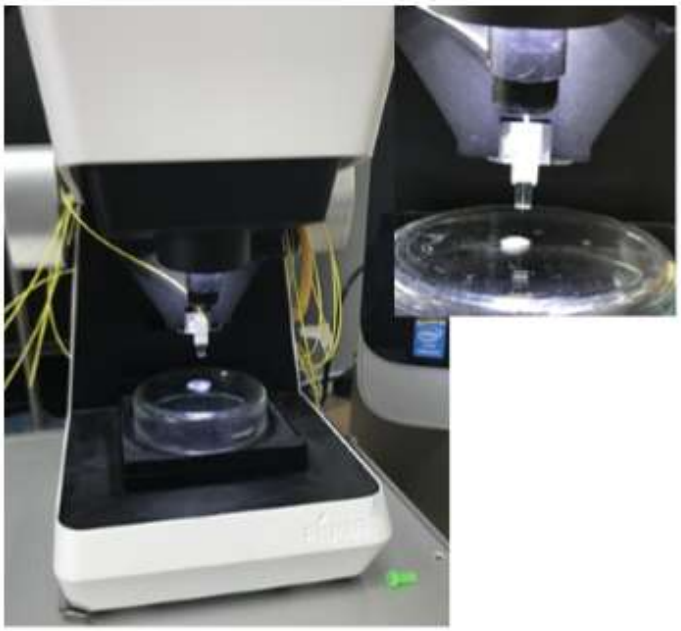

Fig. 2.1 - Piuma Nano-Indenter (Optics)

Piuma is a displacement-controlled nano-indenter machine including a controller, an optical fiber and a spherical probe. The probe is attached to a spring cantilever that is connected to the end of an optical fiber in order to measure the cantilever deflection. Each sample was indented using a cantilever with a stiffness of 4.53 Nm^{-1}. The indentation depth was approximately 10 µm during each indentation test performed in 5 different points of each sample. The tip radius was 53.5 µm and the connected optical fiber measured the cantilever deflection during indentation. Based on the indentation of surfaces using probes with a well-defined geometry, the elastic and viscoelastic constants of examined materials can be determined by relating indenter geometry and measured load and displacement to stress and deformation. The analysis of spherical nano-indentation data is generically based on the *Hertz model*, assuming a linear elastic and isotropic material response.

In order to characterize material viscoelastic and anisotropic proprieties like biological tissue and to study the analysis of spherical nano-indentation data, we used the Hertz model and a variant of the nano-epsilon method (M) [94].

The elastic modulus (E) was obtained as ratio between the indentation stress (σ *ind)* (3) and strain *(ε ind),* as described by following formulas.

$$E = \frac{\sigma\ ind}{\varepsilon\ ind}$$

$$\sigma\ ind = \frac{P}{R\sqrt{hR}}$$

$$\varepsilon\ ind = \frac{4h}{3R(1 - v^2)}$$

where P was the load, R the radius of spherical indenter tip, and h the penetration depth.

2.2.12 RNA extraction

3D CATs were collected, washed and digested with Trizol (Thermo Fisher Scientific) on a vortex by using a stainless-steel bead and then passing the solution into a syringe needle. After homogenization, samples were treated with 200 µl of chloroform, vortexed and centrifuged at 12000 rcf for 10 minutes. Five hundred µl of isopropanol were added to the upper phase. Samples were incubated for 10 minutes at RT and centrifuged at 12000 rcf for 10 minutes. After the removal of the surnatant, pellets were washed with 1 ml of EtOH (75%), centrifuged for 10 minutes at 7600 rcf and then resuspended in 100 µl of RNase- free water. To perform RNA precipitation, 100 µl of acid phenol-chloroform were added to the sample. After a centrifugation of 15 minutes at maximum speed, 9 µl NaAC (3M) and 250µl EtOH (100%) were added to the upper phase. Samples were vortexed and incubated at - 80º for 1 hour. Then, tubes were centrifuged for 15 minutes at maximum speed (4º C). After removing the supernatant, the pellet was resuspended in RNase- free water. To further clean the RNA sample from collagen debris, the

solution was transferred into the column of the High Pure RNA Tissue Kit (Roche), centrifugated at the maximum speed. RNA was eluted with 20 µl of RNase-free water. Similarly, 2D samples were extracted by using the same protocol excluding the phase of tissue homogenization [89].

2.2.13 QuantSeq 3' mRNA sequencing library preparation

Preparation of libraries was performed with a total of 100 ng RNA from each sample using QuantSeq 3'mRNA-Seq Library prep kit (Lexogen, Vienna, Austria) according to manufacturer's instructions. Total RNA was quantified using the Qubit 2.0 fluorimetric Assay (Thermo Fisher Scientific). Libraries were prepared from 100 ng of total RNA using the QuantSeq 3' mRNA-Seq Library Prep Kit FWD for Illumina (Lexogen GmbH). The quality of libraries was assessed by using screen tape High sensitivity DNA D1000 (Agilent Technologies). Libraries were sequenced on a NovaSeq 6000 sequencing system using an S1, 100 cycles flow cell (Illumina Inc.). Amplified fragmented cDNA of 300 bp in size were sequenced in single-end mode with a read length of 100 bp.

Illumina NovaSeq base call (BCL) files are converted in fastq file through bcl2fastq *[http://emea.support.illumina.com/content/dam/illuminasupport/documents/documentation/software_documentation/bcl2fastq/bcl2fastq2-v2-20-software-guide-15051736-03.pdf]* (v2.20.0.422).

2.2.14 QuantSeq 3' mRNA sequencing data processing and analysis

For analysis, sequence reads were trimmed using the bbduk software (*https://jgi.doe.gov/data-and-tools/bbtools/bb-tools-user-guide/usage-guide/*) to remove adapter sequences, poly-A tails and low-quality end bases (regions with average quality below 6). Alignment was performed with STAR 2.6.0a3 [95] on hg38 reference assembly obtained from cellRanger website (https://support.10xgenomics.com/single-cell-gene-expression/software/release notes/build#GRCh38_3.0.0; Ensembl assembly release 93). Expression levels of genes were determined with htseq-count [96] using Gencode/Ensembl gene model [97]. We filtered out all genes having < 1 cpm in less than n_min samples and Perc MM reads > 20% simultaneously. Differential expression analysis was performed using edgeR [98], a statistical package based on generalized linear models, suitable for multifactorial experiments. The threshold for statistical significance

chosen was False Discovery Rate (FDR) < 0,05: in details, 2005 genes were differentially expressed (1179 genes induced and 826 inhibited) in the 2D dataset (GSE141535), while 1505 genes were differentially expressed (968 genes induced and 537 inhibited) in the 3D dataset (GSE141536).

1406 transcripts were specifically regulated in the 2D condition (779 up-regulated and 627 down-regulated), 906 transcripts were specifically regulated in the 3D condition (554 up-regulated and 352 down-regulated), 559 DEGs were commonly regulated (381 up-regulated and 166 down-regulated in both datasets and 52 regulated in opposite manner). Gene Ontology (GOEA) and Functional Annotation Clustering analyses were performed using DAVID Bioinformatic Resources [99,100] restricting the output to Biological Process terms (BP_FAT). Cellular Compartment terms (CC_FAT) and Molecular Function terms (MF_FAT). The 'Kyoto Encyclopedia of Genes and Genomes' (KEGG Pathway) analyses [101–103] was also performed. The threshold for statistical significance of GOEA was FDR<0,1 and Enrichment Score ≥1.5, while for the KEGG Pathway analyses was FDR<0,1. The GOEA was performed on the induced genes in the two datasets separately and after the comparison on the commonly up-regulated and on the specifically up-regulated gene lists. The additional threshold of logFC > 2 for induced and logFC < -2 was used for the list of DEGs obtained in the two datasets separately. In details, the DEGs induced into the 3D dataset were 487, while the DEGs induced into the 2D dataset were 459.

2.2.15 Accession codes

The whole set of results is available in the GEO database as SuperSerie code GSE141537. The title of the SuprSeries is "Transcriptome profile of Primary Human Lung Fibroblasts (Cystic Fibrosis *vs* Non-Cystic Fibrosis)". In details: 1) GSE141535 refers to expression data from Primary Human Lung Fibroblasts (Cystic Fibrosis *vs* Non-Cystic Fibrosis) in 2D condition; 2) GSE141536 refers to expression data from Primary Human Lung Fibroblasts (Cystic Fibrosis *vs* Non-Cystic Fibrosis) arranged in a 3D model of the connective airways tissue [89].

2.2.16 Scanning electron microscopy (SEM)

Samples were fixed with Glutaraldehyde/ Perfluorocarbon (PFC/OsO4) followed by critical point drying (CPD-300 Leica). Then, they were mounted onto metal stubs and then coated with 100 A

ultrathin gold layer (thickness 7-15 nm) in a glow-discharge coater to minimize charging and increase the conductivity of the biological material (sputter coater Cressington_HR 208). Images were acquired using InLens and SE2 detectors (SEM, FEG_Ultrapluss by ZEISS).

2.2.17 Immunofluorescence and staining of the whole sample

Samples were fixed with 4% Paraformaldehyde (P61148-500g Sigma Aldrich) for 30 minutes at RT and washed with PBS (1X). They were permeabilized using 0,1% Triton (Triton® X-100 T9284-100ML Sigma) in PBS (1X) for 5 minutes at RT, washed with PBS (1X) and blocked using a solution with 3% BSA (A9418-100G Sigma) and 3% FBS (F7524 Sigma) diluted with PBS (1X) for 1 hour at RT. Tissues were incubated in presence of the primary antibody against Alpha-Tubulin, diluted in blocking solution, at 4°C in the dark. The following morning, samples were washed and a Donkey Anti Rabbit IgG (H+L) Alexa Fluor 546 (A10040, diluted 1:500 in 1X PBS) was added for 1,5 hour at RT. The actin cytoskeleton was stained using 488 Phalloidin (Thermo Fisher Scientific A12379) 1:200 diluted with PBS. The cell nuclei were stained with 4',6-diamidino-2-phenylindole (DAPI Sigma-Aldrich D9542) 1:10.000 diluted with PBS (1X) for 20 minutes at RT. Samples were examined by Confocal Leica TCS SP5 II. Images and z stack were analyzed using *Image J*.

2.2.18 Histology

Samples were fixed with Formalin (10%) (HT501320 Sigma) for 1 hour at RT and washed with PBS (1X). They were dehydrated in Ethanol from 75% to 100% and treated with Xylene (A9982 ROMIL) before the inclusion in Paraffin. Tissue slices, 7 µm thick, were cut using a microtome (Thermo Scientific HM 355S) and then deparaffinized using xylene. Sections were hydrated in ethanol from 100% to 75%, washed in water and stained using Masson's trichrome (HT15-1KT Sigma-Aldrich), Hematoxylin/Eosin (Bio Optica W01030708) or Alcian Blue (101647 Millipore). Sections were mounted with Histomount Mounting Solution (Bio Mount HM 05-BMHM500 Bio-Optica) on coverslips and the morphological features of the tissues were observed with a light microscope (Olympus, BX53).

2.2.19 Multiple Particle Tracking (MPT)

Recovery of mucus

Mucus was recovered from epithelia kept in culture for 3 weeks. Seventy two hours before mucus collection, the apical surface was washed twice with PBS and 120 µl of the same solution was left. After 72 hours all the PBS from the apical side (it contains the mucus produced by cells) was retrived and moved it into an eppendorf tube. All experiments were conducted on healthy mucus and CF mucus, produced by the full tickness models and the epithelium in Snapwell. Epithelial mucus was carefully aspirated from the apical and weighted surface. If not used immediately, samples were frozen and stored at -20°C.

Micro-rheology

To study the microscopic properties of mucus, Multiple Particle Tracking (MPT) was used. MPT consists in following the movement of suspended nanospheres inside the medium to be studied (mucus). The physical background of the method lies in the thermal motion of the tracer particle, which can be connected to the viscoelastic properties of the local environment through the generalized Langevin equation[104]. For MPT experiments, 0.01% polysterene carboxylated yellow/green fluorescent beads of 200 nm diameter (λecc = 488 nm, λem = 505-515 nm; Fluospheres, Life Technologies) were added to the PBS containing the mucus and softly mixed. A sample of 30 µl of the solution with mucus and fluorescent particles were sandwiched on a 35mm FluoroDish and were covered with a glass (d=2cm) to avoid evaporation. Before starting the acquisition, the samples were maintained at RT for 15 minutes to let the mucus to equilibrate and relax.

The microscope was focused to the mid-height of the sample to exclude beads that might be interacting with the coverslips or to avoid bubble air at the edges. Beads positions were recorded with an inverted Olympus microscope with a 60 X (N.A. = 1.42) oil immersion objective connected to a CCD video camera (Photometrics), yielding a final spatial resolution of ~0.1 µm/pixel. Images were captured using the MetaMorph software (Molecular Devices) at a rate of 10 frames per second, 1392 x 1040 pixels of resolution. Video files were analysed using the ImageJ software. These beads are smaller than 1 µm so that they undergo Brownian motion, as inertial forces (gravity) are negligible. Then, they are subjected to two main forces, the random force created by the thermal energy k_BT and the counteracting frictional force proportional to the velocity of the

bead and the bead's friction coefficient, which depends on the viscoelastic properties of the living cell and the size of the bead. By using a video particle nano-tracking, the particle's displacements were tracked. To generate the point tracking trajectories, algorithm has to perform two distinct steps: first, it has to detect the points in each frame and, then, it has to link this point detection into trajectories. Using a Matlab® code, each position was determined by intensity measurements through its centroid, and it was compared frame by frame to produce trajectory for each particle, based on the principle that the closest positions in successive frames belong to the same particle (proximity principle). The movement of many (several hundreds) fluorescent beads within the mucus in a given time interval, τ, is described by its mean squared displacement, <msd>, from which it is possible to calculate D_0, the diffusion coefficient.

Once obtained nanoparticles trajectories, mean squared displacements (MSDs) were calculated with this expression:

$$msd(\tau) = < \Delta r^2(\tau) > = < [x(t-\tau) - x(t)]^2 + [y(t-\tau) - y(t)]^2 >$$

where <> means time average, τ is the time scale and t the elapsed time.

The displacement of beads in pure viscous solutions, guided only by a diffusive motion, gives a <msd(τ)> which shows a linear dependence on the time interval τ of the form

$$<\mathrm{msd}(\tau)> = 4\ \mathrm{D_o}\ \tau$$

Differently, if the solution has also an elastic component, as in the case of mucus, the trajectory of beads displays a non-linear τ-dependence of <msd> of the form

$$<\mathrm{msd}(\tau)> = 4\ \mathrm{D_o}\ \tau\ \alpha$$

where $0 < \alpha < 1$.

The diffusion coefficient for a spherical particle is related to the viscosity of the solution through the Stokes-Einstein relation:

$$D_0 = \frac{k_B T}{6\pi\mu a}$$

where k_B is the Boltzmann constant, T the temperature, μ the viscosity of the medium and the radius of the diffusing particle. The dimension of the diffusion coefficient is m^2/s.

Consequently, from D_0 it will possible to calculate the viscosity of the medium in which the particle is moving as follow:

$$\mu = \frac{2k_B T}{3\pi a}\frac{\tau\alpha}{\langle msd\rangle}$$

2.2.20 Statistical analysis

Morphological experiments were performed in triplicate. Data were expressed as mean ± SD. Differences between groups were determined using the statistic test ANOVA Tukey HSD test. Significance between groups was established with a *p value < 0,05 or **p value < 0.01.

Transcriptomic analyses were performed in triplicate (3D) or quadruplicate (2D). Only DEG with False Discovery Rate (FDR) < 0.05 were considered as statistically relevant.

2.3 Results

The bottom-up approach of tissue engineering [105] was optimized in order to obtain the lung-bronchial tissue *in vitro* as described in Materials and Methods (paragraph 2.2). Each phase of the process is schematically represented in Fig. 2.4.

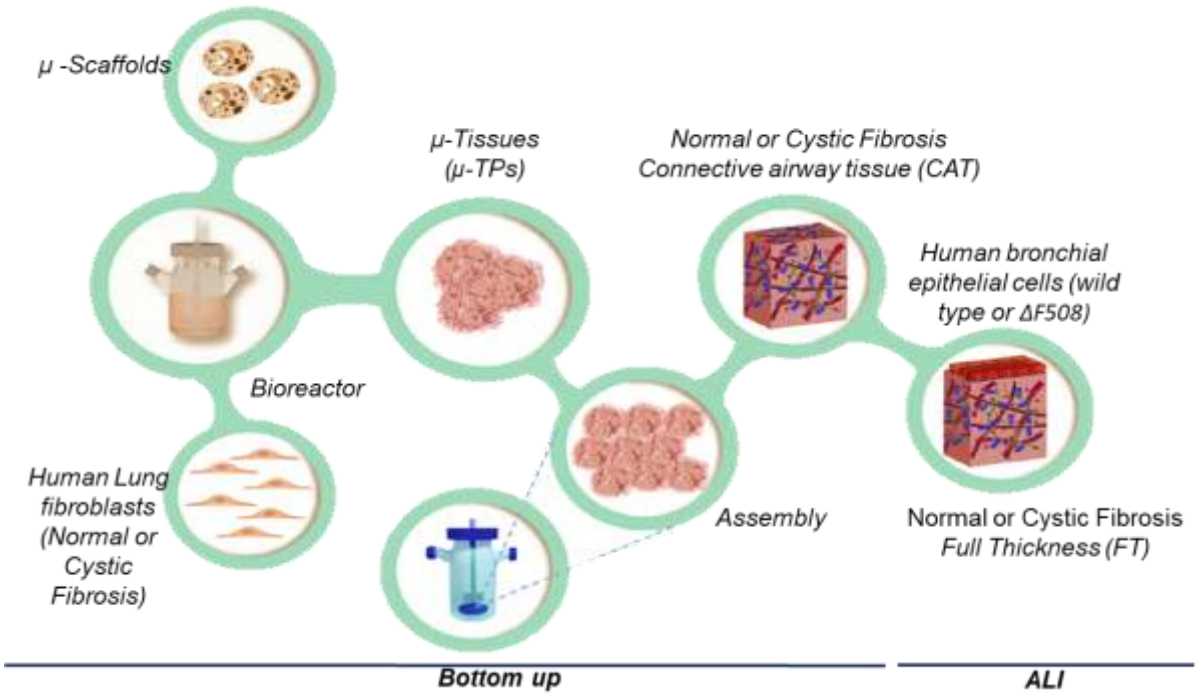

Figure 2.4 - Tissue engineering approach for the development of the 3D CF model:

Schematic representation of the bottom up approach and Air Liquid Interface used to develop the 3D Cystic Fibrosis model.

Specifically, human pulmonary fibroblasts (primary cells collected from adult patients of similar age, with or without cystic fibrosis, available from Lonza) were seeded on porous gelatin microspheres crosslinked using 4% glyceraldehyde (m / m) into spinner flasks bioreactors. In dynamic culture condition, the cells were able to adhere on the surface and into the holes of the scaffolds, and then to replicate and produce elements of the Extra Cellular Matrix (ECM). Due to cell-cell and cell-matrix interactions, each unit containing scaffolds, cells and ECM was able to bind with another and so on, up to the formation of the so-called micro-Tissue Precursors (μTPs). Subsequently, the μTPs were assembled into specific maturation chambers in order to obtain the macro-Tissue or Connective Airway Tissue (CAT), Normal or Cystic Fibrosis (NA-CAT and CF-CAT, respectively), depending on the fibroblasts used to develop the tissue. Human Bronchial Epithelial Cells (HBE), normal or CF, were seeded on a surface of the NA-CAT and CF-CAT. After 1 week of submerged culture and 2 weeks of air-liquid interface (ALI), it was possible to obtain the full

thickness models (Normal Full Thickness Airway or FT-NA and Cystic Fibrosis Full Thickness Airway or FT-CF) featured by the presence of a differentiated epithelium on a lung connective tissue enriched in ECM elements produced by pulmonary fibroblasts. Each phase of the aforementioned approach was analyzed in order to identify significant differences between the normal and CF model. The following paragraphs describe the results obtained from the analysis of the µTPs, CAT and Full Thickness model.

2.3.1 Micro-Tissues (µTPs) characterization

We initially evaluated the capability of both Normal and Cystic Fibrosis Human Lung fibroblasts [89](N-HLF and CF-HLF) to produce endogenous collagen *in vitro* by stimulating 100% confluent cell layer with ascorbic acid for 1 week. Figure 2.5 shows the *de novo* synthetized matrix in gray, visualized by the Second Harmonic Generation (SHG) signal of endogenous collagen fibers.

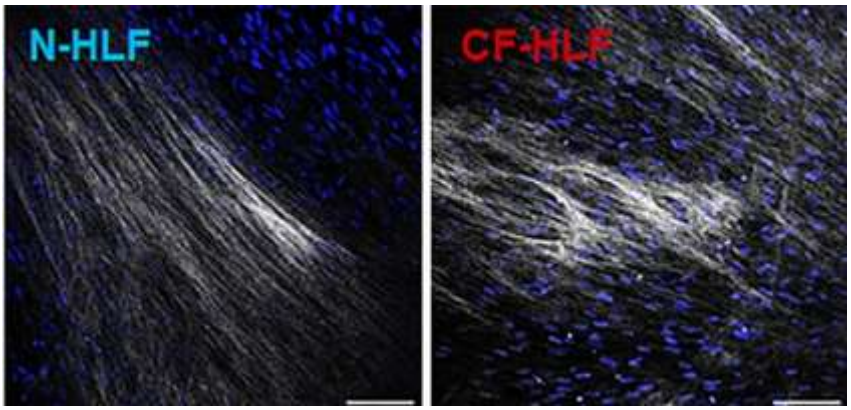

Figure 2.5 - SHG analysis of N-HLF and CF-HLF sheets: In green the endogenous collagen produced by fibroblasts and in blue the nuclei of the cells. Scale bar 100µm.

Then, N-HLF and CF-HLF were used for the formation of the µTPs, as described in the previous paragraph. Both micro-tissues featured the presence of the cells embedded into the endogenous collagen matrix as showed in Figure 2.6 A.

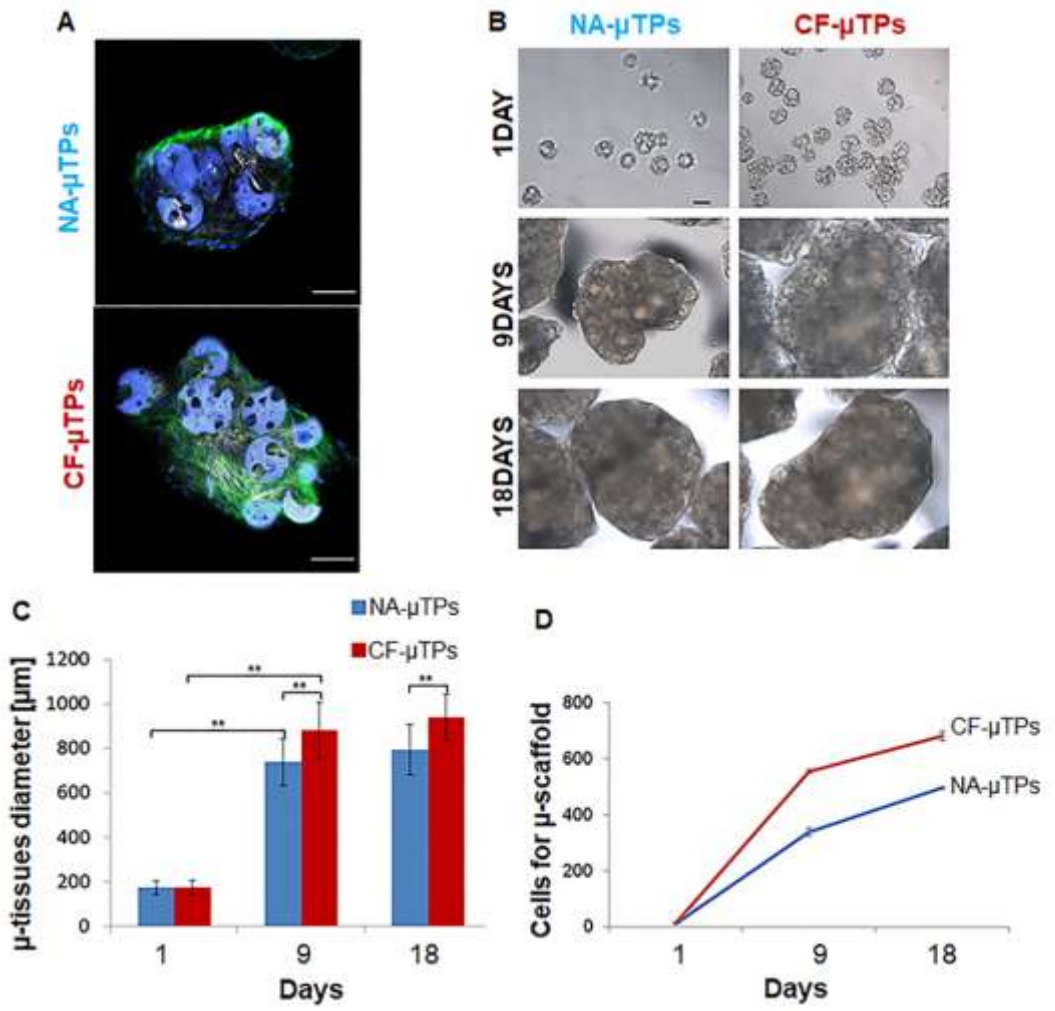

*Figure 2.6 - µTPs morphological characterization: A) Representative images of normal and cystic fibrosis micro-tissues (NA-µTPs and CF- µTPs) showing the nuclei of the cells marked in blue by DAPI, the actin cytoskeleton in green by 488-Phalloidin and the collagen in gray by second harmonic generation signal (SHG), scale bar 100 µm; B) Optical microscope images of NA- µTPs and CF- µTPs 1, 9 and 18 days after seeding of the fibroblasts on the micro-scaffolds, scale bar 100 µm; C) Histogram of NA- µTPs (blue) and CF- µTPs diameter (red) over time (** p value<0.01), data are showed as Mean±Standard Deviation; D) Graphic showing the number of cells per micro-scaffold over time in n NA- µTPs (blue) and CF- µTPs (red).*

Furthermore, both NA- µTPs and CF- µTPs increased their size over time but CF-µTPs were larger than NA- µTPs at each time point (optical image in Figure 2.6B and graphic in 2.6C). The number of cells per µ-scaffold demonstrated that CF lung fibroblasts proliferated faster than the normal ones (Figure 2.6D). Moreover, CF fibroblasts produced a higher amount of collagen as visible in the SHG images (Figure 2.7A) and by the analysis of the collagen fraction (Figure 2.7B). The increased number of cells and the amount of collagen are in agreement with the rise in size of CF- µTPs compared to NA- µTPs. Collagen network morphometry was then investigated by analyzing SHG

images with the correlation feature of the Gray Level Co-occurrence matrix (GLCM) [106–108]. The correlation curve of CF- µTPs decayed slower than the NA- µTPs one (Figure 2.7C) indicating a more disorganized collagen network in the disease model [109]. Moreover, the correlation length of CF- µTPs was significantly higher than NA- µTPs (Table 3), demonstrating the presence of thicker collagen fibers in the disease model [110].

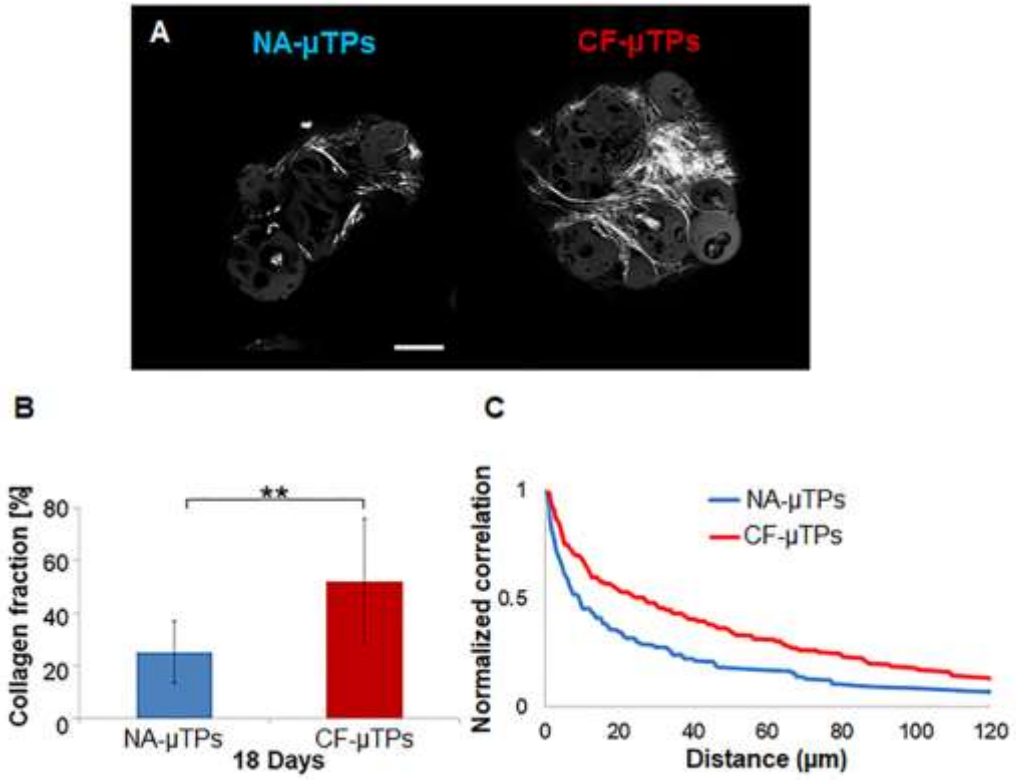

Figure 2.7 - µTPs morphological characterization: A) Second harmonic generation (SHG) images of collagen fibers (shiny gray) in normal and cystic fibrosis micro-tissues (NA- µTPs and CF- µTPs) ; B) Diagram of the collagen fraction (%) in NA- µTPs (bleu) and CF- µTPs (red), data are showed as Mean±Standard Deviation; C) Graphic of the normalized Correlation obtained analyzing SHG images of NA- µTPs (blue) and CF- µTPs (red).

Sample	Correlation length (λ)
NA-µTPs	62.6254±16.23
CF-µTPs	135.88±43.31

Table 3 - Correlation length analysis

2.3.2 CAT production and characterization

Morphological characterization of CAT

In the second step of the process, the "biosintering" of NA- µTPs or CF- µTPs, meaning the biological fusion of the micro-tissue units of the same type [92], was induced to obtain the Normal (NA-CAT) or the CF Connective Airway tissue (CF-CAT) (Figure 2.4)[89]. Specifically, the "biosintering" of CF- µTPs led to the formation of the CF-CAT whose morphological features were compared with the NA-CAT, likewise obtained by assembling NA- µTPs. The macroscopic aspect of the CF-CAT and NA-CAT was very similar, as showed in Figure 2.8A. However, multiphoton microscopy and immunotypization of both models showed that the CF-CAT is characterized by a higher amount of fibrillar collagen, collagen type I, hyaluronic acid and periostin (Figure 2.8B-E). Fibrillar collagen was observed by exploiting SHG imaging. The gray signal in the images in Figure 2.8B highlights the higher quantity of collagen and the more chaotic architecture of the network in the CF-CAT compared to NA-CAT, as already found in micro-tissues. Type I collagen is the main structural protein of the connective tissues responsible for their mechanical properties [111]. Hyaluronic Acid is a large unsulfated glycosaminoglycan, important for tissue repair and homeostasis [112]. Periostin is a matricellular protein with non-structural function, involved in tissue development, repair and remodeling [113]. On the other hand, periostin is involved in different pathological processes such as lung fibrosis [113]. It is able to induce collagen fibrillogenesis and influence tissue mechanical properties [114]. Indeed, our results on mechanical characterization by nano-indentation test (Figure 2.8F) revealed a higher effective elastic modulus in the CF-CAT than NA-CAT, typical of fibrotic tissues [115].

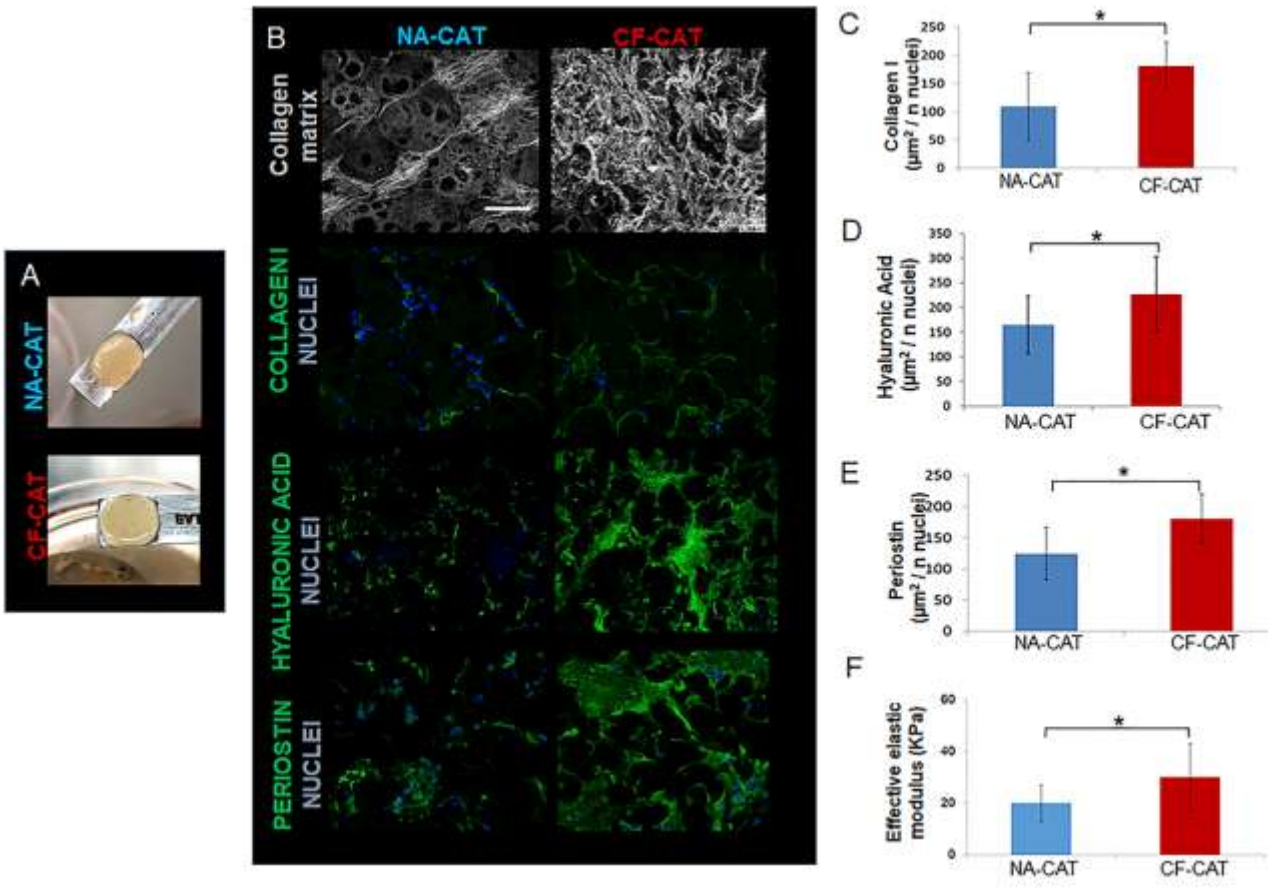

*Figure 2.8 - CAT morphological analysis: A) Macroscopic image of a representative normal and cystic fibrosis connective airway tissue (NA-CAT and CF-CAT); B) Second harmonic generation (SHG) images of collagen fibers in gray and immunofluorescence showing the nuclei of the cells in blue marked by DAPI and in green the signal of Collagen Type I/Hyaluronic Acid and Periostin; scale bar 100µm; C) Diagram of the quantity of collagen (µm^2) type I per cell (nuclei) NA-CAT (blue) and CF-CAT (red); D) Diagram of the quantity of Hyaluronic Acid (µm^2) type I per cell (nuclei) NA-CAT(blue) and CF-CAT (red); E) Diagram of the quantity of Periostin (µm^2) type I per cell (nuclei) NA-CAT(blue) and CF-CAT(red); F) Diagram of the effective elastic modulus of the NA-CAT(blue) and CF-CAT(red). In all the diagrams data are showed as Mean±Standard Deviation *p < 0,05* [89].

Transcriptomic analysis of CAT

To further investigate the effect of the molecular signature underlying the morphological differences observed between CF and Normal fibroblasts (CF-HLF and N-HLF), we performed [89] an unbiased RNA-seq analysis of the cells arranged in 2D or in 3D (CAT) configurations. The transcriptomic analysis confirmed the differences between CF-HLF and N-HLF and highlighted a fundamental role of the 3D environment in replicating tissue physio/pathology *in vitro*. Moreover, as both CF-HLF and N-HLF did not express CFTR, the observed differences between CF-HLF and N-

HLF are not associated with CFTR dysfunction *in vitro* but with other factors probably derived from the patient specific *in vivo* lung condition at the moment of the biopsy from which the primary cells were extracted. Both 2D and 3D conditions were analyzed by comparing the transcriptome of CF-HLF to the transcriptome of N-HLF used as control. In both conditions, we observed a significant alteration of the transcriptome: in details, we found 2005 and 1505 differentially expressed genes (DEGs) in the 2D and in the 3D transcriptomes, respectively. To investigate the effect of the 2D or the 3D condition on the gene expression profiles and to identify the most deregulated pathways, we performed gene ontology enrichment analysis (GOEA) [99] on the two datasets. We observed the term "Extracellular space" (GO:0005615) comprising 81 genes, as the most significant according to GOEA in 3D (Figure 2.9). Similarly, in the 2D dataset the most enriched term was "Extracellular region part" (GO:0044421) (Figure 2.10). Moreover, in agreement with morphological results, CF-HLF over-expressed genes related to the "Extracellular space" (GO:0005615), "Cell proliferation" (GO:0008283) and "Tissue morphogenesis" (GO:00487298) when compared to N-HLF in 3D (Figure 2.9). We observed a set of genes over-expressed by CF-HLF in CF-CAT, which included: hyaluronan synthase 2 (HAS-2), indicating a positive correlation between gene expression and the quantity of hyaluronic acid observed by immunofluorescence; TWIST1 and TGFβ3, positive regulators of periostin synthesis [116,117], and WNT2, SFRP2 and RSPO2 in the WNT pathway. The latter suggests an aberrant activation of the WNT pathway in lung fibroblasts of patients with CF, similar to that observed during lung fibrosis [118,119]. Other genes activated in CF-HLF as in lung fibrosis were: TBX4 [120] and ITGA8 [121]. HHIP and CHI3L1 were both over-expressed in CF, similarly to data reported for chronic obstructive pulmonary disease (COPD) and asthma [122,123] (Table IV).

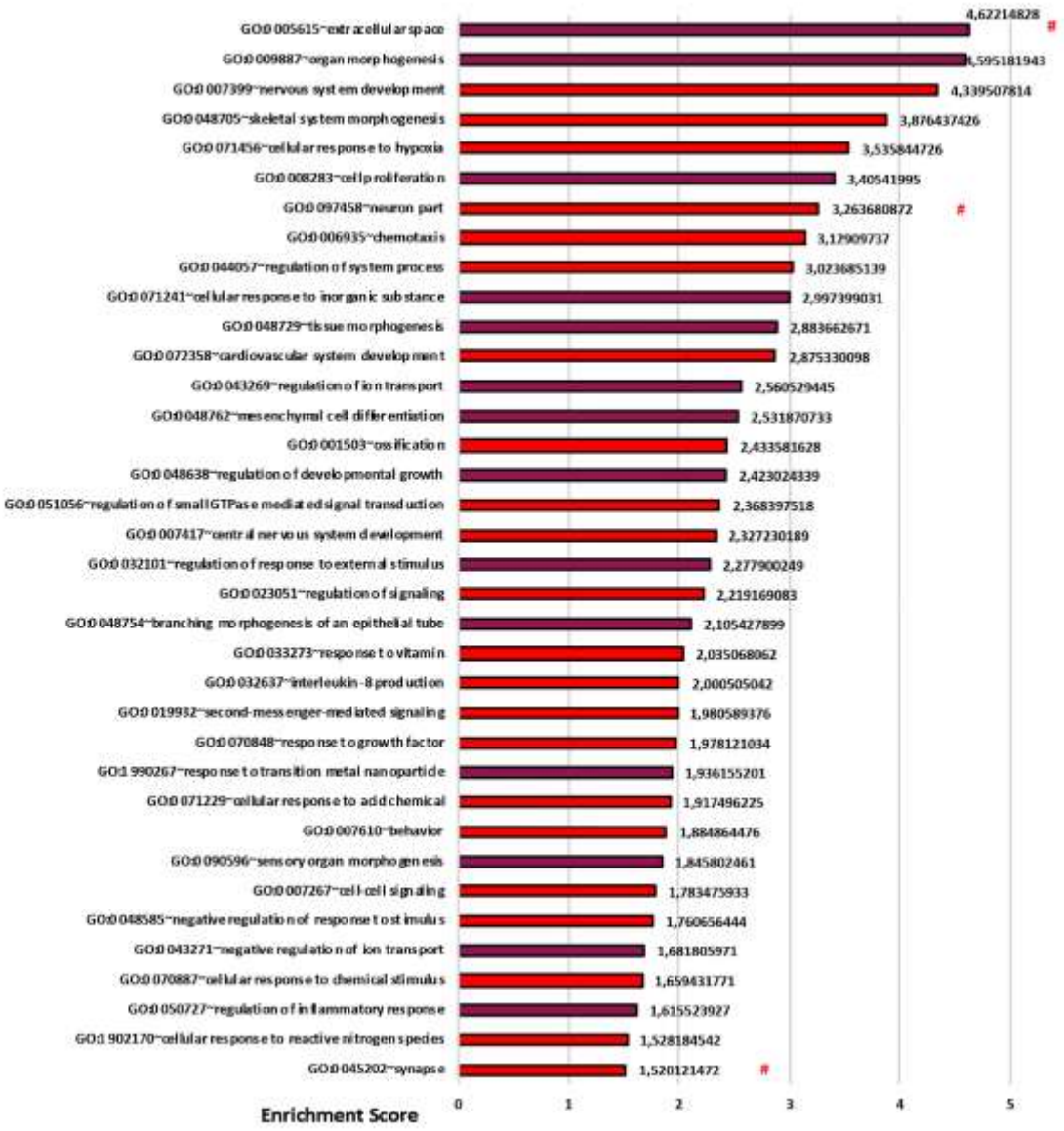

Figure 2.9 - 3D CAT molecular analysis (CF-HLF vs N-HLF): Biological process (BP) and cellular component (CC) significant terms in which the DEG (differentially expressed genes) induced into the 3D dataset are mainly enriched (GSE141536). The threshold of induction plotted is logFC > 2 (487 DEG). # are CC terms. Dark Red terms are the mainly interested induced terms found in our study.

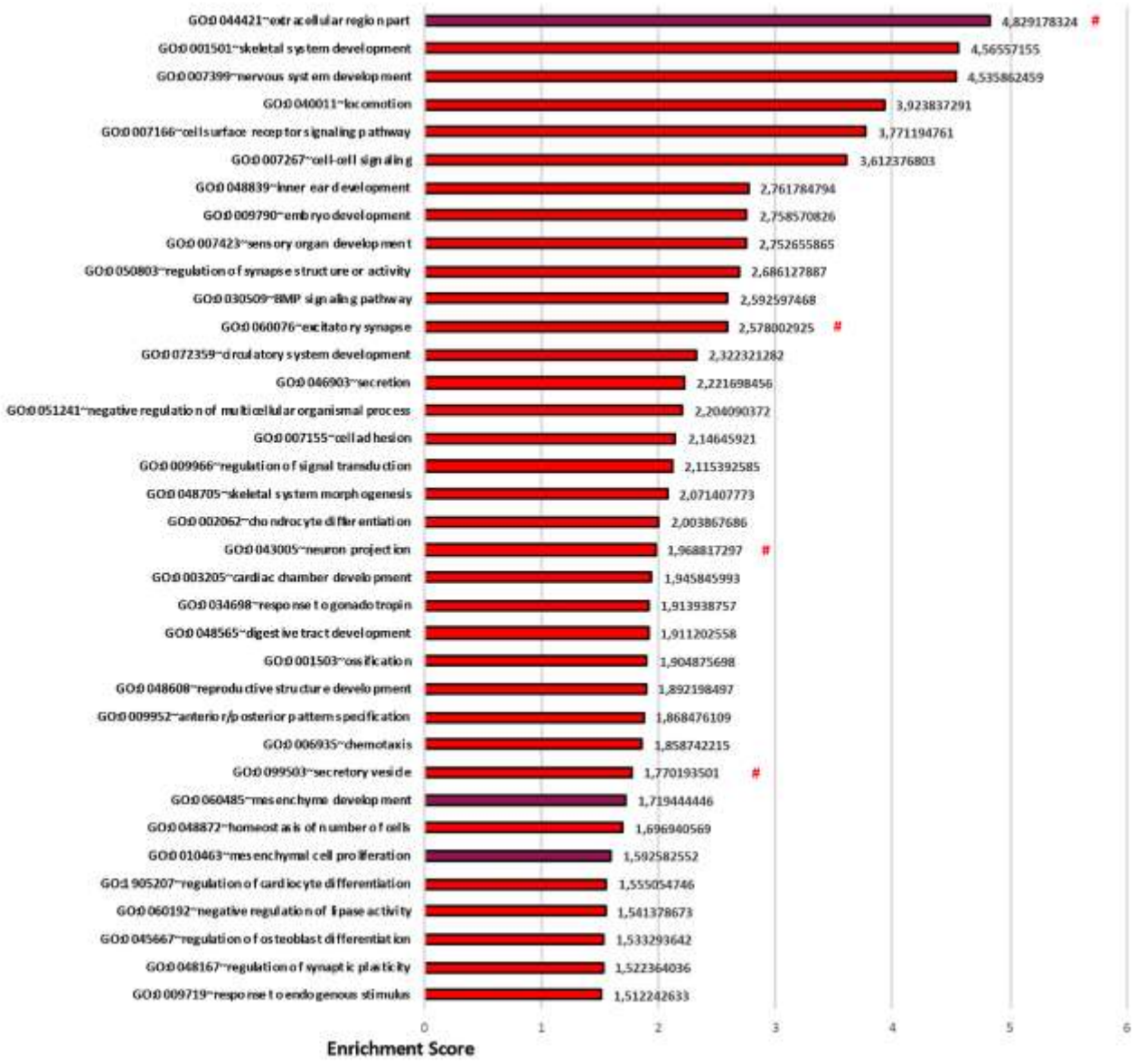

Figure 2.10 - 2D molecular analysis (CF-HLF vs N-HLF): BP and CC significant terms in which the DEG induced into the 2D dataset are mainly enriched. The threshold of induction plotted is logFC > 2 (459 DEG, GSE141535). # are CC terms. Dark Red terms are the mainly interested induced terms found in our study.

Gene symbol	logFC_CF-HLF *vs* N-HLF
TGFβ3	1.755
HAS-2	2.062
TWIST1	2.425
WNT2	3.052
SFRP2	3.695
RSPO2	4.331
TBX4	4.593
ITGA8	4.874
CHI3L1	5.027
HHIP	5.09

Table 4 - Up-regulated genes from the 3D dataset (CF-HLF vs N-HLF)

We then compared the two datasets (2D and 3D) each one normalized on its own control, as represented in the Venn diagram (Figure 2.11)[89]. This analysis allowed us to isolate the genes whose regulation was either dependent or independent of the two different culture conditions and thus to isolate transcripts specifically regulated in 2D (1406 in total, 779 up-regulated and 627 down-regulated), and specifically regulated in 3D (906 in total, 554 up-regulated and 352 down-regulated). Furthermore, we isolated 559 DEGs commonly regulated in both 2D and 3D: 381 up-regulated and 166 down-regulated in both datasets, respectively, whereas 52 were regulated in an opposite manner. Considering the commonly induced 381 DEGs, GOEA highlighted terms such as "Organ morphogenesis" (GO:0009887), "Cell proliferation" (GO:0008283), "Tissue morphogenesis" (GO: 0048729) and "Response to external stimulus" (GO: 0009605) (Figure 2.12). These results strongly suggest that CF-HLF retained an activated state *in vitro* both in 2D and 3D. The 2D specific analysis showed the enrichment of the GO terms "Epithelial cell proliferation" (GO:0050673), "Regulation of epithelial to mesenchymal transition" (GO:0010717), "Canonical Wnt signaling pathway" (GO:0060070) and "Metal ion binding" (GO:0046872). The latter was not enriched in the 3D specific induced dataset (Figure 2.13). Interestingly, in the GOEA performed on the 3D transcriptome highlighted terms such as "Morphogenesis of a branching epithelium" (GO: 0061138), "Inflammatory response" (GO: 0006954) and "Regulation of inflammatory response" (GO: 0050727) (Figure 2.14). These results suggest that only the 3D environment of the CF- CAT

was able to induce the expression of genes involved in these key events occurring during the progression of cystic fibrosis *in vivo* [89].

Figure 2.11 Comparison between the 2D and 3D datasets: Venn diagram of transcriptomic results comparing cystic fibrosis vs normal human lung fibroblasts (CF-HLF vs N-HLF) in 2D and 3D culture conditions.

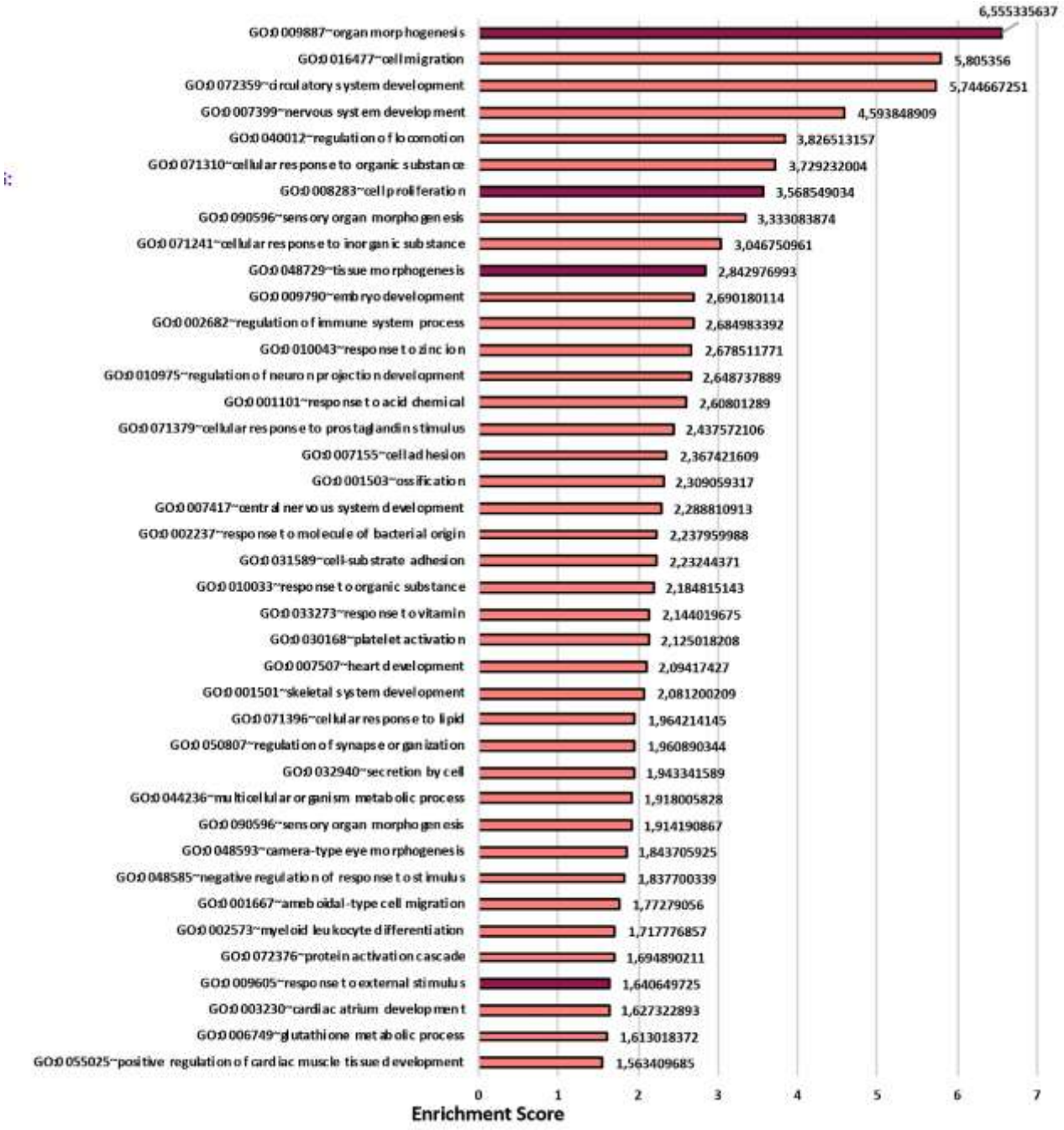

Figure 2.12 2D and 3D molecular analysis (CF-HLF vs N-HLF): All BP significant terms in which the DEG induced both in 2D and 3D datasets are mainly enriched. Dark Red terms are the mainly interested induced terms found in our study.

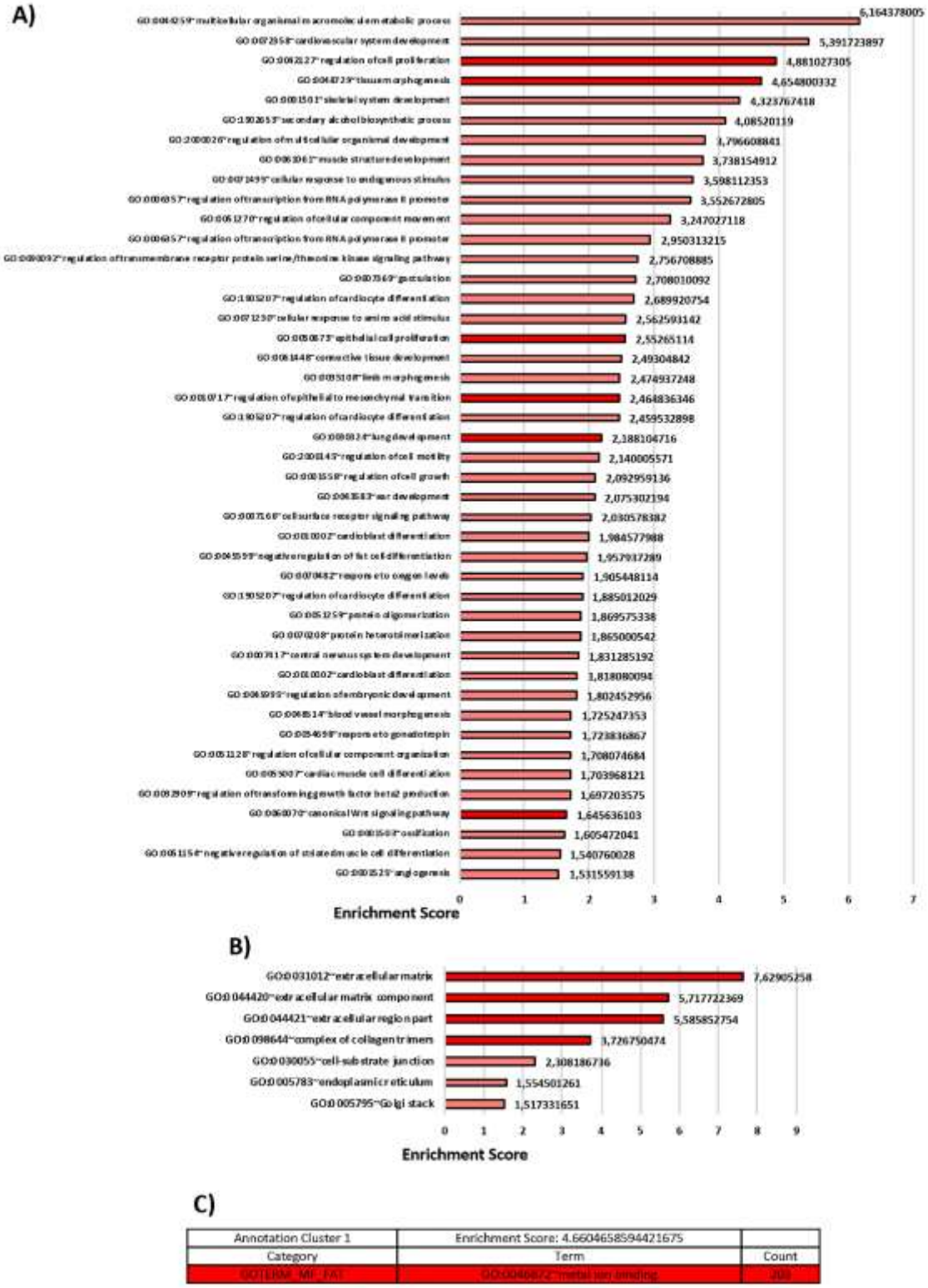

Fig.2.13 - Specific 2D molecular analysis: A) BP and B) CC significant terms in which the DEG specifically induced (779) into the 2D dataset are mainly enriched. Dark Red terms are the mainly interested induced terms found in our study C) The metal ion binding is the top MF in this dataset and is not enriched in the 3D specific induced dataset.

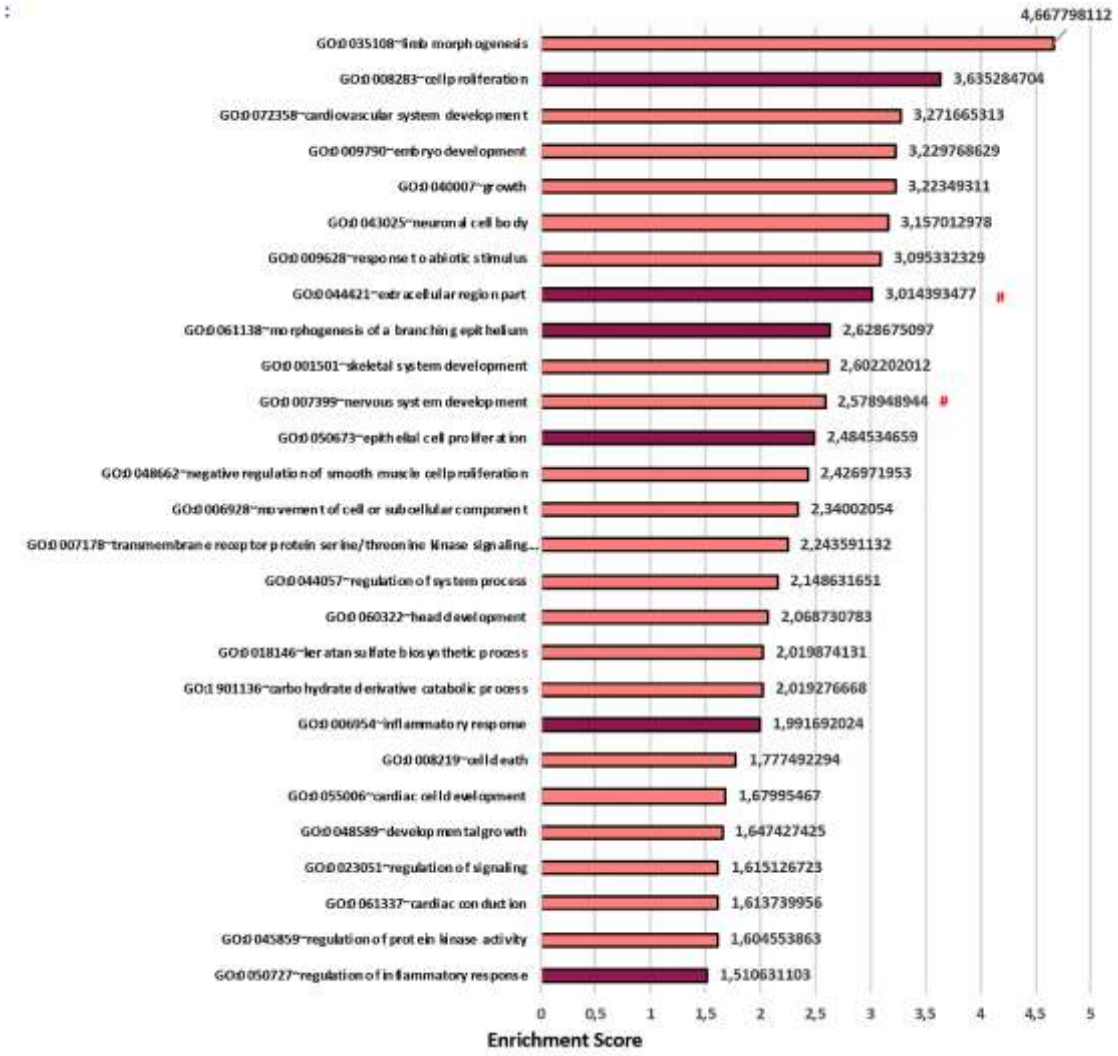

Figure 2.14 Specific 3D CAT molecular analysis (CF-HLF vs N-HLF): Biological process (BP) and cellular component (CC) significant terms in which the DEG (differentially expressed genes) specifically induced (554) into the 3D dataset are mainly enriched. # are CC terms. Dark Red terms are the mainly interested induced terms found in our study.

2.3.3 Full Thickness model production and characterization

Both the epithelium of the Normal and CF Full Thickness model (FT-NA and FT-CF) differentiated *in vitro* under ALI condition. The presence of cilia and mucus was evaluated by observing glutaraldehyde or Perfluorocarbon (PFC: anhydrous fixative) fixed samples at the Scanning Electron Microscope (Fig. 2.15A shows the cilia and the mucus).

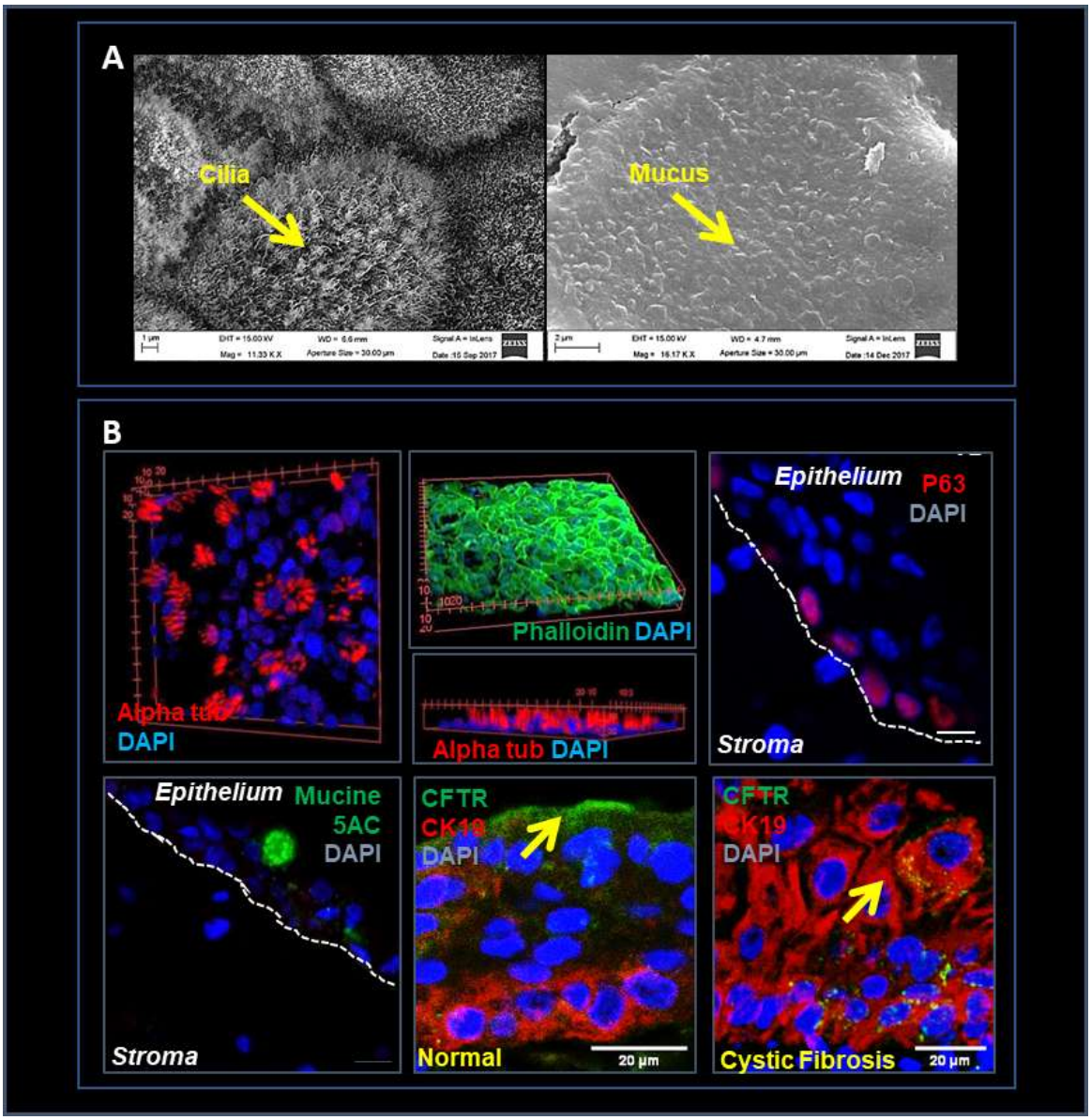

Figure 2.15 - Morphological characterization of the Full Thickness model: A) Muco-ciliary differentiation demonstrated by using the Scanning Electron Microscope (SEM) fixing the sample using glutaraldehyde or Perfluorocarbon (PFC); Confocal images of the alpha Tubulin (red), Phalloidin (green), p63 (red) (scale bar 10µm), Mucin 5AC (green) (scale bar 10µm), Cytokeratin19 (red) and CFTR (green) in the Normal and Cystic Fibrosis Full Thickness model (FT-NA and FT-CF). Nuclei are marked in blue by DAPI.

Moreover, the immunofluorescence in Fig. 2.15B showed that the epithelium was positive for specific markers such as Alpha Tubulin (which marks the cilia), Phalloidin (which marks the actin cytoskeleton), p63 (marker of the stem cells basal layer), Mucin 5AC (which is a mucus protein) and CFTR. Specifically, the chloride channel was localized in the apical part of the FT-NA epithelium and in the cytoplasmic part of the FT-CF epithelium, as expected because we used cells carrying the ΔF508 mutation. Future studies will characterize the presence of the typic epithelial cell populations by single cell RNA sequencing (e.g. secretory, basal, ciliated cells) similarly to bronchial epithelial cells differentiated under ALI on porous inserts (Fig. 2.16) [124].

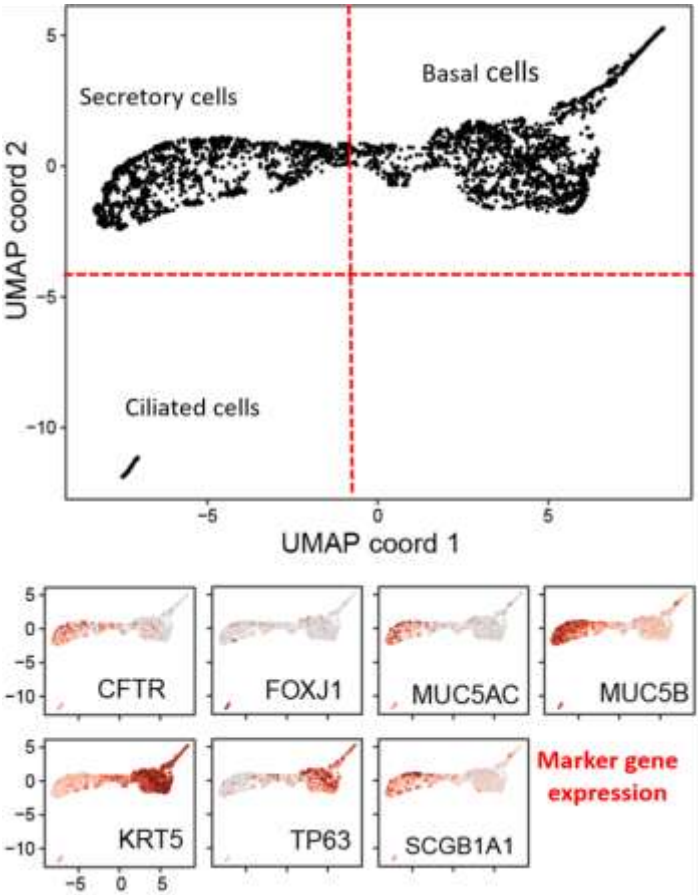

Figure 2.16 - Single cells analysis: Profiling of normal human airways epithelium

Furthermore, epithelial cells are able to penetrate the underlying connective tissue and to form glandular-like structures (Fig. 2.17A/B) consisting of cells positive for Cytokeratin 19 (CK19), p63, CFTR, Mucin 5B and Mucin 5AC (MUC5B, MUC5AC) (Fig. 2.17C/I). The formation of these structures closely reminds the process of morphogenesis of pulmonary glands *in vivo*. For this reason, the FT-CF model could represent a model of gland dysfunction occurring during CF [5]. In this context, future studies will aim to highlight differences between glandular-like structures in the FT-CF and the FT-NA (e.g. gland size, cell number and composition, presence of mucus in glandular ducts, morphological and molecular markers).

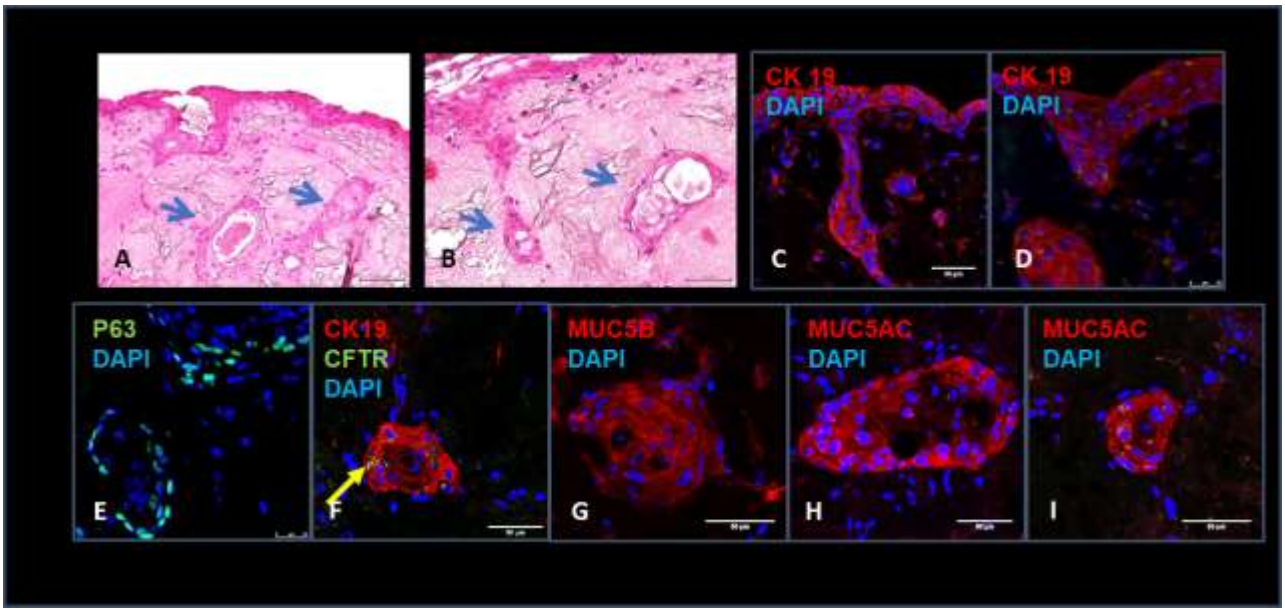

Figure 2.17 Morphological characterization of glandular-like structures in the full thickness model: A/B) Hematoxylin/Eosin showing glandular-like structures, scale bar A 100 µm, B 50µm; C/I) Immunofluorescence for Cytokeratin 19 (CK19 in red), p63 (green), CFTR (green), Mucin 5B e 5AC (MUC5B e MUC5AC in red), scale bar 50µm.

Subsequently, with the aim to functionally characterize the epithelium, we analyzed the viscosity of the apical mucus by Multiple Particle Tracking [125]. This technique is based on the tracking of fluorescent nano-particles (polystyrene, carboxylated, 200nm in diameter) moving into the fluid withdrawn from the apical surface of the sample. Fig. 2.18A shows a representative movement of fluorescent particles in the normal (blue) and CF (red) sample. The trajectory of the particles was very small in the disease model compared to the normal one. As expected, due to the ΔF508

mutation, the analysis revealed that the mucus collected from the FT-CF model was more viscous than the mucus withdrawn from the FT-NA sample (Fig. 2.18B/C).

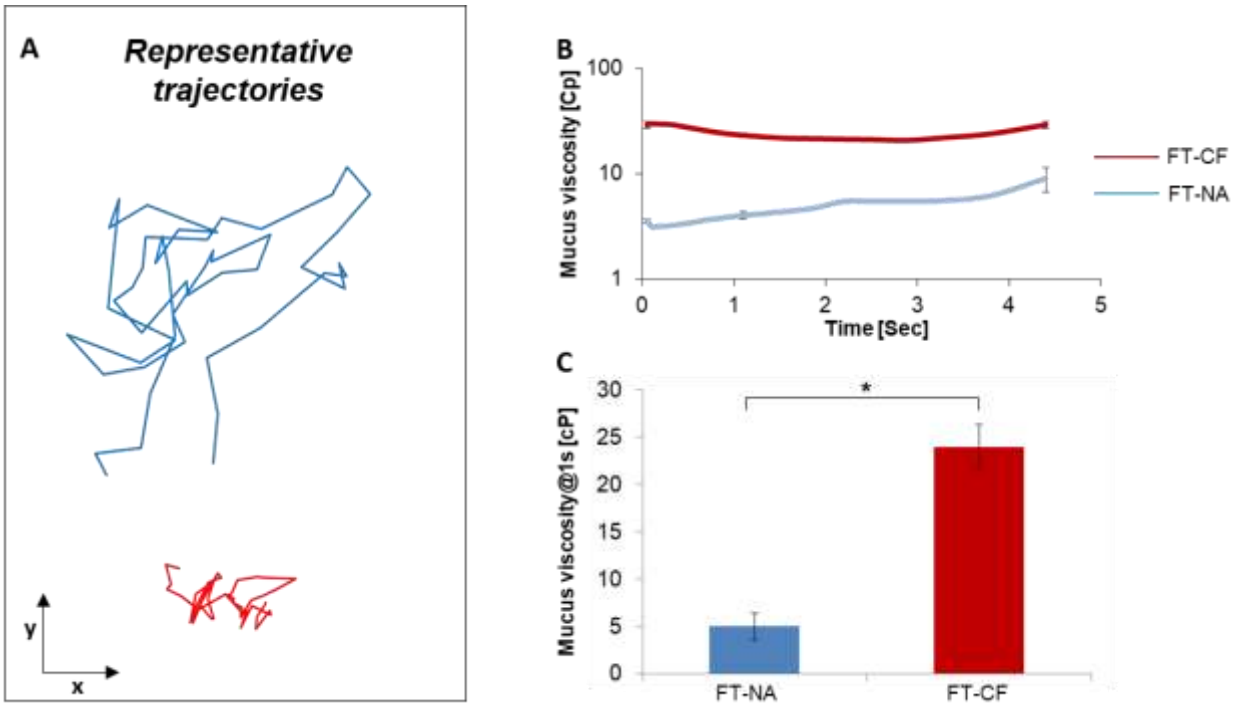

*Figure 2.18 - Analysis of mucus viscosity by Multiple Particle Tracking (MPT): A) Representative trajectories of fluorescent nano-particles moving into the apical fluid withdrawn from the surface of the FT-NA (Normal Full Thickness) (blue) and FT-CF (Full Thickness Cystic Fibrosis) (red) sample; B/C) Graphics of mucus viscosity in the FT-NA and FT-CF. *p<0.05.*

2.4 Discussion

Traditionally, *in vitro* studies of CF lung disease have focused on the analysis of airway epithelial cells carrying CFTR mutations. Consistent with the role of stromal environment in several diseases affecting epithelium [126–128], here we show that the pulmonary CF stroma has non-negligible abnormalities that *in vivo* may have a significant impact on the progression of CF lung disease. Indeed, our results demonstrated morphological and transcriptomic differences existing between primary CF-HLF and N-HLF and the importance of the 3D environment to highlight such features *in vitro*. In this work, we developed a 3D bio-engineered model of CF connective airway tissue (CF-CAT) and compared its characteristics with the normal counterpart (NA-CAT). Specifically, the CF-CAT was achieved *in vitro* by using a bottom up approach (Figure 2.4) and it featured the presence of fibroblasts embedded in their own native ECM. By using the same approach, our group

previously demonstrated the possibility of recapitulating *in vitro* the physio-pathological environment of different tissues in terms of composition and features of the organ-specific ECM, as well as interactions between the epithelial and stromal compartments [37,129,130]. CF arises from CFTR mutation in epithelial cells, but the severe complications of this pathology involve the entire pulmonary tissue and dramatically compromise lung functions. Indeed, mucus plugging, bacterial infection [84], inflammatory response [85,86], and tissue remodeling [87,88] are all central features of CF and represent putative therapeutic targets. In this context, our model uniquely recapitulates lung tissue remodeling and fibrosis occurring during CF. In fact, lung fibroblasts derived from patients with CF displayed an activated and fibrotic phenotype with increased cell proliferation (Figure 2.6D), production of ECM elements (Figure 2.7A/B, Figure 2.8 B/C/D/E), collagen fiber thickness and aberrant organization of the network (Figure 2.7 C, Table III, Figure 2.8B). Among the ECM proteins we found that CF-HLF produced higher amounts of collagen I, hyaluronic acid and periostin. The latter has been recognized as marker of lung fibrosis and inflammation [113]. Moreover, periostin was reported to have a role in collagen synthesis [114], assembly and organization in different pathological conditions [131]. It binds other proteins of the ECM, and the bone morphogenic protein 1 (BMP-1), catalyzing the crosslinking of collagen fibers and increasing tissue stiffness [132]. At the same time, periostin activates HAS-2 function and hyaluronic acid synthesis [133]. The higher quantity of hyaluronic acid and the overexpression of HAS-2 we found in the CF-CAT are as well markers of severe fibrosis [134]. The presence of important abnormalities in CF-HLF, despite the absence of CFTR expression, is probably a consequence of the *in vivo* activation of the cells during the chronic pathology. It appears that CF-HLF *in vitro* retain epigenetic changes resulting from the cascade of events triggered by CFTR loss-of-function and leading to severe inflammation *in vivo*. Here, we did not evaluate the epigenetic profile of the cells, an interesting aspect that should be examined in depth. In this work, we focused on the transcriptomic profile of CF-HLF. Our results demonstrate that CF-HLF display the up-regulation of genes involved in the production of elements of the extracellular space compartment as well as in the control of tissue/organ morphogenesis and cell proliferation (Figure 2.11). At the same time, the CF-HLF phenotype overexpressed genes of the WNT pathway, TBX4 and ITGA8, which are involved in lung fibrosis [118–121]. Moreover, although we confirmed that lung fibroblasts do not express CFTR, CF-HLF showed the up-regulation of the GO terms “Regulation of ion transport” (GO:0043269) and “Negative regulation of ion transport” (GO:0043271). We hypothesize that such overexpression could be a consequence of the *in vivo* CFTR dysfunction in epithelial cells. On the

other hand, the transcriptomic analysis showed that CF-HLF genes involved in the biological processes of “Mesenchymal cell differentiation” (GO:0048762) (Figure 2.11), “Mesenchyme development” (GO:0060485) and “Mesenchymal cell proliferation” (GO:0010463) (Figure 2.10) were upregulated, suggesting that CF-HLF have the potential to activate the Epithelial to Mesenchymal Transition (EMT). This phenomenon has been well characterized in other lung diseases and it has been recently associated to CF [135]. Interestingly, EMT has been always recognized as a driven mechanism of lung fibrosis [135,136], however, here we show that the activation of lung fibroblasts during fibrosis can, in turn, stimulate EMT. Furthermore, we denoted that the GO term “Morphogenesis of a branching epithelium” (GO:0061138) was enriched only in the 3D culture condition and not in the 2D (Figure 2.14). It was previously demonstrated that the presence of the stromal compartment is necessary for epithelial branching during the *in vivo* development of the lung [137]. Likewise, here we observed that the connective tissue has a central role in the morphogenesis of epithelial structures in a 3D *in vitro* environment. Moreover, our data show that the formation of branching epithelial structures can be altered in CF due to enhanced fibroblast stimulation. We assume that such biological process can be involved in the dysregulation of submucosal gland morphology and function observed in CF. Indeed, these structures develop through a process of branching morphogenesis *in vivo* [5] and are hyperplastic and mucus occluded in the disease state [138,139]. Furthermore, submucosal glands alteration has been recognized as an important factor contributing to CF pathophysiology [140]. On the other hand, the upregulation of the GO term “Morphogenesis of a branching epithelium” in the 3D CF model underline that in such a physiological relevant *in vitro* environment, fibroblasts, even if cultured without epithelial cells, can to ‘store memory’ of the epithelial stromal crosstalk occurring *in vivo*. At the same time, CF-HLF overexpressed genes involved in the “Inflammatory response” (GO:0006954) also without being exposed to inflammatory stimuli *in vitro* (Figure 2.14). Indeed, inflammation is a hallmark of CF, characterized by structural lung tissue changes and promoted by persistent bacterial colonization of the airways [85,86]. Our results demonstrate that lung fibroblasts contribute to the amplified inflammatory response observed in patients with CF [141]. In conclusion, our transcriptomic analysis highlights the importance of the 3D microenvironment in the expression of genes involved in the crosstalk between the stroma and the epithelium, inflammation and fibrosis. In CF, stromal/epithelial crosstalk has consequences on both tissue morphogenesis and function/dysfunction, whereas inflammation and fibrosis are responsible for the occurrence of severe complications in patients with CF. Our work sheds light on the alterations

of the connective airway tissue in CF, which cannot be neglected for the study of this pathology and for the development of therapeutic strategies. Most probably, the connective tissue changes derive from the epithelial damage and in turn impair epithelial function [89].

Furthermore, in the Full thickness model, the interaction between epithelium and connective tissue was demonstrated by the presence of epithelial structures within the stroma, so-called *glandular-like structures*, whose morphogenesis resembles the morphogenesis of pulmonary glands, which dysfunctional in CF.

In the full-thickness model, epithelial cells formed a differentiated epithelium on the connective surface. There were not morphological differences between the normal and diseased epithelia except for the localization of CFTR (apical in the normal and cytoplasmic in the CF model). Instead, the viscosity of the apical mucus was higher in the CF than the normal model.

2.5 Conclusions

In conclusion, the transcriptomic analysis highlighted the importance of the 3D microenvironment in the expression of genes involved in the crosstalk between the stroma and the epithelium, inflammation and fibrosis. All these processes are involved in the evolution of CF. In fact, stromal/epithelial crosstalk has consequences on both tissue morphogenesis and function/dysfunction, and inflammatory response and fibrosis are responsible for the occurrence of severe complications in patients with CF. Our work sheds light on the alterations of the connective airway tissue in CF, which cannot be neglected for the study of this pathology and for the development of therapeutic strategies. Most probably, the connective tissue changes derive from the epithelial damage and in turn impair epithelial function [89].

Furthermore, results demonstrated the effective differentiation of the bronchial epithelium on the CAT and the development of the Full thickness model. This latter was uniquely characterized by the presence of typical airway epithelial structures into the underlying stroma, thus offering novel model useful for the understanding of epithelial-stromal crosstalk in cystic fibrosis and opening to new putative therapeutic strategies.

Chapter 3

Lung on a chip

3.1 Introduction: From traditional cystic fibrosis model to Lung on a chip.

As mentioned in the previous chapters, CF is caused by mutations in the CFTR gene. In the airways, CFTR dysfunction impairs mucociliary clearance, promoting bacterial colonisation and chronic neutrophilic inflammation. CF pathobiology can be studied by :

- evaluating the functional status of the various organs;
- examining substances present in the blood and other biological liquids that document the conditions of deviation from normal metabolism;
- studying patient cells easy to obtain, i.e blood cells, nasal epithelial cells, intestinal epithelial stem cells);
- using tissues and organs collected for therapeutic purposes (for example, the explanted lungs of subjects undergoing lung transplantation).

However, these approaches suffer of several limitations. *Animal models* of CF have been recently introduced (Fig. 3.1). The pig model is the one more closely related to the human pathology, but its use is limited by the high cost and the difficulty to handle such large animals. The murine model is widley used. CFTR-KO and ΔF508-CFTR models are available, al

Disease	Human	Pig	Ferret	Rabbit	Rat	Mouse
Spontaneous Lung Infections	✔	✔[9]	✔[8,10]	?	X	X[2,15,39]
Impaired Growth	✔	✔[7]	✔[8,10]	✔[4]	✔[3]	✔[2,15,39]
Intestinal	✔	✔[7,35]	✔[8,11,35]	✔[4]	✔[3,35]	✔[2,15,39]
Exocrine Pancreatic	✔	✔[29-30,35]	✔[11,35]	?	X	X[2,15,39]
Endocrine Pancreas	✔	✔[32]	✔[31]	?	?	X[2,15,39]
Hepatic	✔	✔[35,40]	✔[11,35]	?	?	X[2,15,39]
Gallbladder	✔	✔[35,40]	✔[11,35]	?	NA	X[2,15,39]

***Fig. 3.1** - Organ disease presence or absence in various genetically modified animal models. Organs affected in humans with CF are listed on the left. Check marks below each CF model species indicates disease presence, while question marks denote disease has yet to be evaluated. Organs marked by an X indicate lack of overt disease. NA, not applicable as rats do not have a gallbladder*[142].

However, murine CF displays anatomic and immunologic differences with the human disease[143]. CF mice are not long-lived and it is not known whether for this reason or for other reasons still unknown, they develop intestinal CF disease, but little or no lung disease.

Although the use of animal models is an essential step for the clinical experimentation of the pathology, other types of models have been developed in order not only to limit animal experimentation for ethical reasons, but above all to replicate the evolution of the cystic fibrosis pathology to lung level (not only intestinal). Indeed progressive lung disease and respiratory failure are the main cause of morbidity and mortality for most cystic fibrosis patients [83].

A cornerstone for CF research is represented by the 2D *Human Airway Epithelial (HAE) Cell Culture*. Primary Human Bronchial epithelial cells (HBE) are now largely used for studies on CF disease [144,145]. HBE cells can be isolated from lung explants or cadavers. Explanted lungs and post-mortem samples from individuals with CF provide high cell yield. However, the extensive tissue damage, particularly of the epithelial cell layer, plus the presence of chronic microbial colonization represent technical challenges to establishing successful *ex vivo* cultures. Therefore, supply of CF patient-derived HBE cells are often limited and difficult to obtain.

Human nasal epithelial (HNE) cells are increasingly used as surrogates for the lower airway epithelium in CF research[146,147]. HNE cells share many characteristics of HBE cells, including the ability to form polarized, pseudostratified epithelium that mimick *in vivo* airways, and the expression of ion channels such as CFTR. They have the advantage of being collected by non-invasive procedures. HNE cells are grown using the same culture media and protocol as for HBE cells.

Patient-derived intestinal epithelial stem cells, differentiate into organoids also represent an invaluable resource for studies on the relationship between the CFTR gene mutation and the disease phenotype. Intestinal organoids are now used for high-throughput screening (HTS) for drug discovery in CF [148]. They are also used for personalized approaches to treatments with the newly introduced CFTR modulators

Organoids are 3D in vitro cell cultures that derive from stem cells that spontaneously self-organize in space in a way quite similar to the reference organs in vivo.

In CF, *intestinal organoids* (or mini-guts) can be grown from crypts isolated from fresh rectal biopsies[148]. Crypts are rich in stem cells which grow and differentiate into self-organizing, multicellular structures[149 150]. These organoids contain all the intestinal cell types present in the *in vivo* epithelium[151]. The growth and differentiation of stem cells into closed epithelial structures with an internal lumen require a fine balance of growth factors, inhibitors of TGF-β and BMP signaling and the basement membrane matrix (matrigel). Intestinal organoids can be indefinitely cultured and remain genetically and phenotypically stable upon repeated passaging and long term culture[152]. Capitalizing on the high expression of CFTR in rectal tissues and the rapid expansion of stem cells, intestinal organoids represent an attractive model for the the assessment of CFTR functional responses in pharmacological testing. They provide the added advantage to test combination of CFTR modulators without established safety profiles as part of the pre-clinical evaluation in CF patients with rare CFTR genotype. However, these innovative 3D models have a number of disadvantages:

1) absence of endogenous matrix, being immersed in matrigel;

2) difficulty in maintaining the stem cell niche that exists in vivo between the crypt and intestinal villous;

3) relative invasive procedure for collection;

4) difficulty in electrical measurements, being in a close conformation;

5) not necessarily representative of the airways.

As demonstrated in the second chapter and in our work published in Cells 2020 [89], the *full tickness airway* (Normal and Cystic Fibrosis models), engineered in our laboratories, provides an important turning point for cystic fibrosis because it reproduces the bronchial tissue in vitro and thus offers clinical research a new 3D model to deepen the study of the mechanisms of action and dysfunction of the CFTR protein, not only at the epithelial level, but above all at the stromal level with the endogenous extracellular matrix presence.

Furthermore, new organ-on-chip (OOC) platforms have been developed with the aim to reproduce in vitro activities, mechanics and physiological response of entire organs or organ systems, and

therefore represent the dynamic and complex in vivo condition[153]. The convergence of labs-on-chips (LOC) and cell biology allows the study of human physiology in a specific context for the organ, introducing the new model of multicellular human organisms in vitro. The application of microfluidics to organ-on-chips also allows efficient transport and distribution of nutrients and other soluble signals through the vital constructs of 3D tissue. On-chip organs are regarded as the next wave of 3D cell culture models that mimic the biological activities of entire living organisms, dynamic mechanical properties and biochemical functions[153].

In this context, we aimed to reproduce the tissue mechanics and the vital microenvironment in of the bronchus, through the use of microfluidics. In this second part of the thesis, I will therefore propose a totally innovative three-dimensional platform, the so-called "Lung on a chip". It is a microfluidic chip never made before in which the human physio/pathological airways can be reproduced in dynamic condition, mimicking the in vivo environment and studied in greater depth. Therefore, this chapter will illustrate the manufacturing and optimization technique of the new microfluidic device constructed for tissue culture and live monitoring of tissue functions.

Furthermore, the optimization of the paramenters for dynamic culture and treatment on chip will be illustrated by exploiting the differentiated human bronchial epithelial model, healthy and affected by fibrosis. Next studies will be focused on the full thickness model on chip with the aim to offer a unique functional model, useful for the understanding of epithelial-stromal crosstalk occurring in CF and for the validation of novel therapeutic strategies targeting not only the epithelium but also the connective compartment, via aereosol or systemic administration.

3.2 Matherial and methods

3.2.1 Design and fabrication of a microfluidic device

In order to optimize the microfluidic conditions, we have fabricated and tested different kinds of devices. Regardless of the geometry, size and type of material used, all the chips we have made are characterized by two polymeric layers, upper and lower part. The upper part consists of a central chamber of 12 or 6 mm in which there is a snapwell for sample housing and an inlet and an outlet for the culture medium flow. The lower part is made by digging a channel, 1.5 mm deep, to ensure the flow of the culture medium basolaterally to the sample.

Almost all microfluidic devices used in this work were fabricated by a *rapid prototyping procedure*. The upper and lower layers of the microfluidic device were prepared by demolding polydimethylsiloxane (PDMS) (Sylgard 184, Mascherpa), from a Poly (methyl methacrylate) (PMMA, Goodfellow) slab. The PMMA masters (top and bottom part of mirofluidic chip) mold were designed by the AutoCAD program generating a CAD file, which was subsequently converted into a CAM format using the Deskam program. This particular format was sent to the Milling machine (Minithech CNC Mini-Mill described in the prevoius *1.10.1 paragraph*) making a relief positive geometry to avoid silanization process of PDMS. The ratio between PDMS prepolymer and curing agent was 10:1 (w/w), then the mixture was degassed in centrifuge for 5 minutes at 1500 rpm to remove air bubbles and then poured on PMMA masters. The set-up was incubated at 80°C for 60 minutes, then peeled off from master molds. Inlet and outlet holes of the upper layer were punched with a 2.5 mm biopsy punch (DifaCooper) or created by cutting the chip at both ends of the channel, while lung chambers were punched using a 6.5 mm or 12 mm puncher (Am-Tech). The two PDMS layers were overlapped in order to match the upper and lower tissue and irreversibly assembled using a small amount of PDMS. This setup was incubated at 80° for 60 minutes. Finally, abudant PDMS was used to seal two inlet and outlet pipes and to attach the final chip to a glass microscope slide (24 mm wide × 60 mm 38 long) for mechanical support. The whole setup (pipes, chip, glass slide) was incubated at 60 °C overnight to achieve irreversible bonding of the entire device.

On the other hand, for the first microfluidic chip model, we tested another building strategy, simply by assembling the two PMMA plates, top and bottom part, using Isopropyl alcohol (IPA) in a heater at 80° C for 15 minutes; so the two PMMA plates were irreversibly closed and used in direct contact with the cells after adequate sterilization with 70% ethanol and UV rays, without replication molding or the use of other polymers.

As mentioned above, in general the device was equipped with 2 channels adjacent to the central chamber for the baso-lateral flow of the culture medium under dynamic condition. In fact, the device can be connected to a peristaltic pump through a system of connectors, tubes and reservoir, in order to obtain the passage of the fluid inside the channels and to establish the closed-cycle dynamic culture regime (Fig. 3.2). In this way, it could be possible to deliver drugs to the sample, mimicking the systemic administration.

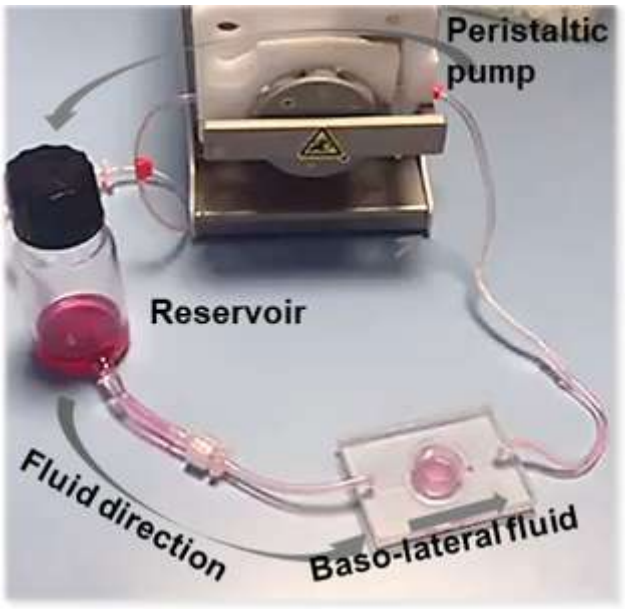

Fig. 3.2 – A system of dynamic cell culture condition for a generic chip

3.2.2 Mathematical model CFD simulation

In order to define the experimental dynamic setup, the three-dimensional velocity and the oxygen gradients in the microbioreactor before in vitro trial, we used the commercial CFD COMSOL Multiphysics vers 5. CDF analyses were performed dividing the entire bioreactor into two different domains as shown in Fig. 3.3: a fluid domain indicated with f, which identifies the region filled with culture medium, and a tissue domain, indicated with t, which identifies the region filled with the the human bronchial equivalent (HBE) samples. The properties of the material were manually added on the basis of empirical results and of values taken from the literature (Figure 3.4).

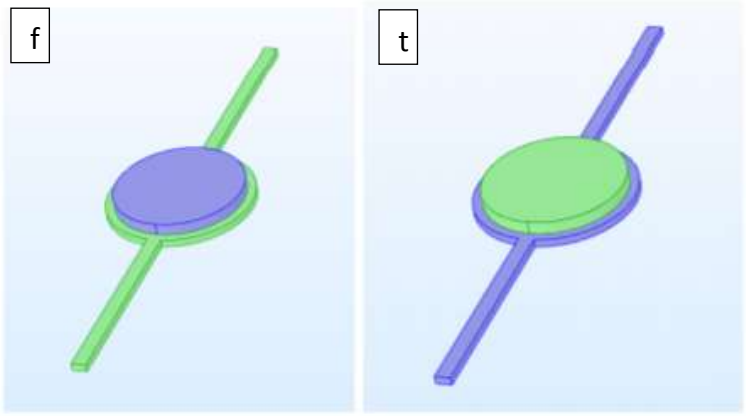

Fig. 3.3 - CFD Images of medium's domain (domain "f" of the fluid) and tissue's domain (domain "t"), both highlighted in green.

Property	Variable	Expression	Unit	Size
Density	rho	999.7	kg/m³	1x1
Dynamic viscosity	mu	0.001	Pa·s	1x1
Porosity	epsilon	0.7	1	1x1
Permeability	kappa_iso...	1e-11	m²	3x3

Fig. 3.4 – Tissue properties

To simulate culture conditions, and in particular the distribution of oxygen throughout the tissue, the velocity field and the fluid shear stress, COMSOL Multiphysics was used, coupling the *Free and Porous Media Flow* and *Transport of Diluted Species in Porous Media* modules in steady state conditions. The first physics implements Navier-Stokes equation for the free fluid phase and Brinkman extended Darcy's equation for the porous matrix, while the second physics implements the mass balance equation:

- Navier-Stokes equation

$$\begin{cases} \rho \boldsymbol{u} \cdot \nabla \boldsymbol{u} = \nabla \cdot [-pI + \mu(\nabla \boldsymbol{u} + (\nabla \boldsymbol{u})^T)] + \boldsymbol{F} \\ \rho \nabla \cdot \boldsymbol{u} = 0 \end{cases}$$

- Brinkman equation

$$\begin{cases} \frac{\rho}{\epsilon_p} \boldsymbol{u} \cdot \nabla \frac{\boldsymbol{u}}{\varepsilon_p} = \nabla \cdot \left[-pI + \frac{\mu}{\varepsilon_p}(\nabla \boldsymbol{u} + (\nabla \boldsymbol{u})^T) - \frac{2}{3}\frac{\mu}{\epsilon_p}(\nabla \cdot \boldsymbol{u})I \right] - \left(\mu \kappa^{-1} + \beta_F |\boldsymbol{u}| + \frac{Q_{br}}{\varepsilon_p^2} \right) \boldsymbol{u} + \boldsymbol{F} \\ \rho \nabla \cdot \boldsymbol{u} = Q_{br} \end{cases}$$

- Mass balance

$$\begin{cases} \nabla \cdot \boldsymbol{\Gamma_i} + \boldsymbol{u} \cdot \nabla c_i = R_i + S_i \\ \boldsymbol{N_i} = \boldsymbol{\Gamma_i} + \boldsymbol{u} c_i = -\mathcal{D}_{e,i} \nabla c_i + \boldsymbol{u} c_i \end{cases}$$

Concerning the boundary conditions, at the chip outlet atmospheric pressure was considered (p = 1 atm), no slip condition was adopted at the walls, equality for velocity and pressure was imposed at the Navier-Stokes (u, v, w, p)/ Brinkman (u_2, v_2, w_2, p_2) interfaces. Imposing for O_2 concentration in the culture medium (0.22 mol/m^3), the diffusion coefficient (D) (10^{-9} m^2/s), cell density (ρ)

($0.2 \cdot 10^{14}$ cell/m^3), maximum velocity of O_2 diffusion (V_{max}) (10^{-18} mol/(cells·s)) and O_2 concentration at $V_{max}/2$ (K_m) (10^3 mol/m^3), the convection-diffusion equation was implemented in the model in order to evaluate the O_2 consumption in the bio-system. All these values were previously evaluated experimentally. The liquid we modelled is incompressible and the governing equation in the fluid region is given by incompressible Navier-Stokes Equation:

$$\frac{\partial u}{\partial t} + u \cdot \nabla u = \frac{1}{\rho}(\mu \Delta u - \nabla p + f_{NS})$$
$$\nabla \cdot u = 0$$

where $u = (u,v)^T$ is the velocity vector, p is the hydrodynamic pressure, ρ is the density, f_{NS} is the external body force and μ is the dynamic viscosity coefficient. With flow in porous media, we mean a material consisting of a solid matrix with an interconnected void, the interconnectedness of the void (the pores) allows the flow of one or more fluids through the material. The details of the internal geometry of porous media are essentially random and unknown. The saturated flow in porous media is described by Darcy's model and expressed by the equations:

$$\mu K^{-1} u = f_D - \nabla p$$

The permeability tensor, a characteristic of the porous media geometry, is denoted by K. The above relation does not take into account the viscous resistance and convective acceleration terms. This, in effect, imposes serious limitations on the range of validity of Darcy's law, which was valid for flows with low Reynolds number. As the flow velocity or particle size increases, Darcy's linear relationship between the discharge velocity and pressure gradient breaks down. Consequently, in order to describe the high porosity and high velocity, the following Brinkman model, which is an extension of Darcy's model was considered. Brinkman accounted for the presence of a solid boundary by adding a viscous term to Darcy's law. The unsteady Brinkman equation for viscous flows in a porous media is given by:

$$s\frac{\partial u}{\partial t} + u \cdot \nabla u = \frac{1}{\rho}\left(\nabla \cdot \left(\mu_{eff}\nabla u\right) - \mu K^{-1}u - \nabla p + f_B\right)$$

where $\mu_{eff} = \mu/\varepsilon_p$ is the effective viscosity, $s = 1 + (1 - \varepsilon p)\cdot c_m/\varepsilon_p$ is the inertial coefficient, c_m is a coefficient of added mass and ε_p is the porosity of the porous structure. The left-hand-side terms in equation above denote the inertial force per unit volume, the right-hand-side terms represent the total forces acting on the fluid per unit volume. The first term on the right- hand-side is the force caused by the pressure gradient, the second term represents the viscous force and can be traced back to Brinkman who suggests that for flow motion in porous media with high permeability, the viscous shear stresses acting on the pore flow should be added to the momentum equation. The viscous stress term is responsible for transferring shear force and may become increasingly important near the interface between the porous and pure liquid regions. The convective term should improve the non-linear effect for the wave structure interaction, while the benefit of including the viscous force term for pore flow is the complete forces acting on the flow are taking into account. The third term represents the resistance force acting on flow by fixed solid skeleton.

Consequently, the equations are of the same type as the Navier-Stokes equations for the flow in the pure liquid region. Hence, both equations can be solved using the same numerical algorithm and formulated as single system called Navier-Stokes-Brinkman system[154]. Laminar flow with different flow rates was set at the inlet and zero pressure was set at the outlet. Different flow rates were investigated in order to evaluate the best culture conditions which gave the velocity able to ensure cell viability and oxygen consumption. The first attempt was performed by starting with a velocity taken from preliminary experiments achieved by our research group, [130], which ranges from 0.04-0.06 m/s. Adapting to our geometry, this velocity was achieved by applying a flow rate of 4 ml/min. Moving on this scenario, we performed different simulations at different order of magnitude, choosing a lower, an intermediate and a higher flow rate, respectively, 40 µl/min, 1 ml/min and 4 ml/min. The oxygen concentration within the system was calculated by means of the following mass balance equation:

$$D\nabla^2 c - \nabla(cv) = R$$

where c is the oxygen concentration, v is the fluid velocity field, D is the diffusion coefficient of the oxygen, R is the volumetric oxygen consumption rate expressed by the Michaelis–Menten law and according to the next equation:

$$R = \frac{\rho V_{max} c}{K_m + c}$$

where V_{max} is the maximum oxygen consumption rate and K_m is the concentration at which the oxygen consumption rate is half of V_{max}, ρ is the cell density in the cultivation chamber obtained by taking into account the number of cells present in the HBE tissue housed into the transwell fixed on the microdevice. R was set to 0 only in the fluid domain, since cells are present only in the tissue domain. The air-liquid interface was mimicked by an open wall at the bottom of the central chamber.

Finally, another important parameter which contributed in the choice of the proper flow rate was the shear stress. In the simulation, the study of the shear stress was integrated on the base of the velocity results coming from the steady-state study, i.e. the velocities that the adopted fluid-related physics (*free and porous media flow – abbr. fp*) provided. Our fluid corresponds to the culture medium that can be easily approximated to water. For all Newtonian fluids in laminar flow, the shear stress is proportional to the strain rate in the fluid, where the viscosity is the constant of proportionality. For non-Newtonian fluids, the viscosity is not constant. The shear stress is imparted onto the boundary as a result of this loss of velocity.

For a Newtonian fluid, the shear stress at a surface element parallel to a flat plate at the point is given by:

$$\tau(y) = \mu \frac{\partial u}{\partial y}$$

where

μ is the dynamic viscosity of the flow;

u is the flow velocity along the boundary;

y is the height above the boundary.

The Newton's constitutive law, for any general geometry (including the flat plate above mentioned), states that shear tensor (a second-order tensor) is proportional to the flow velocity gradient (the velocity is a vector, so its gradient is a second-order tensor):

$$\tau(u) = \mu \nabla u$$

and the constant of proportionality is named dynamic viscosity. For an isotropic Newtonian flow, it is a scalar, while for anisotropic Newtonian flows it can be a second-order tensor too. The fundamental aspect is that for a Newtonian fluid the dynamic viscosity is independent on flow velocity (i.e., the shear stress constitutive law is linear)[155].

Characterizing this parameter is as fundamental as simulating optimal velocity since shear stress may stimulate both the differentiation of the tissue and damage the tissue itself. Thus, the choice fell on those volumetric flow rates that guaranteed shear stress close to the physiological ones (0,5-3 dynes/cm^2)[156] or, at least, similar to the values adopted in the reference literature (1 dyn/cm^2)[157].

3.2.3 Cell culture in dynamic conditions

Normal/Cystic Fibrosis Human bronchial epithelial cells (respectively, NA-HBEC/CF-HBECs ΔF508) were provided by the Primary Cell Culture Facility of the FFC (Istituto G. Gaslini, Genova). Cells were seeded in flasks pre-coated with Rat tail collagen and expanded using the LHC9/RPMI164, a serum-free culture medium that allows to expand the initial number of cells keeping them in an undifferentiated state. In this phase, the cell density was checked carefully.

The cells were rapidly thawed at 37 °C and resuspended in 10 ml of serum-free medium, centrifuged at 1000 rpm for 5 min, the supernatant discarded and the cell pellet resuspended in the serum-free medium. Cells were cultured in T75 flasks previously coated with collagen, at 37 °C with 5% CO_2 and 90% relative humidity. For collagen coating, rat tail collagen was diluted 1: 100 (v:v) in sterile water; 10 ml of this solution was added to the T75 flask covering the whole surface. Cells were split up to passage 5, detached from T75-flasks by trypsinization and seeded on

Transwells and/or Snapwells inserts which can be both kept in *static conditions*, as expected in classical HBE cell culture, and/or moved into device in dynamic conditions.

Once 70% confluent, NA-HBEC/CF-HBECs were detached from the flask using trypsin–EDTA (Lonza) and approximately 88,463 cells/mm^2 were seeded on the surface of Transwell® inserts (Corning, NY, 0.4 µm pore polycarbonate membrane and 6.5 mm inserts), previously coated with rat-tail collagen. Both the apical and basal sides of the inserts were filled with LHC9-RPMI medium and maintained for 1 day of submerged culture in static condition. Then, in order to guarantee epithelial differentiation, the apical culture medium was removed from the transwell insert and only the basolateral medium was replaced with the PneumaCult™-ALI medium (STEMCELL Technologies) in order to establish an air-liquid interface (ALI) condition. The transwells were left into the multiwell for static culture or moved into the microfluidic device to estabilsh a dynamic cell culture condition. In both conditions, cells generate a highly resistant epithelium, the apical surface will remain "dry" without even a meniscus of liquid around the border.

3.2.4 Live monitoring by TEER measurement

TEER measurements were performed to monitor cellular differentiation and barrier function of the bronchial epithelium. Before starting the measurements, to guarantee an adequate ion concentration in the solution, one hour before the analysis the culture medium was changed and left to stabilize in contact with the cells. TEER measurements were performed by connecting the microfluidic device to an AUTOLAB PGSTAT302N (potentiostat/galvanostat) equipped with a FRA32M module (frequency response analysis module). Impedance spectra were recorded in potentiostatic mode (0.3 V) with an amplitude of 0.01 V and frequencies ranging from 100 kHz to 0.1 Hz between two Au electrodes. For each measurement, three readings and 50 data points (logarithmic frequency step) per reading were collected. Bode Modulus and impedance at 12 Hz were used to monitor the epithelium growth as reported in the literature[158]. Moreover, the least-square optimization method was used to fit the measured impedance data to an electrical equivalent circuit model, reported in Figure 3.5.

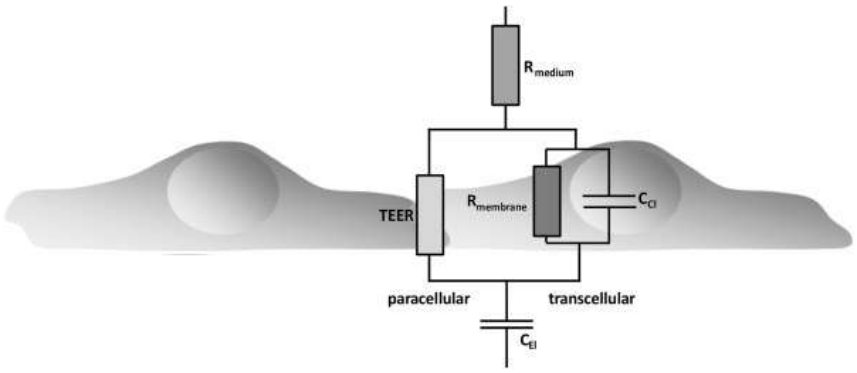

Figure 3.5 - Tissue electrical equivalent circuit model

Within the paracellular pathway, the tight junctional proteins represent an ohmic resistance (TEER) in the circuit diagram, while each lipid bilayer in the transcellular pathway can be described as a parallel circuit of an ohmic resistance ($R_{membrane}$) and an electric capacitance, C_{cl}. Within the considered frequency range, the high resistance of the membrane causes the current to flow predominantly across the capacitor and allows, in first-order approximation, to ignore the membrane resistance. In addition, both the resistance of the surrounding medium (R_{medium}) and the capacitance of the electrodes (C_{El}) need to be considered as well. Thus, for each impedance spectra an apparent R_{TEER} (R_{eq}) was collected and then corrected for the membrane resistance to obtain the effective R_{TEER}.

$$R_{TEER} = \frac{R_{eq}\ x\ R_{membrane}}{R_{eq} - R_{membrane}}$$

R_{TEER} was normalized for the cross-sectional surface area of the chip to calculate the TEER value in Ohm x cm^2.

3.2.5 The forskolin assay

The use of an alternative instrument, such as the potentiostat/galvanostat, to electrically characterize the quality and function of the tissue reproduced in vitro, allows to gather information not only about the transepithelial electrical resistance, but also about the electrical capacitance. As previously discussed, the cell membrane, due to the presence of the phospholipid

double layer and the electric charges that accumulate both on the cytoplasmic and extracellular side of the membrane, is comparable to a capacitor. Therefore, capacity is another parameter that can be useful to describe the differences between the normal or pathologic electrical responses of the epithelium to a chemical stimulus. For this reason, an assay that involves the use of Forskolin can be adopted to further discriminate diseased from healthy tissues, but also to evaluate the efficiency of a drug to rescue CFTR function. Forskolin (coleonol) is a labdane diterpene that is produced by the Indian Coleus plant (Plectranthus barbatus). Forskolin activates the enzyme adenylyl cyclase and increases intracellular levels of cAMP which, in turn, increments endogenous PKA concentrations. CFTR is activated by protein kinase A (PKA) phosphorylation at multiple sites in the regulatory domains (RD). So, extracellular application of micromolar concentrations of forskolin (0.5–10 μM) determines an intracellular increase of cAMP sufficient to activate PKA, with the consequent activation of CFTR. Because CFTR is an integral membrane protein, it will traffic through vesicular membrane compartments such as the endoplasmic reticulum, Golgi stacks, and membranes of the endosomal/lysosomal pathways.[159,160]

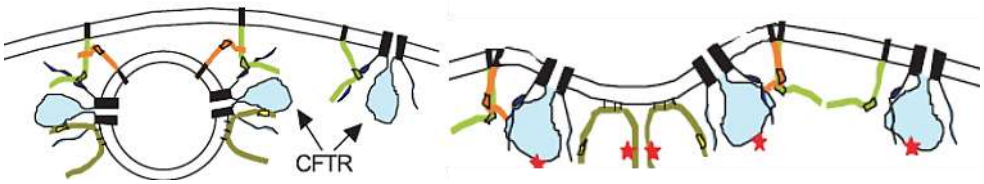

Figure 3.6 - CFTR recruiting after injection of Forskoline

As a consequence, cAMP augmentation, due to Forskolin, guides the encapsulated CFTR trafficking to the plasma membrane. Since the vesicles containing CFTR carry portions of cellular membranes, the fusion between these small cavities and the plasma membrane leads to an increase in surface area which is electrically recorded as an increase in capacitance. This phenomenon can be explained by keeping in mind that the capacity of a body acting as a capacitor depends on the shape and size of its elements, and on the permittivity of the dielectric which separates them, showed in the equation

$$C = \frac{\varepsilon A}{d}$$

which describes the capacitance of a linear capacitor (an equivalent of the plasma membrane). Cells were typically stimulated with 10 µM forskolin and recordings of the electrical capacitance, after forskolin treatment on both NA and CF HBE tissues, were performed at 6 time points: 0, 3, 6, 9, 12 and 15 minutes (time elapsed from the beginning of the measurement with the potentiostat).

3.2.6 Vx809 treatment

The CFTR protein is an ion channel for chlorine, present on the cell membrane of several epithelia; the deletion of phenylalanine in position 508 (ΔF508) causes a defect in the maturation of the CFTR protein, in particular a defective folding or configuration of the amino acid chain that constitutes the protein, with consequent retention in the endoplasmic reticulum and degradation. However, the smallest amount of CFTR that can reach the cell surface has also a defect in the opening of the channel and a considerable instability on the membrane.

From a study on the in vitro experimentation of the molecule published in 2011, VX-809 appears to be a very promising "corrector" [161]. Researchers from the Vertex Pharmaceutical laboratories of San Diego and Cambridge, together with researchers from the Stanford University Cystic Fibrosis Research Laboratory and the Cell Biology and Physiology Laboratory of the University of Pittsburg, conducted research aimed at analyzing the cellular mechanism of action of the VX-809 molecule. In FRT cells (rat thyroid cells) the efficacy of VX-809 in increasing the amount of the mature form of CFTR present on the membrane (known as C band, with higher molecular weight as glycosylated) was evaluated compared to the form immature (band B) present in the cytoplasm.

Using biochemical experiments, in which it is possible to follow the effect of VX-809 on the decrease in the quantity of the immature form and the simultaneous increase in the mature form, the authors found that the prolonged pre-incubation (24-48 hours) of cells with low concentrations of VX-809 (3µM) is able to significantly increase the glycosylated mature form of CFTR. The researchers therefore demonstrated that VX-809 favors the exit of a small amount of CFTR from the endoplasmic reticulum, which can then be transported to the cell membrane. The effect of VX-809 does not appear to be due to the inhibition of the CFTR degradation system, but rather is due to an increased conformation stability of the CFTR protein. This hypothesis is confirmed by proteolysis assay experiments. This technique is based on the premise that folded

proteins are more compact, and therefore more resistant, to proteolytic digestion than unfolded proteins. Experiments have shown that pre-incubation with VX-809 actually allows a fraction of CFTR to take on a more compact and digestive-resistant form, thanks to a correct folding of the CFTR. Using electrophysiological techniques, the authors also verified that preincubation of 24 - 48 hours with VX-809 is able to restore normal activation of the CFTR protein-channel. Many correctors, while being effective in cultures of particular types of human cells often used in laboratory experiments, have however proved ineffective when tested in primary cultures of bronchiolar cells (i.e. in cultures of cells derived directly from the bronchi of sick subjects and precisely from the bronchi smaller) [162]. Therefore, it was considered important to verify the effect of VX-809 also on human cell cultures, isolated from the lungs of patients homozygous for the F508del mutation (HBE FC), and it was found that, even in these cells, the pre-incubation of 24 hours with VX-809 is able to increase both the mature membrane form of the CFTR protein and the secretion of chlorine. The increase in chlorine secretion is equal to 14% of the value found in "healthy" HBE cells. The increased transport of chlorine induced by VX-809, although not very high, is however comparable to the level of chlorine transport found in patients with cystic fibrosis who have less severe mutations (mild) and symptoms.

In order to further validate our samples and implement the microfluidic platform for drug screening, in the second part of the work we tested the effectiveness of VX-809 on our Human Bronchial epithelium (HBE) samples on a chip. Once achieved epithelial differentiation at 6 days of Air Liquid Interface (ALI) culture, we delivered VX-809 (3 μM) to the basolateral medium. Subsequently, we evaluated the action of VX-809 by electrical measurements of cell membrane capacity at 24 hours and 48 hours, in the epithelium stimulated with forskolin, and recorded the hypothetical changes in electrical capacity every 3 minutes for 15 minutes.

3.2.7 Immunofluorescence analysis on whole samples

Both NA-HBEC/CF-HBEC samples, in static and dynamic conditions, were collected in multiwells and washed 3 times with PBS (1X), fixed with PFA (4 %) at 4°C over night. PFA was, then, removed and the membrane was permeabilized using Triton (0.1%) diluted with PBS for 5 minutes at room temperature (RT). At this point, the blocking solution, composed of 3% BSA, 3% FBS and 0.01%

Tryton w/v all diluted in PBS, was added to the samples for 1 hour at room temperature. Samples were incubated overnight with primary antibodies diluted with the blocking solution:

anti-MUC5AC diluted 1:100;

anti-acetylated tubulin diluted 1:100.

After incubation with primary antibodies, samples were washed with PBS and then incubated with a mixture of secondary fluorophores-conjugated antibodies for 1 hour, at room temperature, in the dark. After additional three washings with PBS, phalloidin, diluted 1:200 with PBS (to visualize actin filaments) and DAPI, diluted 1:10000 (to observe the nuclei) were added, respectively for 40 minutes and 20 minutes at room temperature. Samples were washed again and the porous membrane containing the cells were cut from the Transwell support and placed on a specimen slide closed with object-cover and varnish. Images were acquired using a confocal microscope (Confocal Leica TCS SP5 II). Image analysis was performed with the Leica and ImageJ programs.

3.3 Results

3.3.1 Optimization of the microfluidic device - Comsol simulation

In order to create an innovative platform for the culture, differentiation and testing of human bronchial epithelium or the full tickness airway model, we initially focused on the optimization of the cell culture conditions in terms of cell viability and, therefore, the right amount of culture medium and oxygen. The first microfluidic device we fabricated, consisted of two 2 mm Polymethyl methacrylate (PMMA) parts:
the upper part was characterized by a round chamber (12 mm diameter) which housed the filter with the sample above and a downward part in which the channel (1.5 mm deep) was excavated for the basolateral flow of the culture medium (Fig. 3.7).

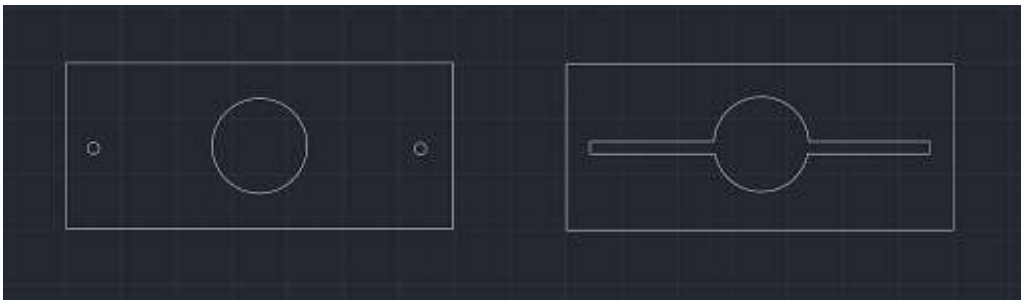

Fig. 3.7– CAD file of the first microfluidic device model:
on the left the top part of the chip with the small lateral holes as inlet and outlet for tube connections used to guarantee the dynamic condition, and the central chamber of diameter 12 mm to house the filter and the sample. On the right the bottom part of the device in which the 1.5 mm deep channel for the basolateral flow of the culture medium.

The two PMMA plates were irreversibly closed (Fig. 3.8) with Isopropyl alcohol (IPA) in a heater at 80 ° C for 15 minutes and used in direct contact with the cells after adequate sterilization with 70% ethanol and UV rays without replication molding or the use of other polymers.

Fig. 3.8 – The first PMMA model of microfluidic chip: the device provides a central pool of 12 mm in diameter and a 1.5 mm deep channel in which the culture medium flows. The central pool allows the placing of the snapwell and so sample housing.

Although the PMMA configuration was higly stable and replicable, this first model of microfluidic chip had several drawbacks:

- Lack of oxygen permeability;
- Poor sealing and adherence of the transwell to the the central chamber walls of the chip with consequent rising or loss of culture medium;
- Long production time (no replica molding);
- Difficulty to obtain optimal sterilization (no autoclave);
- Impossibility of electrode integration into the chip for live monitoring (TEER measurements) of epithelial properties.

For these reasons, we preferred to design and fabricate another type of chip. First of all, we chose to use PMMA only as master to replicate the chips by casting PDMS indefinitely and with shorter manufacturing times than the previous one. Moreover, the PDMS has the advantage of being flexible, manageable and permeable to oxygen, as well as allowing the production of various chips in less time.

Initially, we replicated the same geometry as the first chip (Fig. 3.8) but using PDMS (Fig. 3.9). This configuration features a 15 mm long and 1.5mm wide channel and a 12 mm diameter central pool (complete chip: 40 mm x 16 mm x 1.7 mm). In this microfluidic device, the volume of the culture medium flowing basolaterally to the sample was approximately 170 µl.

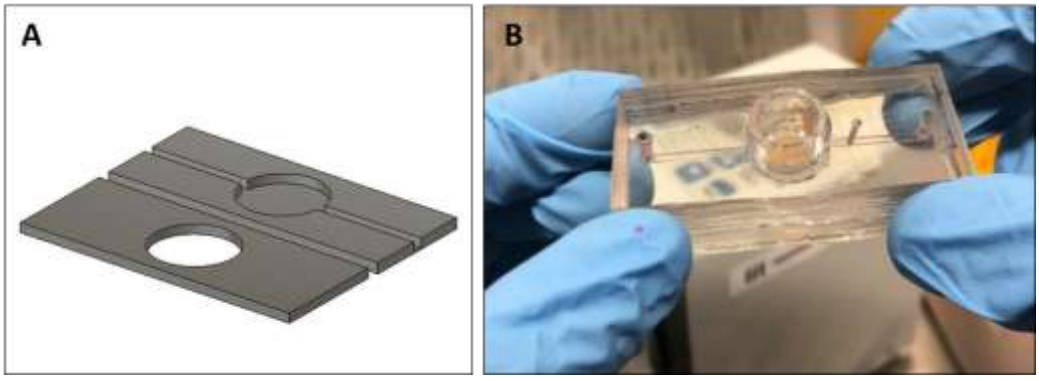

Fig. 3.9 –First PDMS model of microfluidic chip: A) The CAD design in 3D of the upper and lower part of the device; B) The final fabrication in PDMS of this first device model (round widening).

In this condition, despite the continuous change of the culture medium at the basolateral side of the sample due to the dynamic condition, we evaluated that 170 µl was a too low amount of liquid compared to the classic static culture, in which HBE cells need 2 ml of basolateral culture medium

to survive and adequately differentiate. For this reason, we created and tested another configuration, in order to ensure a greater quantity of medium at the basolateral side culture by dampening the walls of the underlying channel (Fig. 3.10). In fact, the second PDMS device allows to ensure a dynamic culture with a volume of approximately 420 µl (maximum basolateral volume that we can ensure with these microfluidic configurations of our interest).

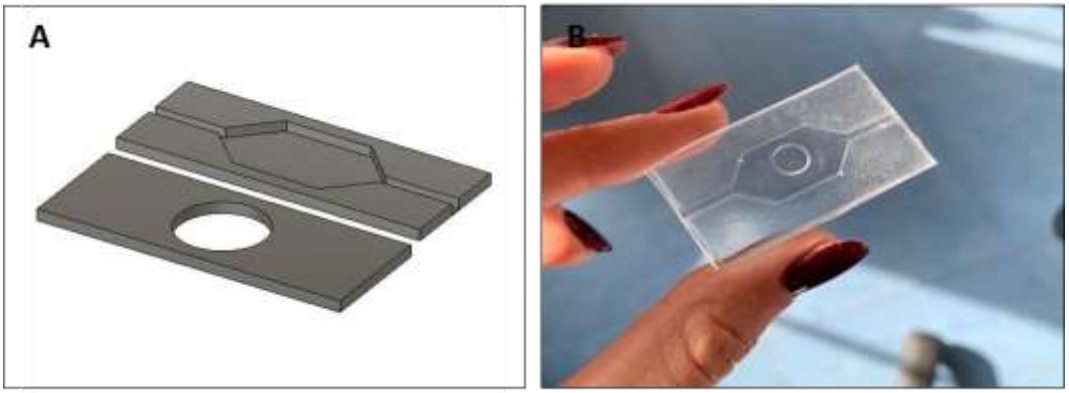

Fig. 3.10 –Second PDMS model of microfluidic chip: A) The CAD design in 3D of upper and lower part of device; B) The final fabrication in PDMS of this first device model (square widening).

In order to select the optimal flow rate for dynamic culture and to check if the bronchial sample was well oxygenated in each configuration, as mentioned in the previous 3.2.2 paragraph, we carried out CFD simulations (Computational Fluid Dynamics). We coupled Navier-Stokes equations with the Brinkman equation in the fluid compartment and in the tissue compartment, respectively. Oxygen consumption by the Human Bronchial Epithelial cells was calculated using a Michelis-Menten equation, taking into account the diffusive/convective oxygen transport. These numerical simulations were performed using different flow rates: 0.04, 2 and 4 mL/min. For both device geometries (round or square widening), at the minimum flow rate (0.04 ml/min), the intermediate flow rate (2ml/min) and the maximum flow rate (4 ml/min) of the persistaltic pump, we verified an excellent oxygen supply to the tissue, as the entire surface of the sample was in contact with the air (Fig. 3.11 A – A ’- A’’, Fig. 3.12 A – A ’- A’’).

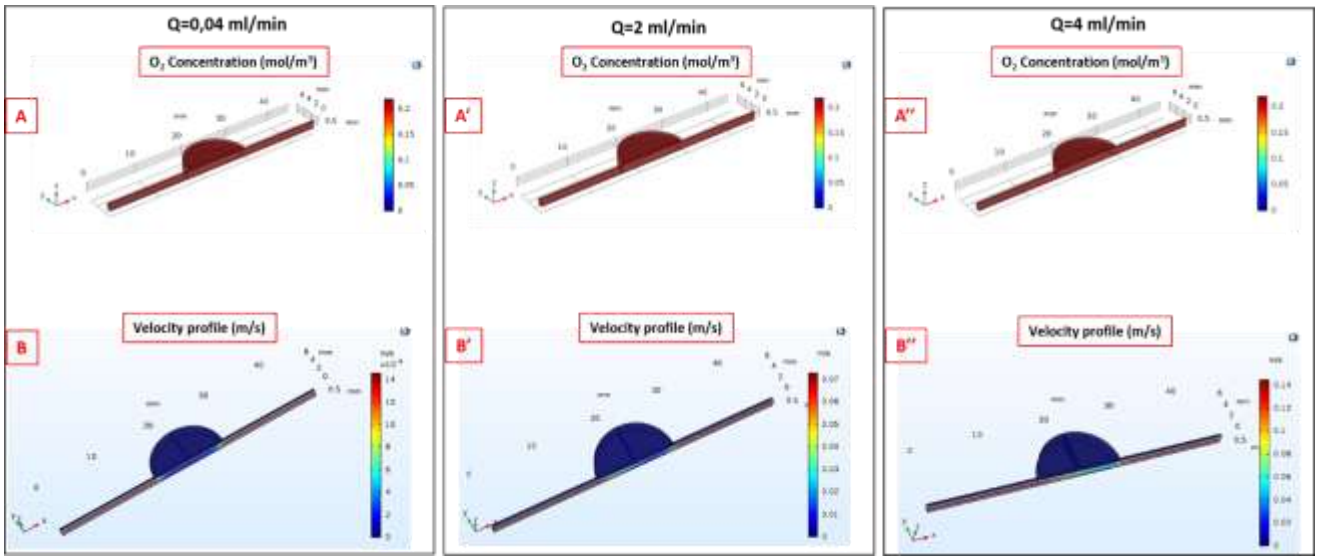

Fig. 3.11 - CFD simulations of bronchial tissue using COMSOL Multiphysics for convective flux and the stream line of the velocity field for 0,04 ml/min, 2ml/min, 4 ml/min in the first PDMS chip model (round widening - round central chamber).

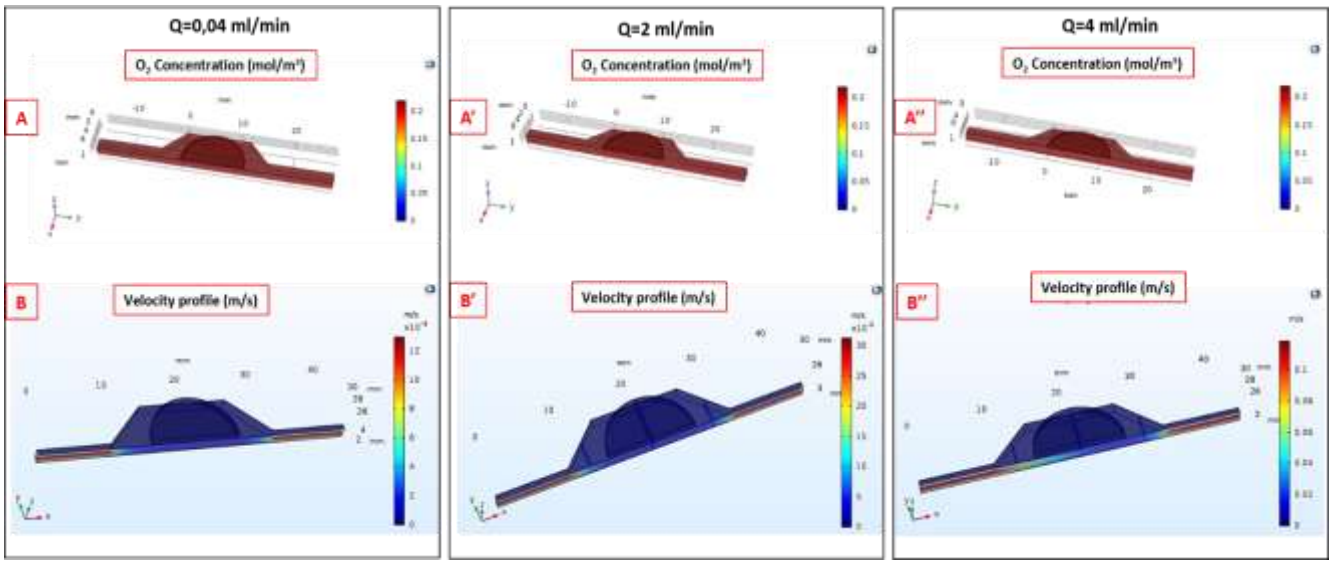

Fig. 3.12 - CFD simulations of bronchial tissue using COMSOL Multiphysics for convective flux and the stream line of the velocity field for 0,04 ml/min, 2ml/min, 4 ml/min in the second PDMS chip configuration (square widening - rectangular central chamber).

Furthermore, at these flow rates and configurations, in both chips it is possible to reach the desired velocity range, as indicated by the literature[163], V= 0.04 – 0.06 m/s; the difference between the two lies solely in the greater amount of volume in the second chip with the square widening conformation (V=420 µl). Therefore, as device for epithelial seeding we chose the second configuration in PDMS (square widening - rectangular central chamber).

However, by carrying out the seeding of the bronchial epithelial cells inside this second PDMS chip, we observed that epithelial damage occurred both at the maximum and minimum flow rates. In fact, after only 5 days of cell culture in this microfluidic chip, the formation of a differentiated epithelium was observed in the chip, but it was not homogeneous. As visible by the fluorescence images, there were areas of excellent differentiation, areas of void due to rupture epithelium and areas of cellular suffering (Fig. 3.13).

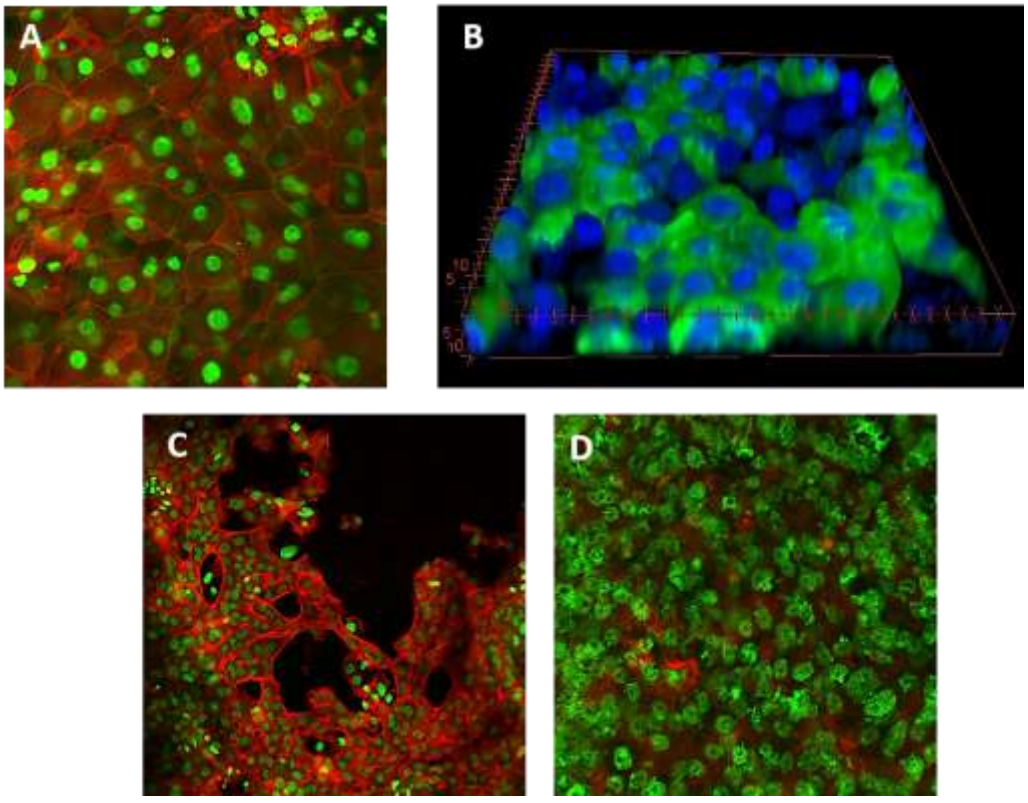

Fig. 3.13 - Morphological characterization of the human bronchial epithelium on chip: Confocal images of the alpha Phalloidin (red) and nuclei (green) showed the formation of a good epithelium A) and the 3D view B) of the confocal image showed nevertheless a ciliary differentiation (Nuclei are marked in blue by DAPI and cilia in green by α-tubulin). Confocal images of the alpha Phalloidin (red) and nuceli (green) showed the formation of areas where the epithelium is damaged C) or with suffering epithelial cells D).

We, therefore, demonstrated that the inhomogeneous epithelial differentiation was due to inadequate shear forces on the surface of the sample and in the vicinity of it. In fact, fluid dynamic simulations at different flow rates showed that shear stresses were not homogeneous over the whole sample, as observed in Fig. 3.14 for the stream line of wall shear stress, thus justifying the results obtained and explained previously (Fig.3.13).

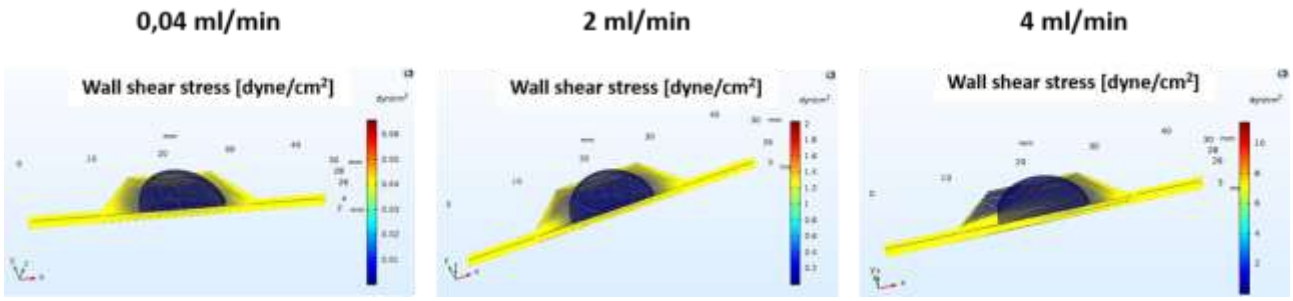

Fig. 3.14 - CFD simulations of bronchial tissue using COMSOL Multiphysics for the stream line of wall shear stress with 0,04 ml/min, 2 ml/min, 4 ml/min in the second PDMS chip configuration (square widening).

Therefore, we designed and manufactured a new chip with the aim to optimize the culture conditions. This chip was similar to the second (square widening), except that the height of the channel was greater (4 mm) in order to reduce the shearing forces and make them homogeneous throughout the sample (Fig. 3.15).

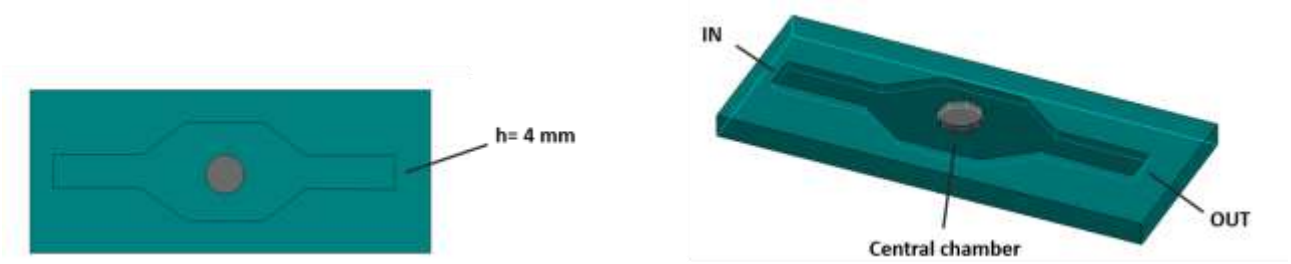

Fig. 3.15 - Third PDMS model of microfluidic chip: The CAD design of the lower part of the device and 3D view of complete chip (square widening with channel height of 4 mm);

By carrying out simulations of the dynamic culture conditions (Fig.3.16), we, not oly evaluated that in correspondence with the three flow rates (minimum flow rate at 0.04 ml / min, intermediate flow rate at 2 ml / min, maximum flow rate at 4 ml / min) the shear stresses were lower than the values observed in the previous device, but, above all, we observed a uniform distribution (contour of shear stress in the figure below rappresented by yellow lines) of the stresses over the entire surface of the sample, a fundamental condition to achieve homogenously differentiated epithelia.

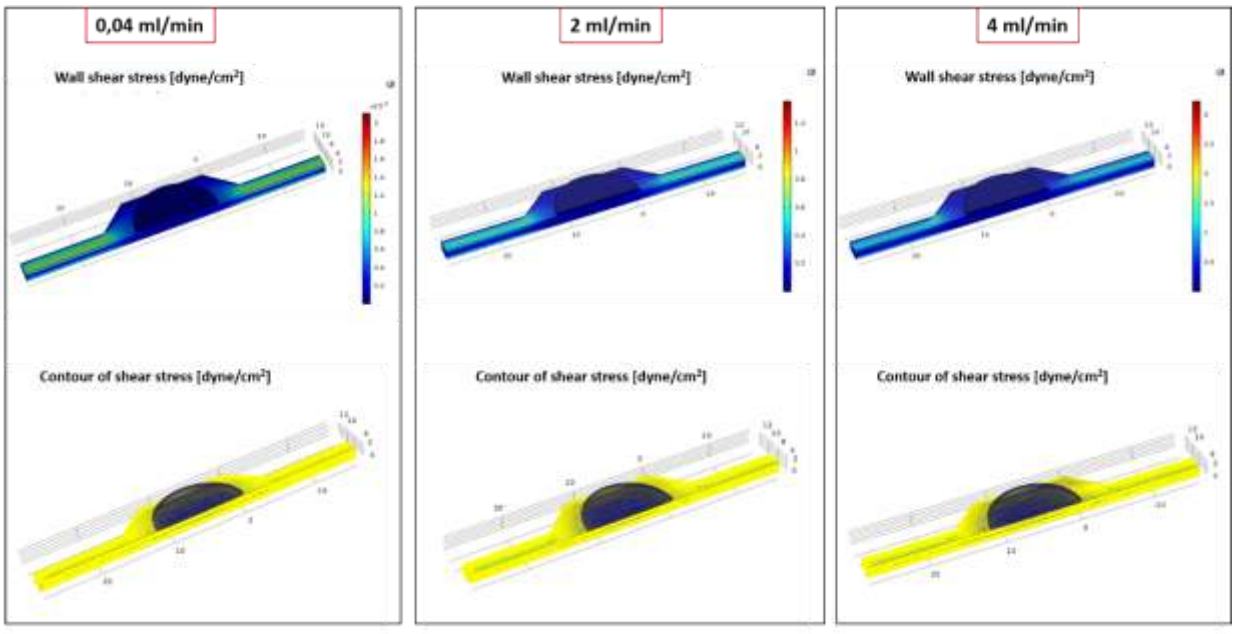

Fig. 3.14 - CFD simulations of bronchial tissue using COMSOL Multiphysics for wall shear stress with 0,04 ml/min, 2ml/min, 4 ml/min in the third PDMS chip configuration (square widening with channel height of 4 mm).

This PDMS configuration "Square widening with 4 mm channel height" proved to be particularly promising for human bronchial epithelium (subsequently for the airway full tickness) to be viable and uniformly well differentiated.

3.3.2 Static vs Dynamic conditions of cell culture

We first tested this device, "Square widening with channel height 4 mm", to compare the dynamic culture with the classic static culture of NA-HBECs or CF-HBECs in order to validate this microfluidic system as an alternative and innovative cell culture platform. So, 88,463 cells/mm^2 were seeded on the surface of each Transwell® insert, as described in the previous paragraph and, after 1 day in static culture condition, placed in dynamic culture for 5 days of air-liquid interface (ALI) condition. As mentioned previously, in parallel the same number of cells was seeded per each Transwell® insert, according to the classical methods of cell culture (static cell culture), and compared the bronchial epithelia of the two cell cultures (dynamic and static cultures) at the same time points, 1 days of submerged culture and 6 days of ALI.

In order to study and monitor the cellular growth / differentiation of the bronchial epithelium over time in a non-destructive way, electrical measurements were carried out on all bronchial tissues, both for static culture and for dynamic culture. In particular, the Transepithelial Electrical Resistance (TEER) and Membrane Capacitance (C_m) measurements were recorded at two intermediate times, in the middle and at the end of cell culture (3 days and 6 days of ALI culture, respectively).

The bronchial epithelium (both normal and CF) grown inside the chip has a TEER and a C_m significantly higher than under static conditions at 3 days (Tab. 5 / Tab. 6). At 6 days, however, the TEER of samples in dynamic culture equals that of samples in static culture, while the C_m of samples in dynamic culture remains always greater than that of the epithelium in static culture (Tab. 5 / Tab 6).

Transepithelial electrical resistance (TEER)		
	3 days of ALI	6 days of ALI
Sample in dynamic culture	1069 ± 732 Ω	517 ± 82 Ω
Sample in static culture	325 ± 175 Ω	421 ± 149 Ω

Tab. 5 – TEER measurements by Potenziostat/Galvanostat electrochemical instrument for samples in dynamic and static cell culture.

Membrane capacitance (C_m)		
	3 days of ALI	6 days of ALI
Sample in dynamic culture	1815 ± 500 nF	2247 ± 690 nF
Sample in static culture	668 ± 356 nF	1705 ± 156 nF

Tab. 6 – C_m measurements by Potenziostat/Galvanostat electrochemical instrument for samples in dynamic and static cell culture.

These higher electrical values were explained and confirmed by Immunofluorescence, on whole samples, for the main markers of bronchial epithelial differentiation (Fig. 3.15). Confocal images of alpha Phalloidin (green) and nuclei (blue) showed the formation of a good bronchial epithelium, more uniform in the samples under dynamic culture than static culture. Moreover, the images of alpha tubulin (cilia) and mucins in red indicated a better epithelial differentiation in the microfluidic device, as demonstrated by the high quantity of mucus on the cell surface and by the homogeneity in cell morphology at day 6. Further quantitative image analyses will be carried out in order to better highlight the difference in epithelial differentiation between the dynamic and the static condition.

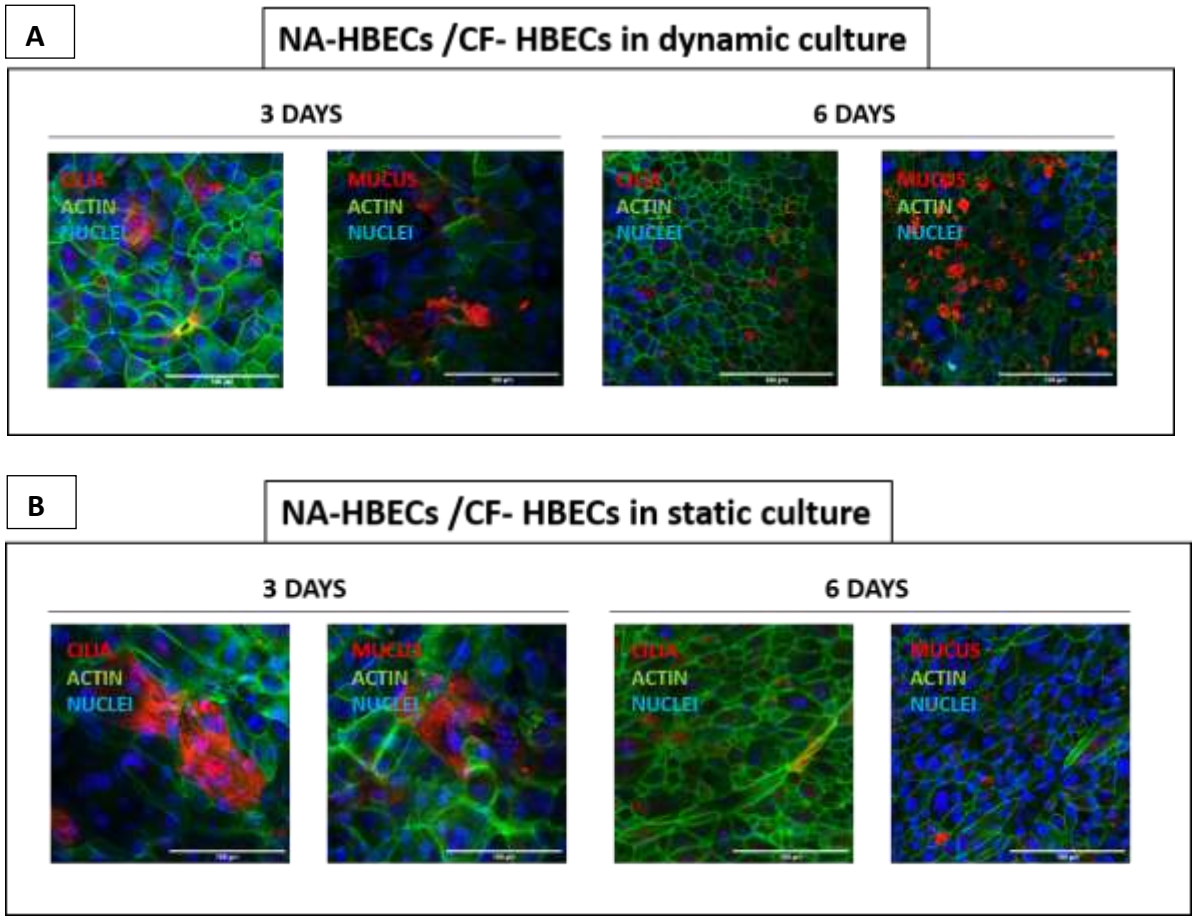

Fig. 3.15 - Morphological characterization of the human bronchial epithelium on chip in dynamic culture A) / in static culture B): Confocal images show alpha Phalloidin (green), alpha tubulin (cilia) in red, mucus (red) and nuclei (blue).

Therefore, this experimental setup demonstrated how the microfluidics chip is a valid cell culture platform for the bronchial epithelium.

3.3.3 Normal and cystic fibrosis bronchial epithelium on chip: functional characterization with Forskolin and VX-809.

The last part of this work was focused on the characterization of the differences between an healthy and a CF epithelium in the chip. In particular, we analyzed the electrical response of the CFTR channel to external stimuli (Forskolin) and to variation in its functionality (exposure to VX-809).

Healthy bronchial epithelia (NA-HBE) and epithelia affected by cystic fibrosis (CF-HBE) were kept in culture and once appropriately differentiated, electrical measurements were carried out by potentiostat analysis to evaluate TEER (index of epithelium integrity) and especially membrane electrical capacity (readout of CFTR activity).

As previously stated (Paraghaph 3.2.5), we expect that in samples with a functional CFTR, the membrane capacity will increase in the presence of forskolin. On the contrary, CF samples will not show such effect.

Cells were stimulated with 10 µM forskolin and recordings of the electrical membrane capacitance C_m, after forskolin treatment, on both NA and CF HBE tissue were performed at 6 time points (Tab. 7): 0, 3, 6, 9, 12 and 15 minutes (time elapsed from the addiction of forskolin and the beginning of the measurements). As expected and reported in Fig. 3.16, the healthy bronchial epithelia (A), showed an increase in Cm, which was almost constant over time, while the CF epithelia (B) displayed a minimal initial decrease in membrane capacity that remained unchanged over time (see Paragr. 3.2.5).

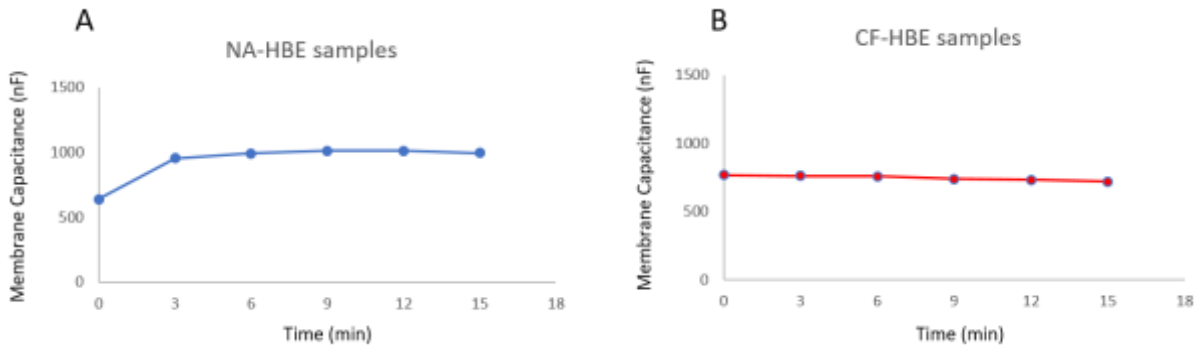

Fig. 3.16 - Electrical measurements at 6 time points (0, 3, 6, 9, 12, 15 minutes) of Membrane Capacity of NA-HBE (A) and CF-HBE (B) samples.

This result was confirmed by confocal microscopy (Fig. 3.17), which showed the apical CFTR localization in NA-HBE (A); and the cytoplasmic CFTR distribution in CF-HBE (B).

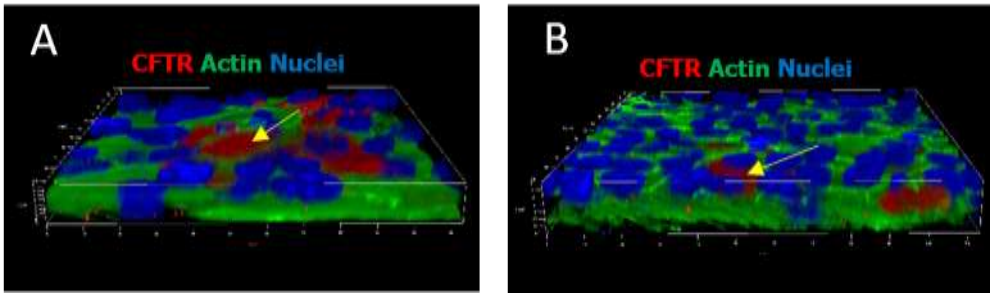

Fig. 3.17 - Morphological characterization of the NA-HBE (A) and CF-HBE (B) on chip by confocal microscopy. Alpha Phalloidin (green), CFTR protein (red) and nuclei (blue) are shown

Once the test was validated, at 6 days of Air Liquid Interface (ALI) culture, we performed the added VX-809 (3 µM) to CF-HBE in the basolateral medium for 48 hours. VX-809 effect was evaluated has been assessed through electrical measurements of cell membrane capacity C_m, stimulating the epithelium with forskolin and recording the changes in electrical capacity every 3 minutes for 15 minutes (Tab.7). As expected, after Vx809 treatment and forskolin stimulation there was a significant increase in C_m as well as a healthy bronchial epithelium, NA-HBE (Fig. 3.18), thus demonstrating the functional internalization of CFTR in the plasma membrane.

Since the single C_m measured at a generic time t, was different from sample to sample, the evaluation of the C_m trend was relative to the delta C_m (ΔC_m), difference between the values recorded at 15 minutes minus the value at 0 min. For healthy samples (NA-HBE) the delta was positive, for samples affected by cystic fibrosis (CF-HBE) the delta was negative or close to zero and therefore for samples affected by cystic fibrosis but treated by VX809 samples the delta was positive as well as NA-HBE (Tab. 7). This has meaning that the treatment with Vx809 gave a positive result, as it was able to restore the correct functioning of the CFTR channel.

Membrane Capacitance C_m			
	NA-HBE samples	CF-HBE samples	CF-HBE samples + Vx809
0 min	639nF	779nF	3890
3 min	952nF	669nF	3730
6 min	990nF	702nF	3650
9 min	1010nF	701nF	3790
12 min	1010nF	732nF	4180
15 min	995nF	720nF	4310
$\Delta C_m = C_f - C_i$	356	-59	420

Tab. 7 - Cell membrane capacity C_m measurements from time 0 (pre-forskolin treatment) to time 15 minutes, measuring every 3 minutes for healthy samples, affected by cystic fibrosis and affected by cystic fibrosis but treated with drug Vx809. The last line shows the total variation of C_m, difference between the values recorded at 15 minutes minus the value at 0 min.

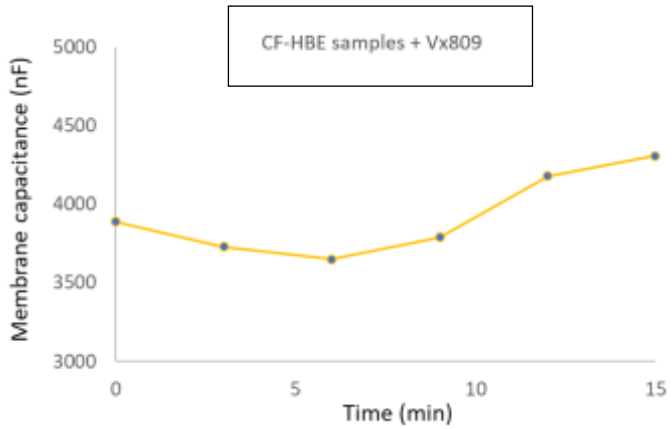

Fig. 3.18 - Electrical measurements at 6 time points (0, 3, 6, 9, 12, 15 minutes) of Membrane Capacity for CF-HBE samples after Vx809 treatment.

3.4 Conclusion

In this work, we developed a fluid-dynamic model able to simulate the physiological condition under which every tissue is fed. There is a urgent need to obtain testing platforms as similar to the in vivo conditions with the aim of overcoming the animal testing; infact the use of human tissue provides a better prediction of human effects/kinetics than in animal tests, simulating the

activities by means of mechanics and physiological response of entire organs and organ systems thanks to a dynamic and continuous flow, obtaining a longer viability cell culture and providing a source for diagnostic tests for personalized medicine. Actually, one of the pressing problems of 3D cultures is the long culture time, in this work we showed that dynamic flow promises to reduce culture time and to improve tissue's features. More experiments are needed in order to optimize the entire process, but the device here showed guarantee the full differentiation and the ability to monitor the tissue growth,differentiation and drug testing in undestructive way through the electrical impedance measuraments.

Moreover, we assume that other possible benefit of dynamic culture in microfluidic device could be a faster and better maturation of the lung stroma by means of a faster degradation of the GPMs and a faster collagen production mediated by the seeded fibroblasts. So, the next experiments will focus on dynamic culture of Human Bronchial full tickness models, healthy and cystic fibrisis tissues, on chip.

We have therefore created and optimized a new platform for cell culture and above all for live monitoring of epithelial functions; this device will soon be further implemented with innovative on-site analyzes to further characterize the epithelium with mucus viscosity studies (MPT on bronchial epithelium / release of particles for measuring mucus thickness).

BIBLIOGRAFIA

1. Chunying, L.; Anjaparavanda P., N. CFTR Chloride Channel in the Apical Compartments: Spatiotemporal Coupling to its Interacting Partners. Integr Biol 2010, 2, 161–177.

2. Ratjen, F.; Bell, S.C.; Rowe, S.M.; Goss, C.H.; Quittner, A.L.; Bush, A. Cystic fibrosis. Nat. Rev. Dis. Prim. 2015, 1, 15010.

3. Cantin, A. M., Hartl, D., Konstan, M. W. & Chmiel, J. F. Inflammation in cystic fibrosis lung disease: Pathogenesis and therapy. *J. Cyst. Fibros.* **14**, 419–430 (2015).

4. Pardo, A. Role of Epithelial Cells in Idiopathic Pulmonary Fibrosis From Innocent Targets to Serial Killers. **3**, 364–372 (2006).

5. Anderson, P. J., Lynch, T. J. & Engelhardt, J. F. Multipotent Myoepithelial Progenitor Cells Are Born Early during Airway Submucosal Gland Development. **56**, 716–726 (2017).

6. Casale, C., Imparato, G., Urciuolo, F. & Netti, P. A. Casale, C., Imparato, G., Urciuolo, F. & Netti, P. A. Endogenous human skin equivalent promotes in vitro morphogenesis of follicle-like structures Bioma- terials 101, 86{95 (2016). *Biomaterials* **101**, 86–95 (2016).

7. Martorina, F., Casale, C., Urciuolo, F., Netti, P. A. & Imparato, G. In vitro activation of the neuro-transduction mechanism in sensitive organotypic human skin model. *Biomaterials* **113**, 217–229 (2017).

8. De Gregorio, V. *et al.* An Engineered Cell-Instructive Stroma for the Fabrication of a Novel Full Thickness Human Cervix Equivalent In Vitro. *Adv. Healthc. Mater.* **6**, (2017).

9. Nyga, A., Cheema, U. & Loizidou, M., 3D tumour models: Novel in vitro approaches to cancer studies J. Cell Commun. Signal. 5, 239{248 (2011);

10. R. Langer, J. P. Vacanti, Tissue engineering, in Science, vol. 260, 1993, pp. 920–926.

11. U. Meyer, The history of tissue engineering and regenerative medicine in perspective, in Fundamentals of Tissue Engineering and Regenerative Medicine, Springer, 2009, pp. 5-12.

12. C. A. Vacanti, The history of tissue engineering, in J. Cell. Mol. Med., vol. 10, n. 3, 2006, pp. 569-576.

13. Nichol, J. W. & Khademhosseini, A. Modular tissue engineering: engineering biological

tissues from the bottom up Soft Matter 5, 1312 (2009);

14. François Berthiaume,1 Timothy J. Maguire,1 and Martin L. Yarmush1,2 - Tissue Engineering and Regenerative Medicine: History, Progress, and Challenges - Annual Review of Chemical and Biomolecular Engineering, Vol. 2:403-430 (July 2011).

15. Review Article: Critical issues in tissue engineering: biomaterials, cell sources, angiogenesis, and drug delivery systems. Naderi H, Matin MM, Bahrami AR. J Biomater Appl. 2011 Sep 16.

16. J. Shi, A. R. Votruba, O. C. Farokhzad, R. Langer, Nanotechnology in Drug Delivery and Tissue Engineering: From Discovery to Applications, in Nano Lett., vol. 10, 2010, pp. 3223-3232.

17. C. Frantz, K. M. Stewart, V. M. Weaver, The extracellular matrix at a glance, in Journal of Cell Science, vol. 123, 2010, pp. 4195-4200. ^ Salta a: a b c d e f g h i j k l m n o p q r s t u.

18. A. Mohamed, M. M. Xing, Nanomaterials and nanotechnology for skin tissue engineering, in Int. J. Burn. Trauma, vol. 2, n. 1, 2012, pp. 29-41.

19. C. P. Barnes, S. A. Sell, E. D. Boland, D. G. Simpson, G. L. Bowlin, Nanofiber technology: Designing the next generation of tissue engineering scaffolds, in Advanced Drug Delivery Reviews, vol. 59, 2007, pp. 1413–1433.

20. B. S. Harrison, A. Atala, Carbon nanotube applications for tissue engineering, in Biomaterials, vol. 28, 2007, pp. 344–353.

21. J. An, C. K. Chua, T. Yu, H. Li, L. P. Tan, Advanced nanobiomaterial strategies for the development of organized tissue engineering constructs, in Nanomedicine, vol. 8, n. 4, 2013, pp. 591-602.

22. CELL-SCAFFOLD INTERACTIONS IN THE BONE TISSUE ENGINEERING TRIADCiara M. Murphy1,* , Fergal J. O'Brien3, David G. Little1, 2 and Aaron Schindeler1.

23. Hillsley MV, Frangos JA. Bone tissue engineering: the role of interstitial fluid flow. Biotechnol Bioeng. 1994 Mar 25;43(7): 573–81.. [PubMed] [Google Scholar].

24. Martin P. Wound healing–aiming for perfect skin regeneration. Science. 1997 Apr 4;276(5309):75–81..

25. Bello YM, Falabella AF, Eaglstein WH. Tissue-engineered skin. Current status in wound healing. Am J Clin Dermatol. 2001;2(5):305–13..

26. Zimmermann WH, Melnychenko I, Wasmeier G, Didié M, Naito H, Nixdorff U, et al. Engineered heart tissue grafts improve systolic and diastolic function in infarcted rat hearts. Nat Med. 2006 Apr;12(4):452–8..

27. Caplan AI, Elyaderani M, Mochizuki Y, Wakitani S, Goldberg VM. Principles of cartilage repair and regeneration. Clin Orthop Relat Res. 1997 Sep;(342):254–69..

28. Palmiero, C., Imparato, G., Urciuolo, F. & Netti, P.Engineered dermal equiv- alent tissue in vitro by assembly of microtissue precursors Acta Biomater. 6, 2548{2553 (2010);

29. Urciuolo, F., Imparato, G., Totaro, A. & Netti, P. A. Building a tissue in vitro from the bottom up: Implications in regenerative medicine Methodist Debakey Cardiovasc. J. 9, 213{217 (2013);

30. Gooch, K. J. et al. - 'Bone Morphogenetic Proteins-2, -12, and -13 Modulate in Vitro Development of Engineered Cartilage Tissue' Eng. 8, 591–601 (2002);

31. Mironov, V., Kasyanov, V., Markwald, R. R. & Prestwich, G. D. Bioreactor- free tissue engineering: directed tissue assembly by centrifugal casting Expert Opin. Biol. Ther. 8, 143{152.

32. Friedrich, J., Ebner, R. & Kunz-Schughart, L. A.Experimental anti-tumor therapy in 3-D: Spheroids { old hat or new challenge? Int. J. Radiat. Biol. 83, 849{871 (2007);

33. Khademhosseini, A. & Bong, G. C. Microscale technologies for tissue engi- neering 2009 IEEE/NIH Life Sci. Syst. Appl.Work. LiSSA 2009 56{57 (2009). doi:10.1109/LISSA.2009.4906708;

34. Wu, M. H., Huang, S. Bin, Cui, Z., Cui, Z. & Lee, G. Bin. A high throughput perfusion-based microbioreactor platform integrated with pneumatic microp- umps for three-dimensional cell culture Biomed. Microdevices 10, 309{319 (2008);

35. Lecuit, T. & Le Go , L. Orchestrating size and shape during morphogenesis Nature 450, 189{192 (2007).

36. Imparato, G., Urciuolo, F., Casale, C. & Netti, P. a. The role of microscaffold properties in controlling the collagen assembly in 3D dermis equivalent using modular tissue engineering. *Biomaterials* **34**, 7851–7861 (2013).

37. Casale, C., Imparato, G., Urciuolo, F. & Netti, P. A. Endogenous human skin equivalent promotes in vitro morphogenesis of follicle-like structures. *Biomaterials* **101**, 86–95 (2016).

38. Ramkumar Tiruvannamalai-Annamalai, David Randall Armant, Howard W. T. Matthew - A Glycosaminoglycan Based, Modular Tissue Scaffold System for Rapid Assembly of Perfusable, High Cell Density, Engineered Tissues - January 20, 2014 - doi:10.1371/journal.pone.

39. Robbins e Cotran - Le basi patologiche delle malattie - Vol. 1 Edition 8th.

40. Adulta, L. E. T. À. Fibrosi cistica, parliamone insieme - Edizione a cura di Fondazione per la ricerca sulla fibrosi cistica, onlus.

41. Mechanisms of endothelial cell dysfunction in cystic fibrosis - L. Totani, R. Plebani, M. Romano et al - ScienceDirect 2017.

42. Establishment and long-term culture of human cystic fibrosis endothelial cells - R. Plebani, R. Tripaldi, M. Romano et al -Nature 2017.

43. Sadava, D., Hillis, D. M., Heller, H. C. & Berenbaum, M. R. Sadava, David Hillis, David M Heller, H Craig Berenbaum, May R - La nuova biologia.blu - Ed. Zanichelli. (1972).

44. Respiratorio, D. A. Apparato respiratorio - Cap. 15 Edised. 345–363.

45. Rosati P., Colombo R.,Maraldi N. - 'Istologia' - Edi. Ermes 2006.

46. Cystic fibrosis - Genetics Home Reference - U.S. National Library of Medicine NIH.

47. Silvia M. Kreda, C. William Davis, and Mary Callaghan Rose - CFTR, Mucins and Mucus Obstruction in Cystic Fibrosis - Cold Spring Harb Perspect Med. 2012 Sep; 2(9): a009589. doi: 10.1101/cshperspect.a009589.

48. Wilfrid Sheldon - 'Congenital Pancreatic Lipase Deficiency' Arch Dis Child. 1964 Jun1.

49. Anderson DH - "Cystic fibrosis of the pancreas and its relation to celiac disease: A clinical and pathological study" - 1938. ,Am J Dis Child 56: 344–399.

50. Mary Callaghan Rose, Judith A Voynow - "Respiratory tract mucin genes and mucin glycoproteins in health and disease". JA 2006. Physiol Rev 86: 245–278.

51. Rose MC, Brown CF, Jacoby JZ III, Lynn WS, Kaufman B - "Biochemical properties of

tracheobronchial mucins from cystic fibrosis and non-cystic fibrosis individuals", 1987. Pediatr Res 22: 545–551.

52. Kesimer M, Kirkham S, Pickles RJ, Henderson AS, Alexis NE, DeMaria G, Knight D, Thornton DJ, Sheehan JK - "Tracheobronchial air–liquid interface cell culture: A model for innate mucosal defense of the upper airways?" , 2008. Am J Physiol Lung Cell Mol Phy.

53. Silvia M. Kreda, C. William Davis, and Mary Callaghan Rose, - "CFTR, Mucins, and Mucus Obstruction in Cystic Fibrosis", Cold Spring Harb Perspect Med. 2012 Sep; 2(9): a009589. doi: 10.1101/cshperspect.a009589.

54. Mary Callaghan Rose, Judith A Voynow - 'Respiratory tract mucin genes and mucin glycoproteins in health and disease', Physiol Rev . 2006 Jan;86(1):245-78. doi: 10.1152/physrev.00010.2005.

55. Hollingsworth MA, Swanson Bj - "Mucins in cancer: Protection and control of the cell surface". 2004 Nat Rev Cancer 4: 45–60.

56. Linden SK, Sutton P, Karlsson NG, Korolik V, McGuckin MA - 'Mucins in the mucosal barrier to infection',2008 Mucosal Immunol 1: 183–197.

57. Cone RA - 'Barrier properties of mucus', 2009 Adv Drug Deliv Rev 61: 75–85.

58. Knowles MR, Boucher RC - 'Mucus clearance as a primary innate defense mechanism for mammalian airways', 2002 J Clin Invest 109: 571–577.

59. Litt M, Khan MA, Chakrin LW, Wardell JR Jr, Christian P - 'The viscoelasticity of fractionated canine tracheal mucus', 1974 Biorheology 11: 111–117.

60. Rose MC, Lynn WS, Kaufman B - 'Resolution of the major components of human lung mucosal gel and their capabilities for reaggregation and gel formation',1979 Biochemistry 18: 4030–4037.

61. Reid CJ, Gould S, Harris A - 'Developmental expression of mucin genes in the human respiratory tract', 1997 Am J Respir Cell Mol Biol 17: 592–598.

62. Chen Y, Zhao YH, Di YP, Wu R 'Characterization of human mucin 5B gene expression in airway epithelium and the genomic clone of the amino-terminal and 5'-flanking region', 2001 Am J Respir Cell Mol Biol 25: 542–553.

63. Caramori G, Casolari P, Di GC, Saetta M, Baraldo S, Boschetto P, Ito K, Fabbri LM, Barnes PJ, Adcock IM, et al - 'MUC5AC expression is increased in bronchial submucosal glands of stable COPD patients', 2009 Histopathology 55: 321–331.

64. Meyerholz DK, Stoltz DA, Namati E, Ramachandran S, Pezzulo AA, Smith AR, Rector MV, Suter MJ, Kao S, McLennan G, et al - "Loss of cystic fibrosis transmembrane conductance regulator function produces abnormalities in tracheal development in neonatal pigs .

65. Kirkham S, Sheehan JK, Knight D, Richardson PS, Thornton DJ - 'Heterogeneity of airways mucus: Variations in the amounts and glycoforms of the major oligomeric mucins MUC5AC and MUC5B', 2002 Biochem J 361: 537–546.

66. Henke MO, John G, Germann M, Lindemann H, Rubin BK - 'MUC5AC and MUC5B mucins increase in cystic fibrosis airway secretions during pulmonary exacerbation', 2005 Am J Respir Crit Care Med 175: 816–821.

67. Jeffrey B. Lyczak et al - "Lung Infections Associated with Cystic Fibrosis", CLINICAL MICROBIOLOGY REVIEWS, Apr. 2002, p. 194–222.

68. Fibrosi in 'Universo del Corpo' - "Fisiopatologia generale", Enciclopedia Treccani.

69. 'Universo del corpo' - Cap.1 Fisiopatologia generale, Enciclopedia Treccani.

70. Alberts et al. Molecular Biology of the Cell. Garland Publishing; 4th Bk&Cdr edition (March, 2002). ISBN 0-8153-3218-1. Undergraduate level.

71. Kulbacka J et al,"Cell Membrane Transport Mechanisms: Ion Channels and Electrical Properties of Cell Membranes.", Adv Anat Embryol Cell Biol. 2017;227:39-58. doi: 10.1007/978-3-319-56895-9_3.

72. Di, A. C. Iannuzzi - "Proprietà bioelettriche delle membrane biologiche", Biofisica e fisiologia I, Medicina e chirurgia. (2009).

73. Freeman, Scott - 'Biological Science, 2nd' (2005) - Pearson Prentice Hall, Upper Saddle River, NJ.

74. 'Epithelial Voltohmmeter', http://www.wpi-europe.com/products/cell-andtissue/teer-measurement/evom2.aspx.

75. 'EndOhm Chamber', http://www.wpi-europe.com/products/cell-andtissue/teer-

measurement/endohm-24snap.aspx.

76. Douville NJ, Tung YC, Li R et al - ‘Fabrication of Two-Layered Channel System with Embedded Electrodes to Measure Resistance Across Epithelial and Endothelial Barriers’, Anal Chem. 2010; 82:2505–2511. [PubMed: 20178370].

77. Benson K, Cramer S, Galla HJ, ‘Impedance-Based Cell Monitoring: Barrier Properties and Beyond’, Fluids Barriers CNS. 2013; 10:5. [PubMed: 23305242].

78. Bhatia, Ingber , "Microfluidic organ on chip” - Nat Biotechnol. 2014 ps - PubMed.

79. Hamelton et al - "Potentially inappropriate medications defined by STOPP criteria and the risk of adverse drug events in older hospitalized patients” - Arch Intern Med 2011, DOI: 10.1001/archinternmed.2011.215.

80. Dongeun Huh , Benjamin D Donald E Ingber et al- ‘Reconstituting Organ-Level Lung Functions on a Chip’, cience . 2010 Jun 25;328(5986):1662-8. doi: 10.1126/science.1188302.

81. Dongeun Huh, Daniel C. Leslie, Donald E. Ingber et al - “A Human Disease Model of Drug Toxicity–Induced Pulmonary Edema in a Lung-on-a-Chip Microdevice" - Science Translational Medicine 07 Nov 2012: Vol. 4, Issue 159, pp. 159ra147 DOI: 10.1126/scitranslme.

82. H. Benam, R. Villenave, D. Ingber et al - ‘Small airway-on-a-chip enables analysis of human lung inflammation and drug responses in vitro’ - 2016 Nat Methods doi: 10.1038/nmeth.3697. Epub 2015 Dec 21.

83. C.L. and A.P. Naren, ‘CFTR Chloride Channel in the Apical Compartments: Spatiotemporal Coupling to its Interacting Partners’, Integr Biol. 2 (2010) 161–177. doi:10.1039/b924455g.

84. Ratjen, F. *et al.* Cystic fibrosis. *Nat. Rev. Dis. Prim.* **1**, 15010 (2015).

85. Nichols, D. P. & Chmiel, J. F. Inflammation and its genesis in cystic fibrosis. *Pediatr. Pulmonol.* **50**, S39–S56 (2015).

86. Su, X. *et al.* Role of CFTR expressed by neutrophils in modulating acute lung inflammation and injury in mice. *Inflamm. Res.* **60**, 619–632 (2011).

87. Mack, M. Inflammation and fibrosis. *Matrix Biol.* **68**–**69**, 106–121 (2018).

88. Hartl, Amit Gaggar, Andreas Hector, Preston E. Bratcher, Marcus A. Mall, Matthias Griese, D. The role of matrix metalloproteases in cystic fibrosis lung disease. *Eur Respir J.* **38**, 721–727 (2011).

89. C.Mazio, L.S.Scognamiglio, G.Imparato, F. Urciuolo, C.Casale, P.A. Netti et al - 'Intrinsic Abnormalities of Cystic Fibrosis Airway Connective Tissue Revealed by an In Vitro 3D Stromal Model' - Cells mdpi 2020 Jun 1;9(6):E1371. doi: 10.3390/cells9061371.

90. P. Scudieri, E. Caci, L.J. V Galietta et al, 'Association of TMEM16A chloride channel overexpression with airway goblet cell metaplasia', J. Physiol. 590 (2012) 6141–6155. doi:10.1113/jphysiol.2012.240838.

91. Nilsson, Ferenc Buzsaky, Klaus Mosbach, K. Growth of anchorage-dependent cells on macroporous microcarriers. *Nat. Publ. Gr.* 6–9 (1986).

92. Urciuolo, F., Imparato, G., Palmiero, C., Trilli, A. & Netti, P. A. Effect of process conditions on the growth of three-dimensional dermal-equivalent tissue obtained by microtissue precursor assembly. *Tissue Eng. Part C. Methods* **17**, 155–164 (2011).

93. C. Mazio, C. Casale, G. Imparato, F. Urciuolo, P.A. Netti, 'Recapitulating spatiotemporal tumor heterogeneity in vitro through engineered breast cancer microtissues', Acta Biomater. (2018). doi:10.1016/j.actbio.2018.04.028.

94. Mattei, G., Gruca, G., Rijnveld, N. & Ahluwalia, A. The nano-epsilon dot method for strain rate viscoelastic characterisation of soft biomaterials by spherical nano-indentation. *J. Mech. Behav. Biomed. Mater.* **50**, 150–159 (2015).

95. Dobin, A. *et al.* STAR: Ultrafast universal RNA-seq aligner. *Bioinformatics* **29**, 15–21 (2013).

96. Anders, S., Pyl, P. T. & Huber, W. HTSeq-A Python framework to work with high-throughput sequencing data. *Bioinformatics* **31**, 166–169 (2015).

97. Frankish, A. *et al.* GENCODE reference annotation for the human and mouse genomes. *Nucleic Acids Res.* **47**, D766–D773 (2019).

98. Robinson, M. D., McCarthy, D. J. & Smyth, G. K. edgeR: A Bioconductor package for differential expression analysis of digital gene expression data. *Bioinformatics* **26**, 139–140 (2009).

99. Huang, D. W., Sherman, B. T. & Lempicki, R. A. Bioinformatics enrichment tools: Paths toward the comprehensive functional analysis of large gene lists. *Nucleic Acids Res.* **37**, 1–13 (2009).

100. Huang, D. W., Sherman, B. T. & Lempicki, R. A. Systematic and integrative analysis of large gene lists using DAVID bioinformatics resources. *Nat. Protoc.* **4**, 44–57 (2009).

101. Qi, M. *et al.* Prevalence and multilocus genotyping of Cryptosporidium andersoni in dairy cattle and He cattle in Xinjiang, China. *Infect. Genet. Evol.* **44**, 313–317 (2016).

102. Kanehisa, M., Goto, S., Sato, Y., Furumichi, M. & Tanabe, M. KEGG for integration and interpretation of large-scale molecular data sets. *Nucleic Acids Res.* **40**, 109–114 (2012).

103. Tanabe, M. & Kanehisa, M. Using the KEGG database resource. *Curr. Protoc. Bioinforma.* 1–54 (2012) doi:10.1002/0471250953.bi0112s38.

104. T. Maier and T. Haraszti, "Python algorithms in particle tracking microrheology," Chem. Cent. J., 2012, doi: 10.1186/1752-153X-6-144.

105. Urciuolo, F., Imparato, G., Totaro, A. & Netti, P. A. Building a tissue in vitro from the bottom up: Implications in regenerative medicine. *Methodist Debakey Cardiovasc. J.* **9**, 213–217 (2013).

106. Wu, S., Peng, Y., Hu, L., Zhang, X. & Li, H. Classification and recognition of texture collagen obtaining by multiphoton microscope with neural network analysis. *J. Phys. Conf. Ser.* **680**, 012014 (2016).

107. Chen, X., Nadiarynkh, O., Plotnikov, S. & Campagnola, P. J. Second harmonic generation microscopy for quantitative analysis of collagen fibrillar structure. *Nat. Protoc.* **7**, 654–669 (2012).

108. Imparato, C. Casale, S. Scamardella, F. Urciuolo, M. Bimonte, F. Apone, G. Colucci, P.A. Netti, G. A novel engineered dermis for in vitro photodamage research. *J. Tissue Eng. Regen. Med.* (2016) doi:10.1002/term.2125.

109. Hristu, R. *et al.* Quantitative second harmonic generation microscopy for the structural characterization of capsular collagen in thyroid neoplasms. *Biomed. Opt. Express* **9**, 3923 (2018).

110. Cicchi, R. *et al.* Scoring of collagen organization in healthy and diseased human dermis by multiphoton microscopy. *J. Biophotonics* **3**, 34–43 (2010).

111. Panwar, P. *et al.* Changes in structural-mechanical properties and degradability of collagen during aging-associated modifications. *J. Biol. Chem.* **290**, 23291–23306 (2015).

112. Lauer, M. E., Dweik, R. A., Garantziotis, S. & Aronica, M. A. The Rise and Fall of Hyaluronan in Respiratory Diseases. *Int. J. Cell Biol.* **2015**, (2015).

113. N. O'Dwyer, Bethany B. Moore, D. The role of periostin in lung fibrosis and airway remodeling. *Cell. Mol. Life Sci.* **74**, 4305–4314 (2017).

114. Norris, R. a *et al.* Periostin Regulates Collagen Fibrillogenesis. **101**, 695–711 (2007).

115. Wells, R. G. Biochimica et Biophysica Acta Tissue mechanics and fi brosis. **1832**, 884–890 (2013).

116. Oshima, A. *et al.* A Novel Mechanism for the Regulation of Osteoblast Differentiation : Transcription of Periostin , a Member of the Fasciclin I Family , is Regulated by the bHLH Transcription Factor , Twist. *J. Cell. Biochem.* **86**, 792–804 (2002).

117. Qin, X. *et al.* TGF β 3-mediated induction of Periostin facilitates head and neck cancer growth and is associated with metastasis. *Nat. Publ. Gr.* **6**, 20587 (2016).

118. Königshoff, M. *et al.* Functional Wnt signaling is increased in idiopathic pulmonary fibrosis. *PLoS One* **3**, 1–12 (2008).

119. Munguía-Reyes, A. *et al.* R-spondin-2 is upregulated in idiopathic pulmonary fibrosis and affects fibroblast behavior. *Am. J. Respir. Cell Mol. Biol.* **59**, 65–76 (2018).

120. Xie, T. *et al.* Transcription factor TBX4 regulates myofibroblast accumulation and lung fibrosis. *J. Clin. Invest.* **126**, 3063–3079 (2016).

121. Hung, C. F., Wilson, C. L., Chow, Y. H. & Schnapp, L. M. Role of integrin alpha8 in murine model of lung fibrosis. *PLoS One* **13**, 1–13 (2018).

122. van der Plaat, D. A. *et al.* Genome-wide association study on the FEV 1 /FVC ratio in never-smokers identifies HHIP and FAM13A. *J. Allergy Clin. Immunol.* **139**, 533–540 (2017).

123. Hector, A. *et al.* The chitinase-like protein YKL-40 modulates cystic fibrosis lung disease.

PLoS One **6**, 1–6 (2011).

124. Genovese M, Borrelli A, Venturini A, Guidone D, Caci E, Viscido G, Gamberdella G, di Bernardo D, Scudieri P, G. L. TRPV4 and purinergic receptor signaling pathways are separately linked in airway epithelia to CFTR and TMEM16A chloride channels. *J Physiol (in Press.*

125. Gianotti, A. *et al.* Pharmacological rescue of mutant CFTR protein improves the viscoelastic properties of CF mucus. *J. Cyst. Fibros.* **15**, 295–301 (2016).

126. Noble, P. W. Epithelial fibroblast triggering and interactions in pulmonary fibrosis. 123–129 (2008) doi:10.1183/09059180.00010904.

127. Parrinello, S., Coppe, J., Krtolica, A. & Campisi, J. Stromal-epithelial interactions in aging and cancer : senescent fibroblasts alter epithelial cell differentiation. *J. Cell Sci.* **118**, 485–496 (2005).

128. Shtilbans, V. Role of Stromal-Epithelial Interaction in the Formation and Development of Cancer Cells. 193–202 (2013) doi:10.1007/s12307-013-0131-5.

129. Brancato, V. *et al.* Bioengineered tumoral microtissues recapitulate desmoplastic reaction of pancreatic cancer. *Acta Biomater.* **49**, 152–166 (2017).

130. De Gregorio, V. *et al.* Intestine-on-chip device increases ECM remodeling inducing faster epithelial cell differentiation. *Biotechnol. Bioeng.* **117**, 556–566 (2020).

131. González-González, L. & Alonso, J. Periostin: A matricellular protein with multiple functions in cancer development and progression. *Front. Oncol.* **8**, 1–15 (2018).

132. Kudo, A. & Kii, I. Periostin function in communication with extracellular matrices. *J. Cell Commun. Signal.* **12**, 301–308 (2018).

133. Ghatak, S. *et al.* Periostin Induces Intracellular Cross-talk between Kinases and Hyaluronan in Atrioventricular Valvulogenesis. **289**, 8545–8561 (2014).

134. Li, Y. *et al.* Severe lung fibrosis requires an invasive fibroblast phenotype regulated by hyaluronan and CD44. *J. Exp. Med.* **208**, 1459–1471 (2011).

135. Rout-pitt, N., Farrow, N., Parsons, D. & Donnelley, M. Epithelial mesenchymal transition (EMT): a universal process in lung diseases with implications for cystic fibrosis

pathophysiology. *Respir. Res.* 1–10 (2018).

136. Salton, F., Volpe, M. C. & Confalonieri, M. Epithelial – Mesenchymal Transition in the Pathogenesis of Idiopathic Pulmonary Fibrosis. *Medicina (B. Aires).* **55**, 1–8 (2019).

137. Ribatti, D. & Santoiemma, M. Epithelial-mesenchymal interactions : a fundamental Developmental Biology mechanism. *Int. J. Dev. Biol.* **58**, 303–306 (2014).

138. Salinas, D. *et al.* Submucosal gland dysfunction as a primary defect in cystic fibrosis. *FASEB J.* **19**, 431–433 (2005).

139. Hays, S. R. & Fahy, J. V. Characterizing mucous cell remodeling in cystic fibrosis: Relationship to neutrophils. *Am. J. Respir. Crit. Care Med.* **174**, 1018–1024 (2006).

140. Inglis, S. K. & Wilson, S. M. Cystic fibrosis and airway submucosal glands. *Pediatr. Pulmonol.* **40**, 279–284 (2005).

141. Huaux, F. *et al.* Dysregulated Proinflammatory and Fibrogenic Phenotype of Fibroblasts in Cystic Fibrosis. *PLoS One* **8**, (2013).

142. Bradley H.Rosen, Marc Chanson and John F.Engelhardt et al - 'Animal and model systems for studying cystic fibrosis', Journal of cystic fibrosis Volume 17, issue 2, 2018.

143. Claudine Guilbault , Zienab Saeed , Gregory P. Downey , and Danuta Radzioch - 'Cystic Fibrosis Mouse Models',2006 American Journal of Respiratory Cell and Molecular Biology.

144. Van Goor F., Straley K. S., Cao D., Gonzalez J., Hadida S., Hazlewood A., et al. . (2006) - 'Rescue of DeltaF508-CFTR trafficking and gating in human cystic fibrosis airway primary cultures by small molecules', Am. J. Physiol. Lung Cell. Mol. Physiol. 290.

145. Awatade N. T., Uliyakina I., Farinha C. M., Clarke L. A., Mendes K., Sole A., et al. . (2015) - 'Measurements of functional responses in human primary lung cells as a basis for personalized therapy for cystic fibrosis' , EBioMedicine 2, 147–153. 10.1016/j.

146. de Courcey F., Zholos A. V., Atherton-Watson H., Williams M. T., Canning P., Danahay H. L., et al. . (2012). 'Development of primary human nasal epithelial cell cultures for the study of cystic fibrosis pathophysiology', Am. J. Physiol. Cell Physiol. 303:

147. Brewington J. J., Filbrandt E. T., LaRosa F. J., III., Moncivaiz J. D., Ostmann A. J., Strecker L. M., et al. . (2018a) - 'Brushed nasal epithelial cells are a surrogate for bronchial epithelial

CFTR studies'. JCI Insight 3:e99385. 10.1172/jci.insight.993.

148. Nikhil T. Awatade, Sharon L. Wong, Shafagh A et al, 'Human Primary Epithelial Cell Models: Promising Tools in the Era of Cystic Fibrosis Personalized Medicine', Front Pharmacol. 2018.

149. Sato T., Vries R. G., Snippert H. J., van de Wetering M., Barker N., Stange D. E., et al. . (2009). 'Single Lgr5 stem cells build crypt–villus structures in vitro without a mesenchymal niche', Nature 459:262. 10.1038/nature07935.

150. Jung P., Sato T., Merlos-Suárez A., Barriga F. M., Iglesias M., Rossell D., et al. . (2011). 'Isolation and in vitro expansion of human colonic stem cells'. Nat. Med. 17:1225. 10.1038/nm.2470.

151. Leushacke M., Barker N. (2014). 'Ex vivo culture of the intestinal epithelium: strategies and applications'. Gut 63, 1345–1354. 10.1136/gutjnl-2014-307204.

152. Ikpa P. T., Bijvelds M. J., de Jonge H. R. (2014) - 'Cystic fibrosis: toward personalized therapies'. Int. J. Biochem. Cell Biol. 52, 192–200. 10.1016/j.biocel.2014.02.008.

153. Melinda Wenner Moyer - 'Organs-on-a-Chip', in Scientific American, vol. 304, n. 3, 2011-03, pp. 19–19, DOI:10.1038/scientificamerican0311-19a.

154. L. Guta and S. Sundar - "Navier-stokes-brinkman system for interaction of viscous waves with a submerged porous structure," Tamkang J. Math., 2010, doi: 10.5556/j.tkjm.41.2010.722.

155. Wikipedia contributors. Shear Stress. *Wikipedia, The Free Encyclopedia.* (2020).

156. Sidhaye, V. K., Schweitzer, K. S., Caterina, M. J., Shimoda, L. & King, L. S. Shear stress regulates aquaporin-5 and airway epithelial barrier function. *Proc. Natl. Acad. Sci. U. S. A.* (2008) doi:10.1073/pnas.0712287105.

157. Benam, K. H. *et al.* Small airway-on-a-chip enables analysis of human lung inflammation and drug responses in vitro. *Nat. Methods* **13**, 151–157 (2016).

158. Kathrin Benson, Sandra Cramer & Hans-Joachim Galla - 'Impedance-based cell monitoring: barrier properties and beyond', 2013 Fluids and Barriers of the CNS.

159. Moran, O. & Zegarra-Moran, O. On the measurement of the functional properties of the CFTR. *J. Cyst. Fibros.* (2008) doi:10.1016/j.jcf.2008.05.003.

160. Bertrand, C. A. & Frizzell, R. A. The role of regulated CFTR trafficking in epithelial secretion. *American Journal of Physiology - Cell Physiology* (2003) doi:10.1152/ajpcell.00554.2002.

161. "Fredrick Van Goor, Sabine Hadida, Paul A Negulescu et al - 'Correction of the F508del-CFTR protein processing defect in vitro by the investigational drug VX-809', 2011 Proc Natl Acad Sci U S A.

162. Nicoletta Pedemonte 1 , Valeria Tomati, Elvira Sondo, Luis J V Galietta - 'Influence of cell background on pharmacological rescue of mutant CFTR', 2010 Am J Physiol Cell Physiol.

163. Vincenza De Gregorio, Brunella Corrado, Simone Sbrescia, Sara Sibilio Francesco Urciuolo, Paolo A. Netti, Giorgia Imparato - 'Intestine-on-chip device increases ECM remodeling inducing faster epithelial cell differentiation' 2019 - Biotechnology and Bioen.